DOCTORAL DISSERTATION

SPH SIMULATIONS ON FAILURE OF A BREAKWATER MOUND DUE TO TSUNAMI SCOUR UNDER EXPERIMENTAL CONDITIONS

実験で観察された津波越流時の防波堤マウンドの洗掘挙動に関する **SPH** シミュレーション

School of Urban Innovation
Yokohama National University

Mohammed Russedul Islam
September 2014

ABSTRACT

Failure of a breakwater during tsunami causes extensive damages to the human lives and properties. Therefore it is very important to investigate the failure mechanisms of a breakwater due to tsunami. Many studies were conducted to investigate the failure mechanisms of a breakwater but a few concentrated extensively on scour of landside mound. The study has attempted to investigate the failure mechanism of a breakwater focusing on the deformation behavior of mound due to scour with experimentally as well as numerically. Moreover, it has proposed some counter measures and has also observed the changes of deformation behavior of the mound due to introduction of the countermeasures.

For experimental investigation, the study has prepared a model of Kamaishi breakwater with a scale of 1/200 of the prototype. Overtopping tsunami water falling into the landside mound with seepage flow due to head difference between landside and seaside of the breakwater was prepared in the experiment to reproduce the natural tsunami attack in caisson type breakwater system. To explore the scour mechanisms the study has conducted experiments with several cases. The cases were designed to observe only seepage flow effect on scour, only overtopping water effect on scour and finally combination of seepage and overtopping effect on scour. The study has found that scour due to overtopping water in the mound increased when seepage flow was combined together. The experimental study has found that existence of hydraulic gradients between seaside and landside of the breakwater was a key parameter to accelerate the scour depth. It has also found that mound showed simultaneous scour and collapse behavior during the process of scouring. Therefore, countermeasures were designed with an ability to reduce the hydraulic gradients and also to control the collapse of mound. It was found that maximum hydraulic gradient was reduced from 0.44 to 0.30 with the introduction of the countermeasures. Collapse of mound was found to be controlled due to physical reinforcement effect. Moreover, it was found that countermeasure had changed the transportation characteristics of the scoured soils. As a result the scour depth and width were found to be significantly reduced when countermeasures were installed in the experiment.

The study has also attempted to simulate numerically the deformation behavior of mound due to scour. For numerical simulation it has developed a smoothed particle hydrodynamic (SPH) code with capability of simulating water and soil together. Water was developed as a Newtonian fluid with viscosity and soil was developed as an elastic perfectly plastic material with Drucker-Prager failure criteria. The study has conducted simulation of couette flow, shear cavity flow, dam break flow to prove the accuracy of the developed SPH code for fluid. Moreover, simple shear test for soil, granular flow test and bearing capacity test for soil were conducted to validate the SPH code for soil. Additionally, flow of water through the porous soil was simulated to verify the coupling ability of the code. It was found that SPH codes for fluid, soil and water-soil coupling were successful in simulating the benchmark cases.

The developed SPH code has used a simplified scour model based on seepage force to take into account the high impact force due to fall of overtopping water as well as the seepage flow from the seaside. The study has simulated the deformation behavior of mound during scour for the same cases as conducted in the experiment. Scour results from the simulations for all the cases with and without countermeasure were found to follow the same trend as that in the experiment.

It was found from both experiment and numerical simulations that deformation behavior due to scour during tsunami overtopping were influenced by the head difference between seaside and landside of the breakwater.

Table of Contents

Chapter 1: Background

CHAPTER 2: Formulations of SPH for Fluid

Chapter 3: Formulations of SPH for Soil

Chapter 4: Permeability and Boiling

Chapter 5: Experimental Investigation for Scour Mechanisms in a Breakwater Mound

Chapter 6: Simulations of Scour by SPH

Chapter 7: Conclusion and Recommendations

List of Notations

c	cohesion
Δd	initial spacing of the particle
h	length of the smoothing function
I_1	first invariant of stress tensor
J_2	second invariant of stress tensor
k	co-efficient of permeability
k_c	Drucker-Prager constant related to cohesion
n	porosity
q_b	bearing capacity
ρ	density
ϕ	frictional angle
α_ϕ	Drucker-Prager constant related to frictional angle
Δt	duration of a time step
μ	dynamic viscosity of a fluid
$\dot{\varepsilon}$	strain rate
p	isotropic pressure
s	deviatoric stress
σ'	effective stress
kPa	kilo Pascal

ACKNOWLEDGEMENTS

I would like to express my sincere gratitude to my supervisor Professor Kimitoshi Hayano for his guidance, patience and overall taking care of the study. His friendly attitude was always a source of great motivation for the study. I would also like to express my gratitude to Professor Kazuo Konagai and Dr. Mamoru Kikumoto for valuable advices. I am also thankful to other members of the research group Nelume Nadeesha, Yan Zhao, Hajime Onoda for kind cooperation. I am also thankful to my wife, my daughter and my parents for encouraging me to work. Finally, I am thankful to almighty God.

CHAPTER 1

BACKGROUND

1.1 Introduction

The great east Japan Earthquake with a moment magnitude of 9.0 occurred on March 11, 2011. It caused extensive damage to human lives, housing and lifeline facilities by seismic motion and tsunami it triggered. From the coastal geotechnical engineering point of view, the damage done to the coastal defense by the tsunami wave imposed a threat on the existing design considerations. It is very important to investigate failure mechanism of a breakwater during tsunami in detail to improve design considerations and thus to protect such an important structure from collapse even during the extraordinary events. The study has considered it to be important to investigate failure mechanism of a breakwater concentrating on scour mechanisms on the landside mound. That is why it has attempted to investigate the deformation behavior of a breakwater mound for tsunami scour. It has decided to perform both experiment and numerical investigation for this purpose.

1.2 Failure mechanisms of coastal defence during tsunami

Coastal defences are built to protect the harbor structures from the sea wave. However, sometimes coastal defence cannot sustain extraordinary events like tsunami. From table 1.1, we can find the possible reasons for the failure of breakwaters. However, to find the exact reason for failure a detailed investigation is necessary. A report by PARI (2011) summarized the failure mechanisms of coastal defence due to tsunami March 2011. Figure 1.1 are summarized version of the failure mechanisms as hypothesized in the report after some minor modifications.

Table 1.1 Summary of the main damage to the break water [collected and partially summarized from Kazama et al. (2012)]

Port Name	Area name	Facility name	Possible causes of damage
Hachinohe	Hattaro	North break water	Wave-dissipating blocks moved, scouring of mounds in the port, sliding of coverings due to tsunami
	Outer harbor	Central breakwater	Collapse due to scouring by tsunami
		No. 2 port break water	Dispersal of covering blocks and split stones caused by the tsunami
Kuji	Mizoguchi	Break water (north-south)	Scouring due to flow rate of the tsunami
Miyako	Desaki	Break water	Sliding and collapse due to tsunami
	Ryujinsaki	Break water	Scouring due to the flow rate of the tsunami
	Fujiwara	Breakwater	Collapse due to the flow rate of the tsunami, sliding and collapse of caissons
Kamaishi	Harbor mouth	Breakwater	Sliding and collapse of caissons due to the wave power of the tsunami and damage to steel cells due to uplift of the opening caused by the flow rate of the tsunami
Oofunato	Harbor mouth	Break water	Sliding and collapse of caissons due to the wave power of the tsunami and damage to steel steel cells due to uplift of the opening caused by the flow rate of the tsunami
Soma	Main port	Break water	Sliding and collapse of caissons due to the wave power of the tsunami during the drawback

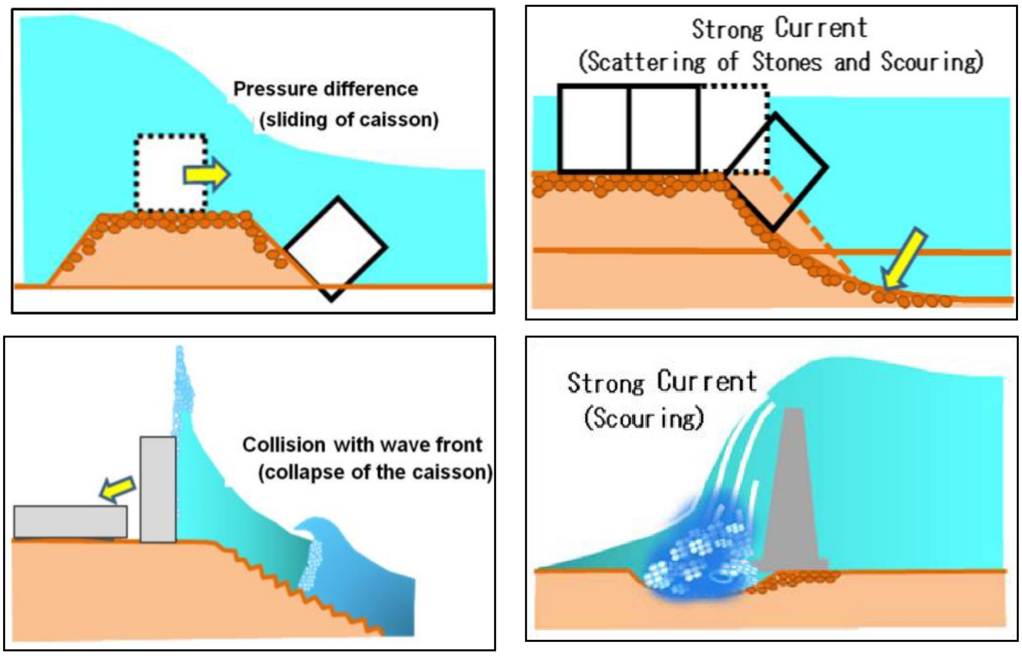

Figure 1.1 Failure mechanisms of coastal defense during tsunami.

Failure of coastal defenses due to pressure difference of seaside and landside and rise of instability of the mound by scouring were considered by many researchers such as T. Arikawa et al. (2012) as shown in figure 1.2.

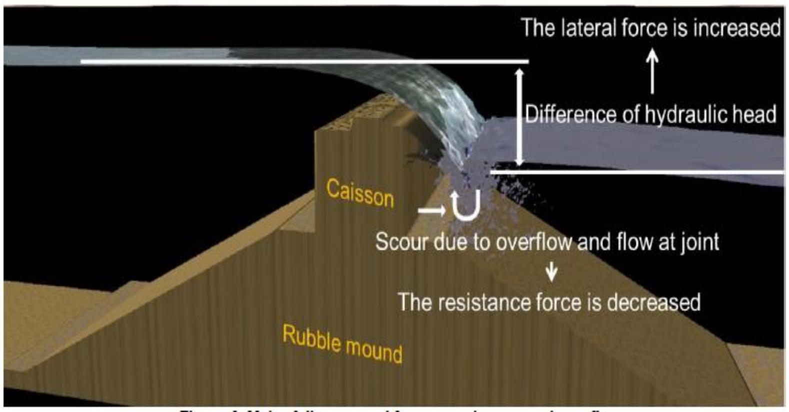

Figure 1.2 Major causes predicted for breakwater failure. [courtesy: Arikawa et al. (2012)]

According to Simeng Dong et al. (2012), at Kamaishi port head difference existed for 8 minutes. Water level difference for such a long time might have caused strong seepage force to be active in the mound. According to Simeng Dong et al. (2012), seepage flow in the rubble mound beneath caisson should be taken into account as a significant influential factor in the design of caisson type composite break water against tsunami. In figure 1.3, it is shown that horizontal hydraulic gradient is higher in harbor side than that in sea side. So, scour due to overtopping water might be more severe with presence of strong seepage force in the mound. However, failure due to combined effect of scour by overtopping and seepage force is yet to be studied in details.

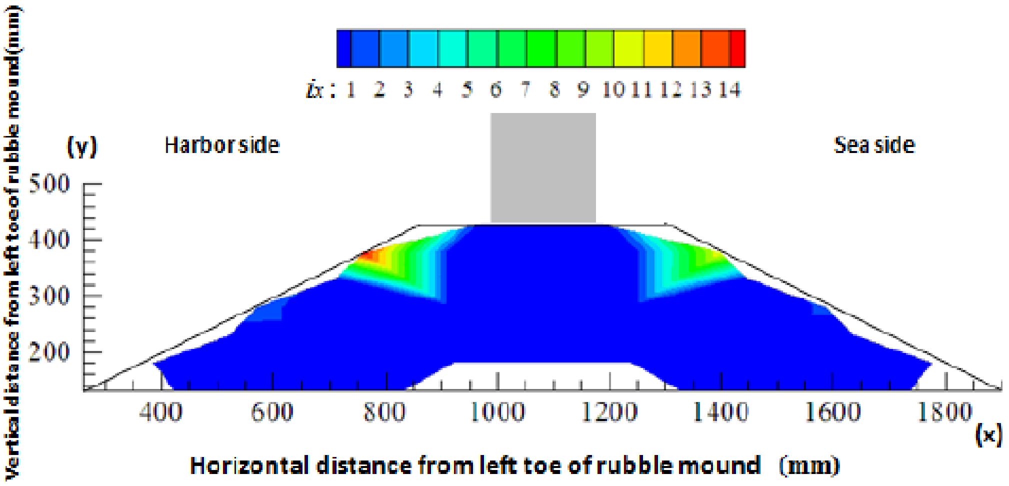

Figure 1.3 Horizontal hydraulic gradient distribution in the mound with 11.8cm head difference. [courtesy: Simeng Dong et al (2012)]

According to Simeng Dong et al. (2012), the bearing capacity of the mound decreases significantly. In figure 1.4, it is found that with same loading pressure settlement of the caisson is higher in the mound when head difference is higher according to Simeng Dong et al. (2012). More recently, a report of PARI, Takahashi et al. (2013) has found that 20% reduction of bearing capacity of the mound can be observed under seepage condition.

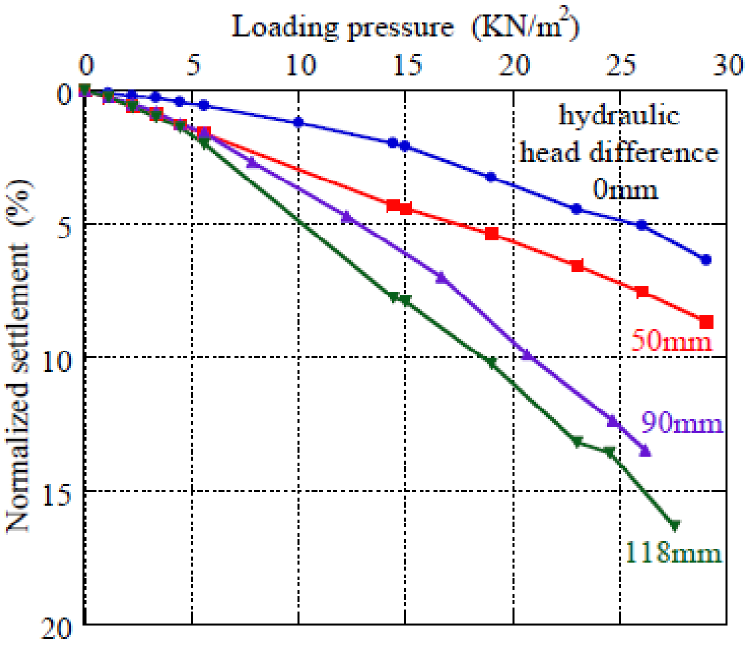

Figure 1.4 Relationship between lading pressure and normalized settlement of caisson. . [Courtesy: Simeng Dong et al. (2012)]

1.3 Failure mechanism considered for the study

From the damage statistics presented in table 1.1 and previous research works discussed in section 1.1, it was found that scour was one of the major causes for breakwater failure. Moreover, from the previous research works it was also found that seepage flow had influence in creating hydraulic gradients in the mound. Seepage flow was also found to reduce the bearing capacity of the mound. During tsunami, scour and seepage flow will remain active at the same time. However, no detailed study was performed about the combined effect of scour and seepage flow. The study has attempted to investigate deformation behavior of the mound for scour by overtopping water with a combined effect of seepage flow as illustrated by figure 1.5. The study has attempted to develop a numerical model to analyze such phenomena under experimental conditions.

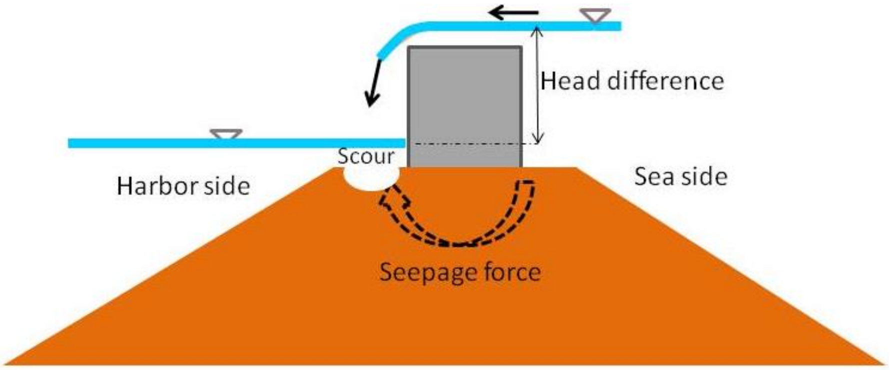

Figure 1.5 A conceptual model to find deformation behavior of the mound under combined effect of scour and seepage.

1.4 Selection of numerical method

1.4.1 Grid based method

The problem specified in above paragraph involves free surface flow, flow through soil pore space and coupling of water and soil. It is very difficult to find a single method based on grid to solve all these problems. Scour by the overtopping water cannot be simulated by the grid based method. It is because grid based method cannot allow large deformation of geo-material as grid would be distorted affecting the accuracy of the calculation.

1.4.2 Particle method

A particle method does not need grids for calculation of field properties. A particle is like a node in the FEM, a calculation unit. To get the properties of the neighboring particles it uses a weighting function usually related to the inverse of the distance. The number of neighboring particles is decided by the influence domain that is redefined in every step. As a result, particle method can simulate free surface flow easily in fluids and allow large deformation in the solids.

1.4.3 Smoothed particle hydrodynamics (SPH)

The particle method usually does not give as accurate result as grid based method like FEM. However, SPH method introduced by Monaghan in 1977 (separately Lucy in 1977) is better than any other particle method in terms of accuracy. It was developed to solve astronomical problems but soon afterwards has become very popular in fluid flow simulations. Wave overtopping characteristics were simulated by Songdong Shao (2006), Jaan Hui Pu (2012) proving the ability of SPH to simulated such violent flow nature. Modelling of stress wave propagation and uniaxial/ triaxial test by Das et al. (2006) and Das et al. (2007) have proved the robustness of SPH in simulating solid mechanics. Fluid-structure interaction was simulated by Carla Antoci (2007) with reasonable accuracy proving the strength of SPH as a coupling tool. Naili et al. (2005) has simulated liquefaction induced lateral spreading by SPH by using Bingham soil model. Seepage flow analysis by Maeda et al. (2004) was a first attempt to simulate geo-material with SPH. After that Sakai H. et al. (2006) has simulated failure of soil considering soil-water-air interaction. Simulation of seepage and erosion with evolution of air bubbles by Sakai H. et al. (2009) was a symbol of SPH advancement in geotechnics. Takbiri et al. (2010) has performed seepage analysis through dam foundation by SPH and compared with FEM. Bui et al. (2011b) has developed a SPH model for seepage flow through deformable porous media where deformation of geo-material was simulated. Large deformation of geo-material with elasto-plastic D-P constitutive model by Bui et al. (2008a) was a milestone of SPH applications in geotechnical engineering. Soil-retaining structure interaction by Bui et al. (2008b) simulated the interaction of flowing geo-materials with the pile structures. Moreover, slope stability analysis and discontinuous slope failure analysis by Bui et al. (2011a), simulation of saturated soil with improved consideration for pore water pressure by Bui et al. (2013) are proofs of SPH ability to handle large deformation of geo-material. Chen et al. (2011) simulated granular flow in 3-D condition by SPH. Yaidel et al. (2012) has improved the accuracy of the granular flow by using different particle size in the simulation termed as dynamic refinement. Hiraoka et al. (2013) has simulated slope failure due to the effect of seismic motion by SPH. Nguyen et al. (2013) has simulated the behavior of modular block retaining wall. Lemiale et al. (2012) has simulated landslide event by combining SPH-DEM method. SPH was used to simulate the onset of the landslide then subsequent flow was simulated by DEM. Numerical application of SPH for deformation, failure and flow problem of geo-material Nonoyama (2011) with more sophisticated soil constitutive model like Cam clay/modified Cam clay has surely proved the growing popularity of SPH in the geotechnical engineering field. Moreover, by using super-sub loading yield surface modified Cam clay model Nonoyama et al. (2013) showed slope failure analysis and also checked the efficiency of the countermeasure to protect the slope failure by SPH. Wang et al. (2013) has developed a new frictional contact to simulate movement of the retaining wall and consequent soil pressure by SPH.

1.5 Objective of the study

The objective of the study was to investigate deformation behavior of a breakwater mound during scour by overtopping tsunami water under experimental conditions.

1.6 Methodology

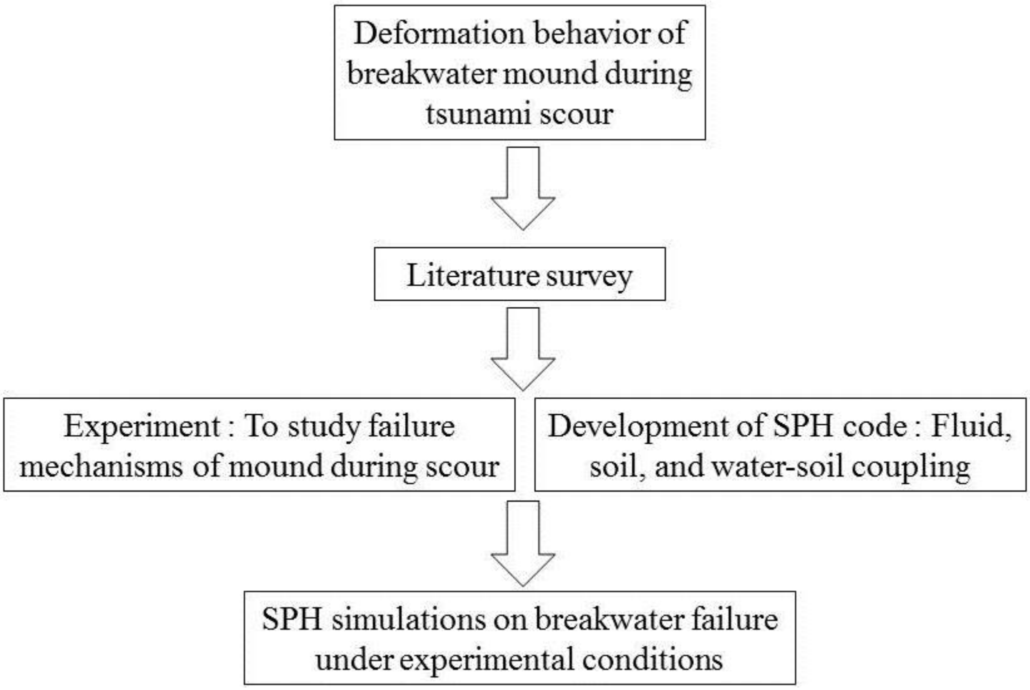

Figure 1.6 Research methodology mapping.

It is to be noted here that the SPH simulations are performed on experimental conditions only. For numerical simulations it is important to compare the results with actual filed data/or experiment data. However, it is very difficult to get field data regarding the failure mechanism considered in the study. That is why experiments were performed and the simulations were done on the experimental conditions and compared thereby.

1.7 Composition of the dissertation

To achieve the objective of the study it was decided to perform numerical as well as experimental investigation. The works done under the study are presented in the dissertation with elaboration. Chapter 2 discusses SPH formulations for fluid. It also presents simulation results for verification of the SPH code for fluid. Chapter 3 discusses about SPH formulations for soil with Drucker-Prager failure criteria. It also presents simulation results to verify the SPH code for soil. Chapter 4 discusses about formulation of two phase model. It also presents the simulation results for permeability test for verification of the two phase model. Additionally, it shows simulation results for seepage flow and boiling phenomenon. Chapter 5 discusses about the experimental investigation of the scour mechanisms. Chapter 6 presents simulation results of scour for the same cases as of the experiment. Chapter 7 presents conclusions and recommendations for future research.

CHAPTER 2

FORMULATIONS OF SPH FOR FLUID

2.1 Introduction

This chapter will describe the general formulations of the SPH method focusing on the fluid. It will discuss important aspects related to numerical implementation of SPH. Additionally, it will present the efficiency of the code developed by the study.

2. 2 Fundamentals of SPH

The fundamentals of SPH discussed here are necessary for understanding and implementing the SPH code. However, more details on conventional SPH can be found on Liu & Liu (2003). The formulations of SPH are divided into two steps. The first step is the integral representation or kernel approximation of the field functions. The second step is the particle approximation.

2.3 Integral representation of a function

The integral representation of a field function $f(\mathrm{x})$ starts from the following.

$$f(x) = \int_{\Omega} f(x')\ \delta(x-x')dx' \qquad (2.1)$$

Where *f(x)* is a function of the three-dimensional position vector x, and $\delta(x-x')$ is the Dirac delta function given by

$$\delta(x-x') = \begin{cases} 1, & x = x' \\ 0, & x \neq x' \end{cases} \qquad (2.2)$$

In equation 2.1, Ω is the area of the integration that contains x and x'; Since the Dirac Delta function is used, the integral representation in equation (2.1) is exact, as long as $f(x)$ is defined and continuous in Ω . Delta function is replaced by a smoothing function $W(x - x\,, h)$, and the integral representations is

$$f(x) = \int_{\Omega} f(x')W(x-x\,,h)dx \qquad (2.3)$$

Where, h is the smoothing length defining the influence domain of the smoothing kernel. $W(x - x\ , h)$ is called kernel or smoothing function.

2.4 Smoothing function

The smoothing function $W(x - x\ , h)$ must satisfy the following three properties. The first one is the normalization condition,

$$\int_{\Omega} W(x-x\,,h)dx\ = 1 \qquad (2.4)$$

The second condition is the delta function property that is observed when smoothing length approaches zero,

$$\lim_{h \to 0} W(x - x\ , h) = \delta(x - x\ ) \qquad (2.5)$$

Additionally, the third condition is the compact condition,

$$W(x - x\ , h) = 0, when\ |x - x\ | > kh \qquad (2.6)$$

Where k is a scalar defines the support domain of the smoothing function.

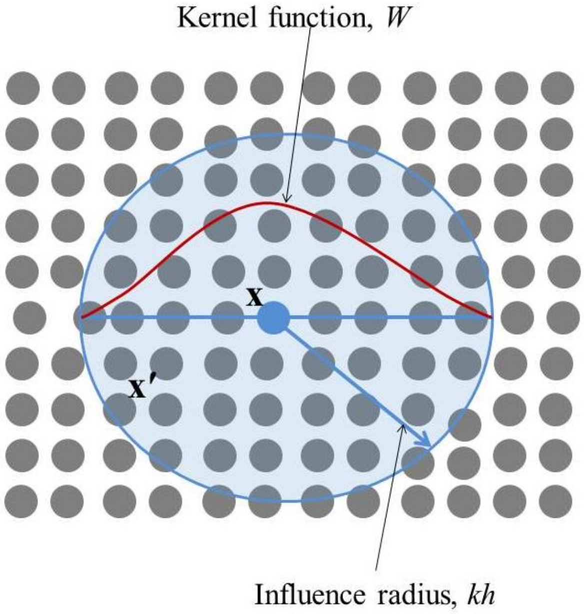

Figure 2.1 Description of influence domain of a field variable 'x'.

There are many kernel functions but the study has used the cubic spline function. The cubic spline function was proposed by Monaghan (1985) as cited by Liu & Liu (2003). It is widely used because it has similarity with Gaussian function. Gaussian function is considered to be a golden selection as it is very stable and accurate. However, it is not theoretically compact, as it never goes to zero. So, it will be computationally more expensive since it will need a long distance for the kernel to become practically close to zero. However, cubic spline function has the advantages of Gaussian function additionally having the compact support. The cubic spline function has the following form:

$$W(q,h) = \alpha_d \begin{cases} 1.5 - q^2 + 0.5q^3 & 0 \le q < 1 \\ \frac{(2-q)^3}{6} & 1 \le q < 2 \\ 0 & q \ge 2 \end{cases} \qquad (2.7)$$

Where,$q = |x - x\ |/h$, $\alpha_d = \frac{1}{h}, \frac{15}{7\pi h^2}, \frac{3}{2\pi h^3}$ respectively in one, two and three dimensions.

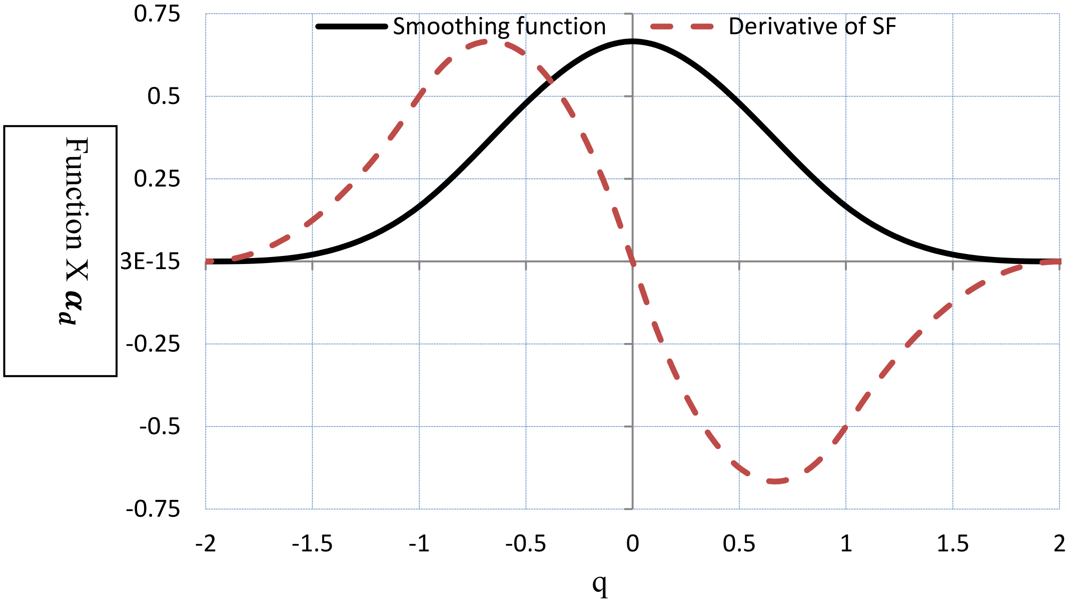

Figure 2.2 The cubic spline kernel and its first derivative.

2.5 Integral representation of the derivative of a function

The approximation for the spatial derivative$\nabla.$ *f(x)* is obtained

$$\langle \nabla . f(x) \rangle \geq \int_{\Omega} [\nabla . f(x')] \; W(x-x',h) dx' \tag{2.8}$$

Right hand side of equation (2.8) can be written

$$[\nabla . f(x')] W(x-x',h) = \; \nabla . [f(x') W(x-x',h)] - f(x') . \; \nabla . W(x-x',h) \tag{2.9}$$

Now by replacing the right side of equation (2.8) with equation (2.9)

$$\langle \nabla . f(x) \rangle \geq \int_{\Omega} \; \nabla . [f(x') W(x-x',h)] dx' - \; \int_{\Omega} f(x') . \; \nabla . W(x-x',h)) \; dx' \tag{2.10}$$

By using the divergence theorem the first integral of the right hand side of equation (2.10) can be converted into an integral over the surface *S* of the domain of integration, Ω.

$$\langle \nabla . f(x) \rangle \geq \int_{\Omega} \; \nabla . [f(x') W(x-x',h)] . \vec{n} \; dS - \; \int_{\Omega} f(x') . \; \nabla W(x-x',h) \; dx' \tag{2.11}$$

Where $\vec{n}$ is unit vector normal to the surface *S*. Since the *W* have compact support , the first part of the right hand side of equation (2.11) will be zero. Finally, we get

$$\langle \nabla . f(x) \rangle \geq \; - \int_{\Omega} f(x') . \; \nabla W(x-x',h) \; \mathrm{d}x' \tag{2.12}$$

However, it is to be noted that if problem domain is truncated by the boundary, compact support condition is not fulfilled.

2.6 Formulation of SPH particle approximation

Infinitesimal volume of the location of particle j is represented dx' in equation (2.3). Let us replace dx' by finite volume V_j. Again we get

$$m_j = \Delta V_j \rho_j \qquad (2.13)$$

Where m_j and ρ_j represent mass and density of particle j (j =1,2,3…..N) , where N is the number of particles within the support domain of the particle i . Let us rewrite equation (2.3)

$$f(x) \cong \sum_{j=1}^{N} f(x_j)\ W(x - x_j, h) \Delta V_j$$

$$f(x) \cong \sum_{j=1}^{N} f(x_j)\ W(x - x_j, h) \frac{1}{\rho_j} (\rho_j \Delta V_j)$$

$$f(x) \cong \sum_{j=1}^{N} f(x_j)\ W(x - x_j, h) \frac{1}{\rho_j} (m_j)$$

$$f(x) = \sum_{j=1}^{N} \frac{m_j}{\rho_j} f(x_j)\ W(x - x_j, h) \qquad (2.14)$$

Equation (2.14) is the particle representation for a function. However, particle representation for the derivative of the function is

$$\langle \nabla . f(x) \rangle = \sum_{j=1}^{N} \frac{m_j}{\rho_j} f(x_j)\ .\ \nabla_i W_{ij} \qquad (2.15)$$

$$W_{ij} = W(x_i - x_j, h) = W(|x_i - x_j|, h) \qquad (2.16)$$

$$\nabla_i W_{ij} = \frac{x_i - x_j}{r_{ij}} \frac{\partial W_{ij}}{\partial r_{ij}} \qquad (2.17)$$

Where r_{ij} is the distance between particle i and j. It is to be mentioned that $\nabla_{ij} W_{ij}$ is taken with respect to particle i, so the negative sign in equation (2.12) is disappeared in equation (2.14)

2.7 SPH formulations for fluid

SPH formulation for fluid is based on Navier-Stokes equations, which states the conservation of mass, momentum and energy. In this study, change of energy was not considered hence formulation of energy equation is not done. If the Greek superscripts α and β are to denote the coordinate directions, repeated indices are used for summation, the Navier-Stokes equations consist of the following. The continuity equation is

$$\frac{D\rho}{Dt} = -\rho \frac{\partial v^{\beta}}{\partial x^{\beta}} \qquad (2.18)$$

2.8 Particle approximation for density evolution

Particle isotropic pressure distribution and smoothing length evolution are based on the density of particle. So density approximation is of great importance in SPH. There two approaches for density evolution. One is summation density approach, another is continuity density approach. The study has used continuity density approach for most of the simulations with free surface flow and also for soil model. For closed flow system like coquette flow, shear cavity flow summation approach was used.

a) Summation density approach

Summation density approach applies the SPH approximation of density itself. If we put ρ_j in place of $f(x_j)$ in the equation (2.13) we get the summation density equation

$$\rho_i = \sum_{j=1}^{N} m_j W_{ij} \qquad (2.19)$$

Where *N* is the number of particles in the support domain of particle *i,* and *j is* the neighboring particles of *i,* m_j is the mass of *j,* W_{ij} is the smoothing function for *i* and *j.* However, the use of equation (2.19) for density calculation induces error near the boundary. Moreover, it cannot simulate free surface flow for fluid accurately. To minimize the errors, normalization with summation smoothing function is performed in the right hand side of equation (2.19) Randles and Libersky (1996), Chen et al. (1999).

$$\rho_i = \frac{\sum_{j=1}^{N} m_j W_{ij}}{\sum_{j=1}^{N} (\frac{m_j}{\rho_j}) W_{ij}} \qquad (2.20)$$

b) Continuity density approach

For simulation of free surface flow density evolution is performed usually by continuity density approach. It is because it can handle property evolution of the particle near the boundary more accurately. This approach is based on the continuity equation. The most popular form of the continuity equation is

$$\frac{D\rho_i}{Dt} = \sum_{j=1}^{N} m_j v_{ij}^{\beta} \frac{\partial W_{ij}}{\partial x_i^{\beta}} \qquad (2.21)$$

Here
$$v_{ij}^{\beta} = (v_i^{\beta} - v_j^{\beta}) \qquad (2.22)$$

Where v_i^{β} and v_j^{β} stand for velocity vector of particle *i* and *j.*

2.9 Particle approximation for momentum equation

From the sets of Navier-Stokes equations, the equation for the conservation of momentum is

$$\frac{Dv^{\alpha}}{Dt} = \frac{1}{\rho} \frac{\partial \sigma^{\alpha\beta}}{\partial x^{\beta}} \qquad (2.23)$$

Applying the particle approximation for derivative of the function equation (2.15) to the right hand side of equation (2.23) result the following

$$\frac{Dv_\beta^\alpha}{Dt} = \frac{1}{\rho_i}\sum_{j=1}^{N} m_j \frac{\sigma_j^{\alpha\beta}}{\rho_j}\frac{\partial W_{ij}}{\partial x_i^\beta} \qquad (2.24)$$

However, momentum equation is used after making modification of the equation (2.24). There are two popular formulations for the momentum equation in SPH. One is

$$\frac{Dv_i^\alpha}{Dt} = \sum_{j=1}^{N} m_j \frac{\sigma_i^{\alpha\beta}+\sigma_j^{\alpha\beta}}{\rho_i\rho_j}\frac{\partial W_{ij}}{\partial x_i^\beta} \qquad (2.25)$$

And the another one is

$$\frac{Dv_i^\alpha}{Dt} = \sum_{j=1}^{N} m_j \left(\frac{\sigma_i^{\alpha\beta}}{\rho_i^2}+\frac{\sigma_j^{\alpha\beta}}{\rho_j^2}\right)\frac{\partial W_{ij}}{\partial x_i^\beta} \qquad (2.26)$$

Both of the above two equations are symmetrized in nature and found to reduce error from particle inconsistency problem. In the above equations $\sigma^{\alpha\beta}$ is the total stress tensor. $\sigma^{\alpha\beta}$ is the combination of isotropic pressure p and the viscous stress τ.

$$\sigma^{\alpha\beta} = -p\delta^{\alpha\beta} + \tau^{\alpha\beta} \qquad (2.27)$$

Where, $\delta^{\alpha\beta}$ is the Kronecher's delta. For isotropic pressure for fluid is obtained explicitly from equation of state in quasi-incompressible or weakly compressible SPH formulation. For Newtonian fluids, the viscous shear stress is proportional to the strain rate ε

$$\tau^{\alpha\beta} = \mu\varepsilon^{\alpha\beta} \qquad (2.28)$$

Where, μ is a constant of proportionality known as the dynamic viscosity of the fluid. Putting the equation (2.27) and (2.28) into the equations (2.25) and (2.26) the momentum equations assume

$$\frac{Dv_i^\alpha}{Dt} = -\sum_{j=1}^{N} m_j \frac{p_i+p_j}{\rho_i\rho_j}\frac{\partial W_{ij}}{\partial x_i^\beta} + \sum_{j=1}^{N} m_j \frac{\mu_i\varepsilon_i^{\alpha\beta}+\mu_j\varepsilon_j^{\alpha\beta}}{\rho_i\rho_j}\frac{\partial W_{ij}}{\partial x_i^\beta} \qquad (2.29)$$

$$\frac{Dv_i^\alpha}{Dt} = -\sum_{j=1}^{N} m_j \left(\frac{p_i}{\rho_i^2}+\frac{p_j}{\rho_j^2}\right)\frac{\partial W_{ij}}{\partial x_i^\beta} + \sum_{j=1}^{N} m_j \left(\frac{\mu_i\varepsilon_i^{\alpha\beta}}{\rho_i^2}+\frac{\mu_j\varepsilon_j^{\alpha\beta}}{\rho_j^2}\right)\frac{\partial W_{ij}}{\partial x_i^\beta} \qquad (2.30)$$

The strain rate $\varepsilon^{\alpha\beta}$ is calculated as the following

$$\varepsilon^{\alpha\beta} = \frac{\partial v^\beta}{\partial x^\alpha} + \frac{\partial v^\beta}{\partial x^\alpha} - \frac{2}{3}(\nabla . v)\delta^{\alpha\beta} \qquad (2.31)$$

And the SPH formulation of equation (2.31) is as the following

$$\varepsilon_i{}^{\alpha\beta} = \sum_{j=1}^{N} \frac{m_j}{\rho_j} v_{ji}^{\beta} \frac{\partial W_{ij}}{\partial x_i^{\alpha}} + \sum_{j=1}^{N} \frac{m_j}{\rho_j} v_{ji}^{\alpha} \frac{\partial W_{ij}}{\partial x_i^{\beta}} - \left(\frac{2}{3} \sum_{j=1}^{N} \frac{m_j}{\rho_j} v_{ji} \,.\, \nabla_{\mathrm{i}} W_{\mathrm{ij}}\right) \delta^{\alpha\beta} \qquad (2.32)$$

2.10 Numerical implementations of fluid flows

2.10.1 Artificial viscosity

The artificial viscosity terms are added with the momentum equation for the fluid flows to dissipate the energy and to prevent particle penetration approaching each other. The formulation for artificial viscosity that was introduced by Monaghan (1989) .

$$\Pi_{ij} = \begin{cases} \dfrac{-\alpha_{\Pi} \bar{c}_{ij} \emptyset_{ij} + \beta_{\Pi} \emptyset_{ij}^2}{\bar{\rho}_{ij}} & v_{ij} . x_{ij} < 0 \\ 0 & v_{ij} . x_{ij} \geq 0 \end{cases} \qquad (2.33)$$

Where

$$\emptyset_{ij} = \frac{h_{ij} v_{ij} . x_{ij}}{\left|x_{ij}\right|^2 + \emptyset^2} \qquad (2.34)$$

$$\bar{c}_{ij} = \frac{1}{2}(c_i + c_j) \qquad (2.35)$$

$$\bar{\rho}_{ij} = \frac{1}{2}(\rho_i + \rho_j) \qquad (2.36)$$

$$h_{ij} = \frac{1}{2}(h_i + h_j) \qquad (2.37)$$

$$v_{ij} = v_i - v_j \,, x_{ij} = x_i - x_j \qquad (2.38)$$

Here , $\phi = 0.1 h_{\mathrm{ij}}$ and α_{Π}, β_{Π} are constants that depend on the type of problem. In the study, since physical viscosity of fluids was considered values for the two constants were taken as 0.06 in the most cases.

2.10.2 Artificial compressibility

According to the artificial compressibility concept theoretically incompressible fluids are considered as weakly compressible. As a result, it is possible to use a quasi-incompressible equation of state to model the incompressible flow. The main purpose of introducing artificial compressibility is to produce the time derivative of pressure. The study has used the following equation of state that was introduced by Monaghan (1994).

$$p = B\left[\left(\frac{\rho}{\rho_0}\right)^{\gamma} - 1\right] \qquad (2.39)$$

Where γ is a constant and set equal to 7 for most cases; ρ_o is the reference density; B is a problem dependent parameter, which sets a limit for the maximum change of the density. B is usually chosen as $B = \frac{\rho_o c^2}{\gamma}$ where c is the sound speed in water. However, if actual c value is used in the simulation time step would become very small. On the other hand, if value of c is too small density variation will be higher. To keep the density variation within 1% c is chosen not less than $10v_{typ}$ instead of the actual value.

When artificial compressibility is introduced in simulation it is useful to consider XSPH technique proposed by Monaghan (1989). According to XSPH technique, the particle moves in the following way.

$$\frac{dx_i}{dt} = v_i - \varepsilon \sum_j \frac{m_j}{\rho_j} v_{ij} W_{ij} \qquad (2.40)$$

Where ε is a constant with a range of 0 to 1.0. The use of XSPH reduces the pressure fluctuation in the simulation that is a typical problem with the weakly compressible SPH.

2.11 Boundary treatment

Boundary treatment is very important to minimize error from particle deficiency near the boundary. The study has used non-slip boundary, symmetric boundary, repulsive boundary and periodic boundary treatments and achieved stable results. In the following sections, first three types boundary are described. Periodic boundary is discussed in coquette flow section.

2.11.1 Non-slip boundary treatment

Non-slip boundary is designed according to the Morris et al. (1997) and Bui et al. (2008a) where boundary particles contribute to real particles in velocity and stress gradient. By using this type of boundary particle deficiency problem near the boundary can be minimized. This fixed type boundary are arranged as in the figure 2.3. v_A and d_A are the velocity and distance from the wall of the real particle. v_B and d_B are the velocity and distance from the wall of the boundary particle. Velocity of a boundary particle is assumed as $v_B = -(d_B/d_A)\, v_A$, so that zero velocity is attained in the plane. The relative velocity between a real and boundary particle is solved

$$v_{AB} = v_A - v_B = \beta(v_A) \qquad (2.41)$$

$$\beta = \min(\beta_{max}, 1.0 + \frac{d_B}{d_A}) \qquad (2.42)$$

Here, β_{max} is used to avoid extremely large value of velocity for a boundary particle when d_A is very small. Typical value for β_{max} is 1.5- 2.0.

The boundary particles in this type also have stress components as implemented by Bui et al. (2008a) If a boundary particle j, are within the support domain of a real particle i then stress will be assigned according to

$$\sigma_j^{\alpha\beta} = \sigma_i^{\alpha\beta} \qquad (2.43)$$

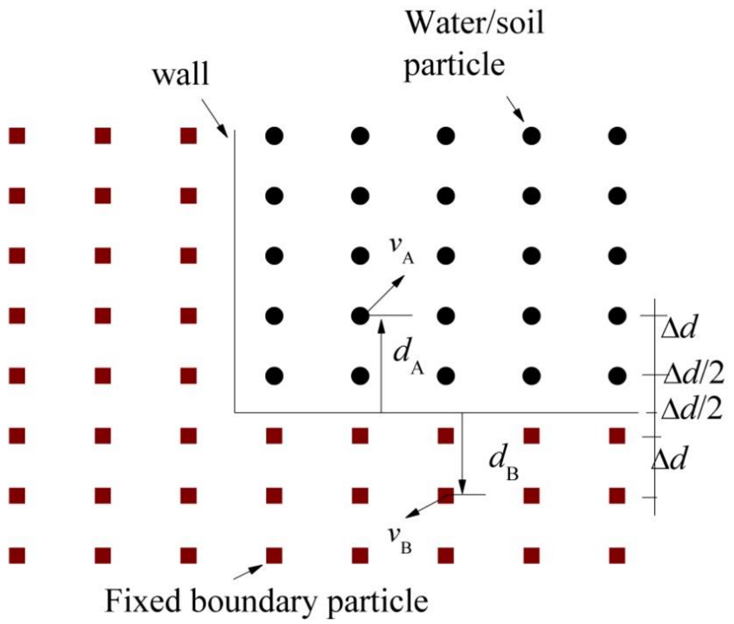

Figure 2.3 Definition of boundary particles in case of non-slip boundary.

2.11.2 Symmetric boundary

The symmetric boundary condition in the study is modelled by ghost particles as Randles and Libersky (1996). Ghost particles are the boundary particles that are generated in every step according to the arrangement of the real particles near the boundary. Sometimes these are referred as the mirror particles in the literature as they assumed mirrored vector properties of the real particles as shown in figure 2.4. However, in the study the ghost particles have the stress components as in the following :

$$\boldsymbol{\sigma}_{\boldsymbol{ghost}}^{\boldsymbol{\alpha\beta}} = \begin{cases} -\boldsymbol{\sigma}_{\boldsymbol{real}}^{\boldsymbol{\alpha\beta}}, & \boldsymbol{\alpha \neq \beta} \\ \boldsymbol{\sigma}_{\boldsymbol{real}}^{\boldsymbol{\alpha\beta}}, & \alpha = \beta \end{cases} \tag{2.44}$$

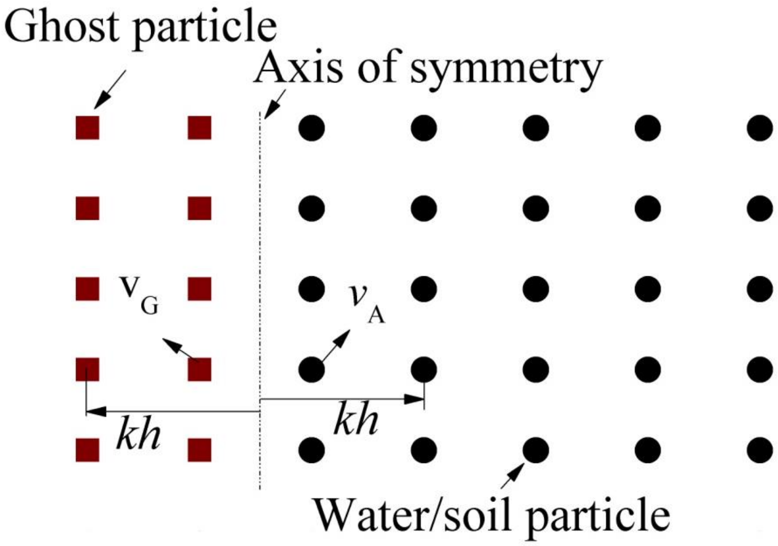

Figure 2.4 Definition of boundary particles in case of symmetric boundary.

2.11.3 Repulsive boundary

Repulsive boundary in the study is implemented according to Monaghan (1994) where boundary particles are placed as in figure 2.5. The boundary particles exert a repulsive force pairwise along the centerline of the pair.

$$FB_{ij} = \begin{cases} D\left[(\frac{r_o}{r_{ij}})^{n_1} - (\frac{r_o}{r_{ij}})^{n_2}\right], & (\frac{r_o}{r_{ij}}) \leq 1 \\ 0, & (\frac{r_o}{r_{ij}}) > 1 \end{cases} \qquad (2.45)$$

Where parameters n_1 and n_2 are should be chosen so that $n_1 > n_2$. According to Monaghan (1994) results are almost same if n_1 and n_2 are 4 and 2 or 12 and 6 respectively. The study also got the similar impression while implementing the repulsive boundary condition. D is a problem dependent parameter in the same scale as the square of the largest velocity, r_o is the cutoff distance where the force will be active usually equal to the initial particle spacing, r_{ij} is the distance between the real i and boundary particle j.

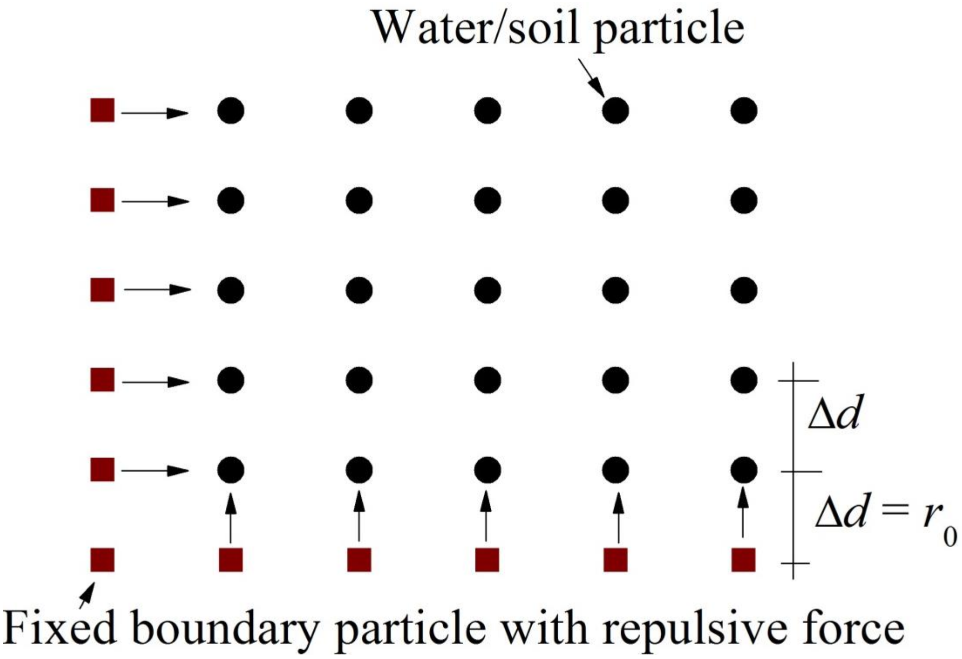

Figure 2.5 Definition of boundary particles in case of repulsive boundary.

2.12 Time integration

The study has used Leapfrog (LF) algorithm for integration of the SPH differential equations. LF algorithm is done:

$$\rho_{n+1/2} = \rho_{n-\frac{1}{2}} + \Delta t(\frac{D_\rho}{D_t})_n \qquad (2.46)$$

$$v_{n+1/2} = v_{n-\frac{1}{2}} + \Delta t(\frac{D_v}{D_t})_n \quad (2.47)$$

$$\sigma_{n+1/2} = \sigma_{n-\frac{1}{2}} + \Delta t(\frac{D_\sigma}{D_t})_n \quad (2.48)$$

$$x_{n+1/2} = x_n + \Delta t v_{n+1/2} \quad (2.49)$$

Here $\triangle t$ is the time step, *n* is the number of current time step. For selection of $\triangle t$ Courant –Frieddriches-Levy (CFL) condition should be checked.

$$\Delta t \leq 0.25\min(\frac{h_i}{c}) \quad (2.50)$$

$$\Delta t \leq 0.25\min\sqrt{(\frac{h_i}{f_i})} \quad (2.51)$$

$$\Delta t \leq 0.125\min(\frac{{h_i}^2}{v}) \quad (2.52)$$

Where *c* is the sound speed, f_i is the acceleration, *v* is the viscosity, h_i is the smoothing length.

2.13 Verification of the code for fluid

The developed SPH code for fluids has been validated by solving some benchmark cases.

2.13.1 Couette flow

For verification of the numerical code coquette flow simulation is popular as it has analytical solution Morris et al. (1997). The coquette flow is a fluid flow between two infinite plates initially stationary as shown in figure 2.6. The flow is generated when the upper plate moves with velocity of 2.5×10^{-5} m/s .

The study has used total 800 particles to represent the coquette flow problem. Table 2.1 summarizes the parameters used for the simulation.

Table 2.1 Summary of parameters used for couette flow simulation.

Number of particles, *N*	800
Initial particle spacing(m), *Δd*	0.00025
Dynamic viscosity of fluid (N.s/m^2) , μ	10^{-3}
Average velocity coefficient, ε	0.3
Boundary type for plate	Repulsive
Boundary type for infinity flow	Periodic
Duration of each time step (s), *Δt*	$1\text{x}10^{-4}$

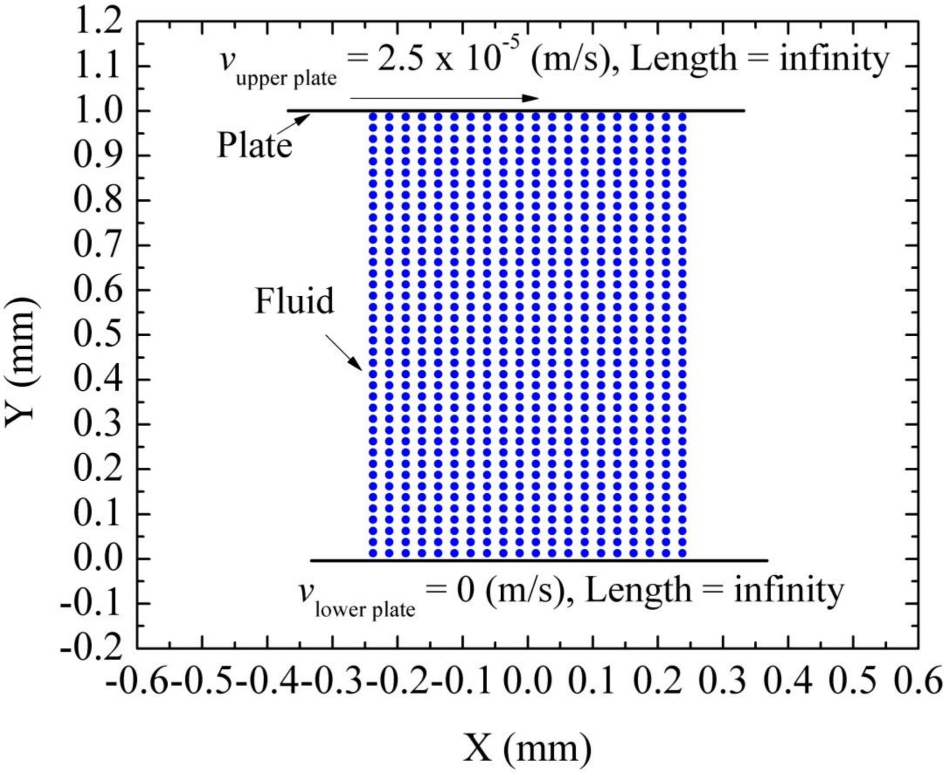

Figure 2.6 Initial conditions for coquette flow.

2.13.1.1 Periodic boundary

To simulate flow of infinite length, the study has adopted the periodic boundary condition. In this boundary system, a particle leaving a predefined boundary outlet immediately reenters into the system through the opposite inlet. Moreover, a particle located within the support domain from the boundary face interacts with the particle within support domain from the opposite face of boundary. In figure 2.7 and 2.8, some particles have reentered into the system after leaving outlet boundary line.

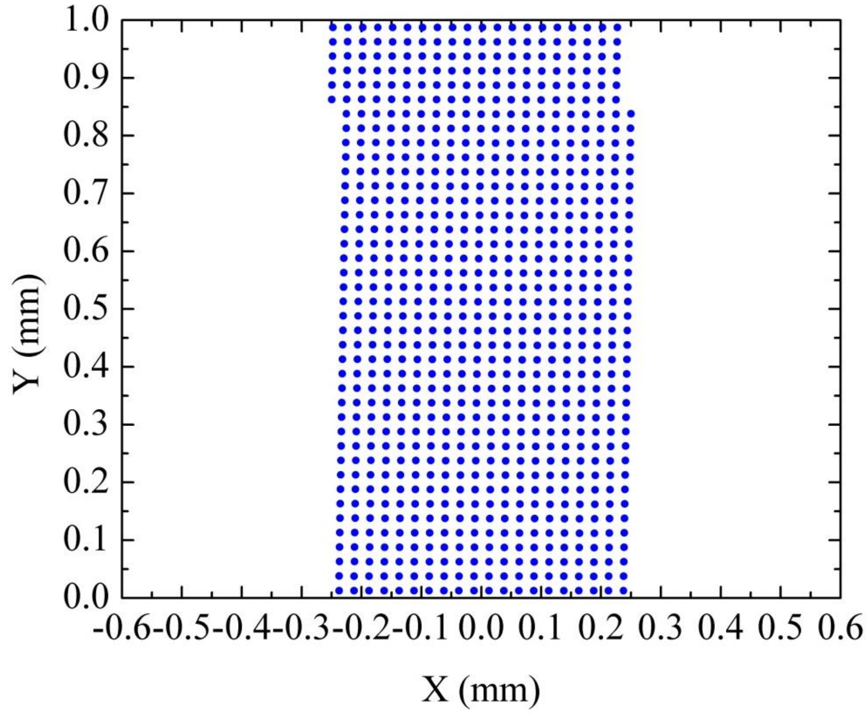

Figure 2.7 Particle distributions at 0.60seconds for couette flow.

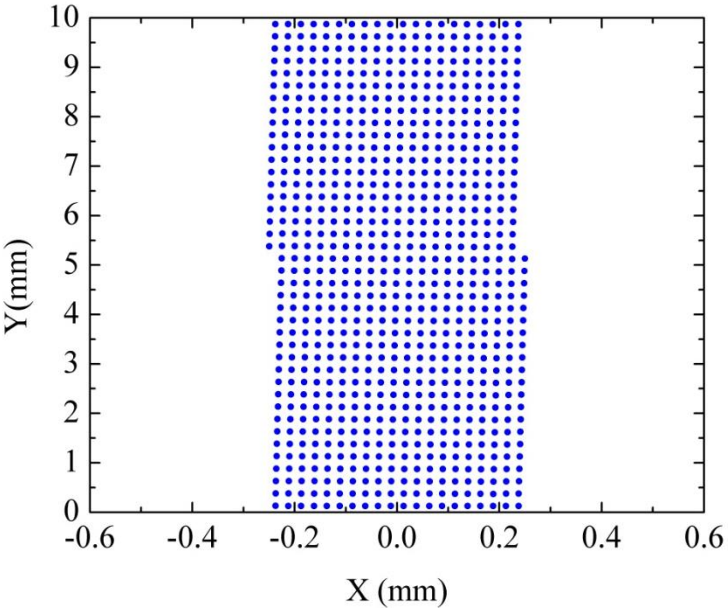

Figure 2.8 Particle distributions at 1.0 second for couette flow.

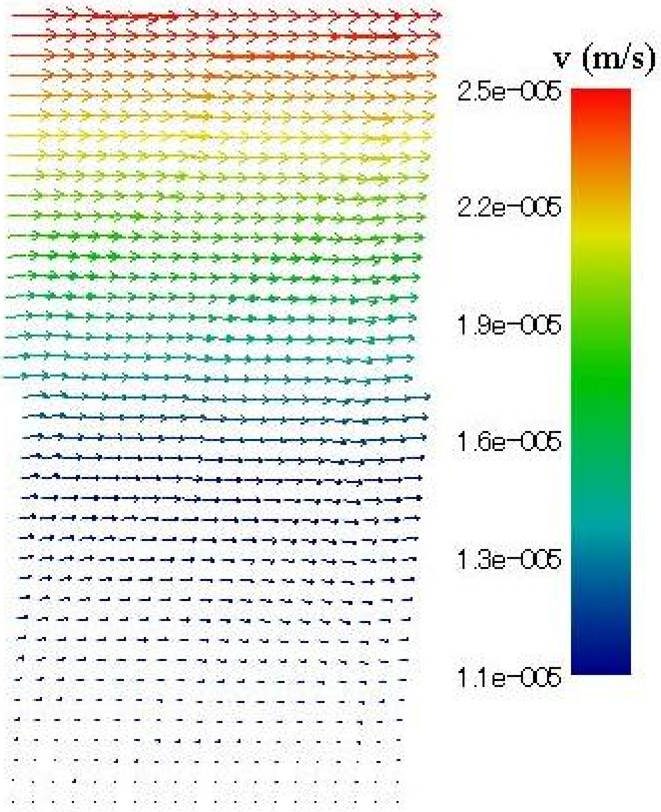

Figure 2.9 Velocity vector for coquette flow at 1.0 second.

2.13.1.2 Accuracy of couette flow simulation

Figure 2.9 shows the velocity distribution of the fluid particles. Figure 2.10 shows the analytical and SPH solution performed by Liu (2003). Figure 2.11 shows the analytical and SPH simulation of coquette flow by the study. It is clear that simulation by the study match nicely with the analytical solution.

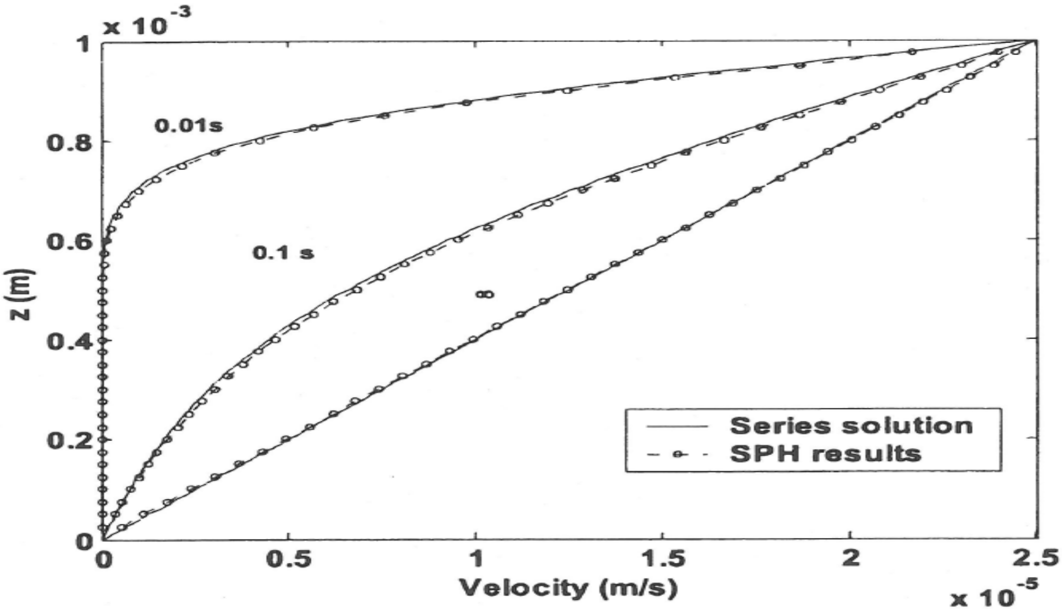

Figure 2.10 Velocity profiles for coquette flow. [Courtesy: Liu (2003)]

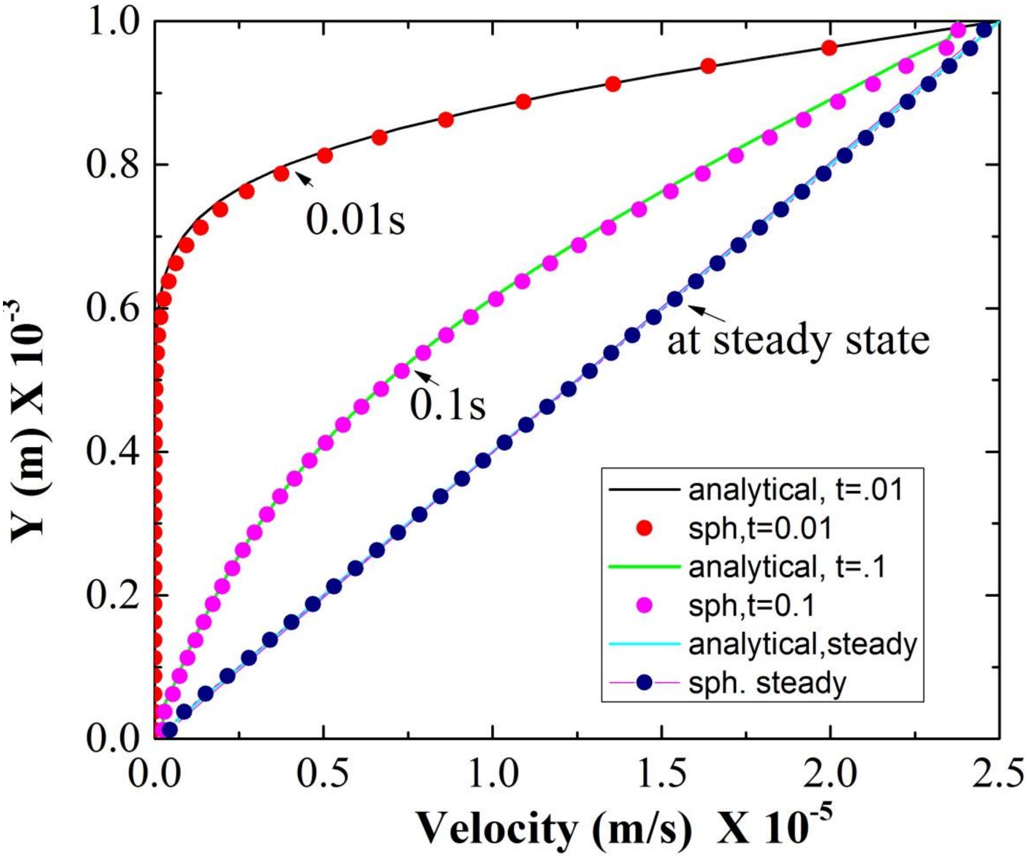

Figure 2.11 Velocity profiles for coquette flow by the study.

2.13.2 Shear cavity problem

The shear cavity involves fluid flow in a closed square generated by moving the upper side of the square at a constant velocity. The flow will reach a steady state and form a recirculation pattern. Figure 2.12 describes the initial conditions for the shear cavity flow. For the simulation, length of the square 10^{-3} m, dynamic viscosity of fluid μ 10^{-3} N.s/m^2, density of fluid ρ 1000kg/m^3 were taken. Total 1600 particles were used to represent the shear cavity in the study. Additionally, 320 repulsive boundary particles were used to define the boundary .The velocity of the upper top side was 10^{-3}m/s. The duration of each time step was taken as 5 x 10^{-5} second, and simulated for 3000 steps. Table 2.2 summarizes the parameters for the shear cavity simulation. Figure 2.12 describe the condition for generation shear cavity.

Table 2.2 Summary of parameters used for shear cavity simulation.

Number of fluid particles, N	1600
Initial particle spacing (m), Δd	0.000025
Smoothing length (m), h	0.00002525
Density (kg/m^3), ρ	1000
Dynamic viscosity of fluid (N.s/m^2) , μ	10^{-3}
Average velocity coefficient, ε	0.30
Boundary type	Repulsive
Duration of a time step(s), Δt	5 x 10^{-5}

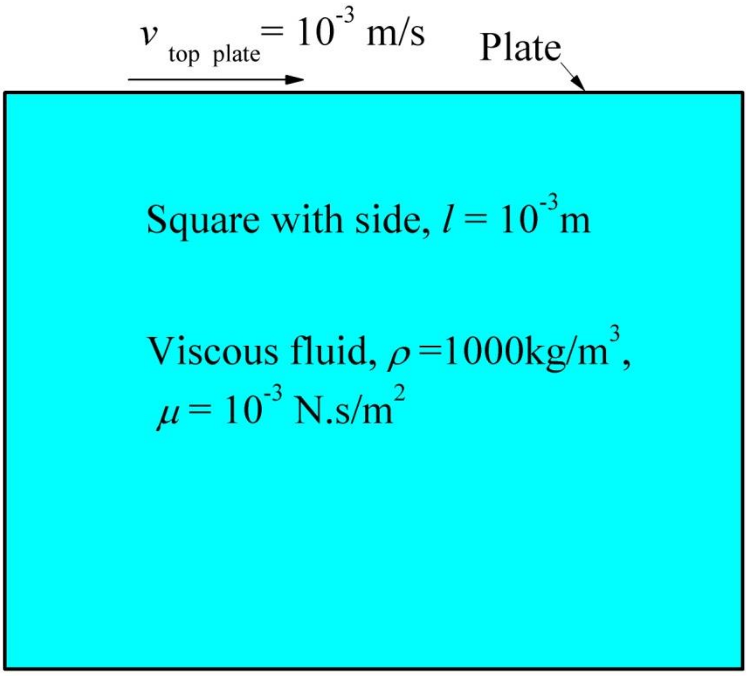

Figure 2.12 Criteria for shear cavity flow.

Figure 2.13 shows the particle velocity distributions for shear cavity. Figure 2.14 shows velocity distributions for shear cavity. From both the figures typical recirculation pattern for shear cavity can be observed.

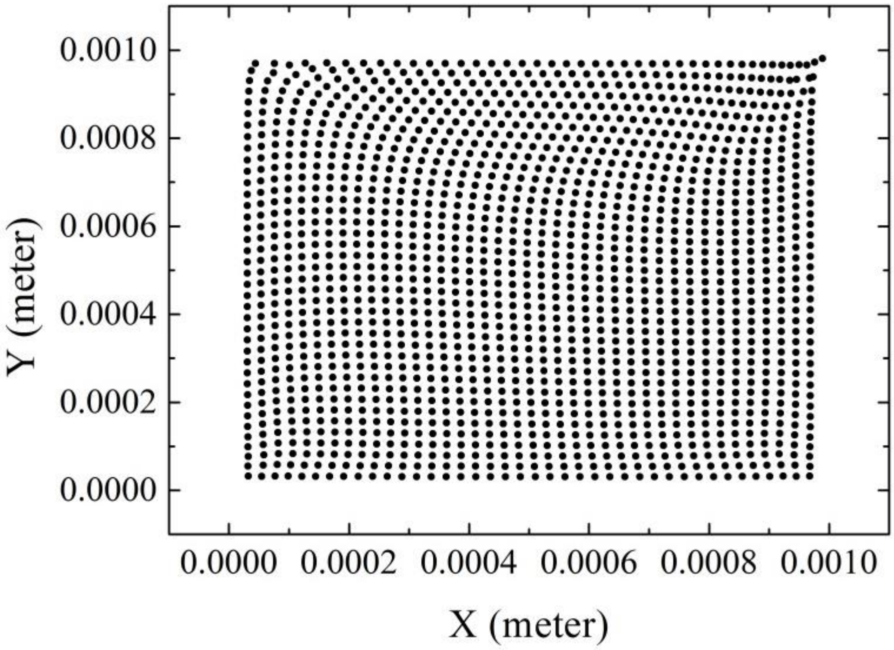

Figure 2.13 Particle distributions at steady state.

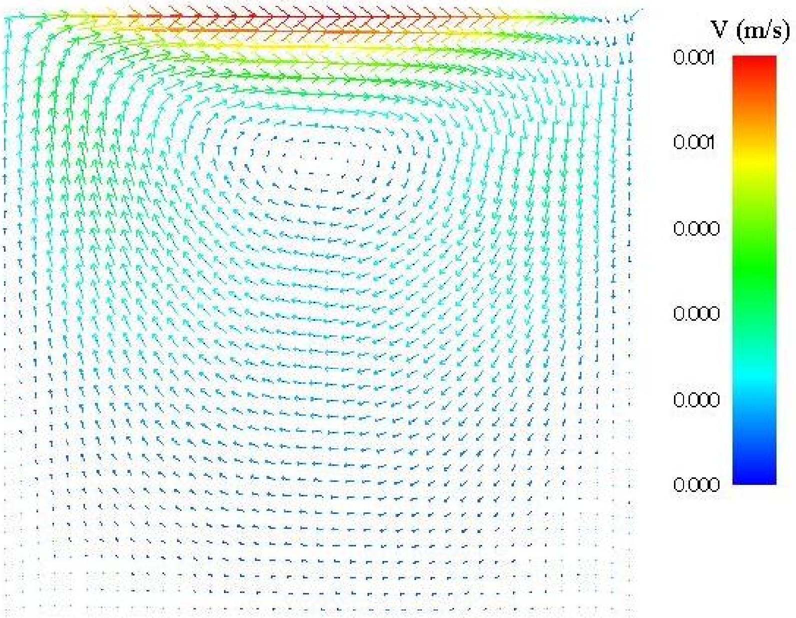

Figure 2.14 Velocity distributions at steady state.

Figure 2.15 shows the non-dimensional vertical velocity profile along the horizontal centerline of the shear cavity. Solution were done by FDM and SPH by Liu and Liu (2003). He compared the SPH solution with FDM , as its accuracy for low Reynolds number is excellent. The study has also plotted the same as in figure 2.16 and found excellent match with FDM.

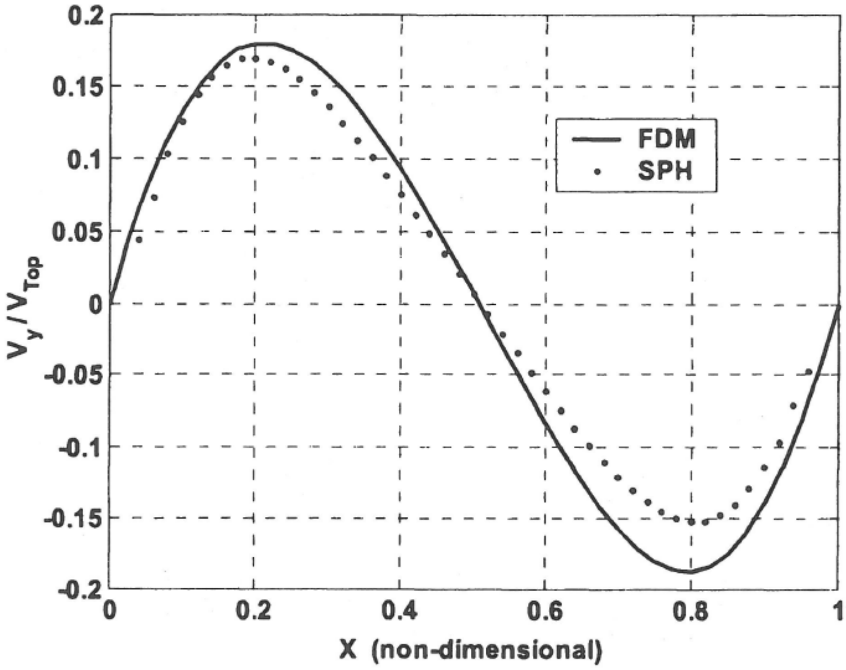

Figure 2.15 Non-dimensional vertical velocities along the horizontal centerline of shear cavity. [courtesy: Liu & Liu (2003)]

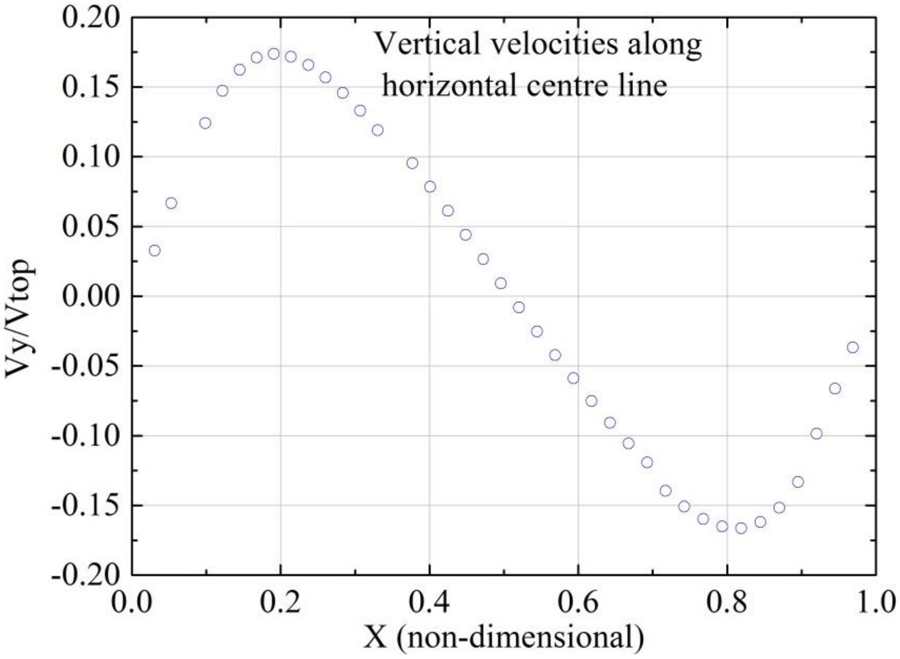

Figure 2.16 Non-dimensional vertical velocities along the horizontal centerline of shear cavity by the SPH code.

Similarly, horizontal velocity along the vertical centerline by FDM was plotted in figure 2.17. Solution by the study as in figure 2.18 matches excellently with the FDM simulation.

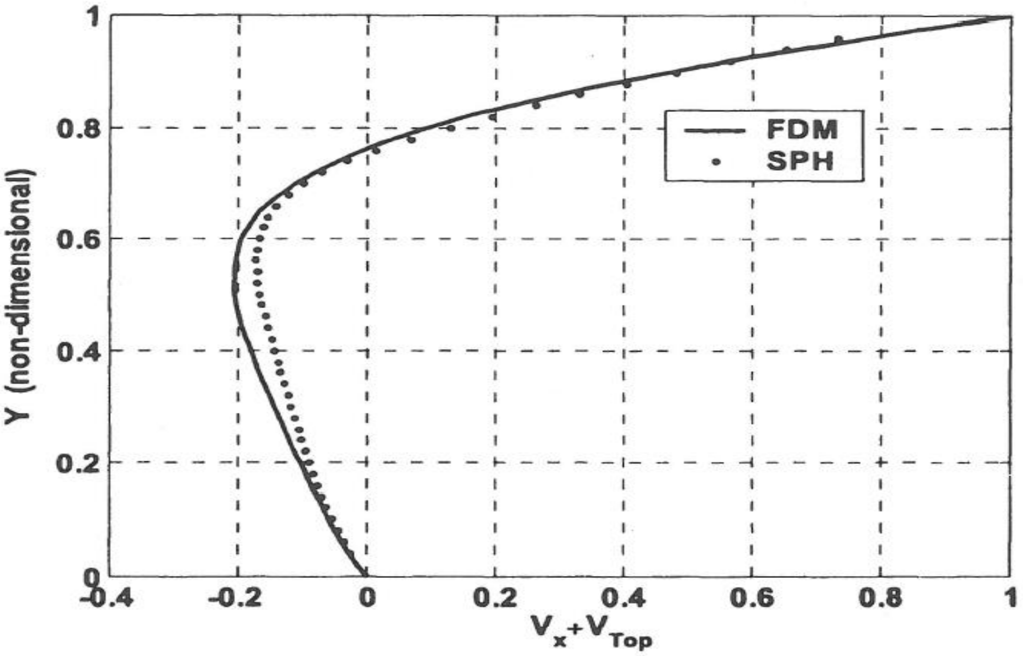

Figure 2.17 Non-dimensional horizontal velocities along the vertical centerline of shear cavity. [courtesy: Liu & Liu (2003)]

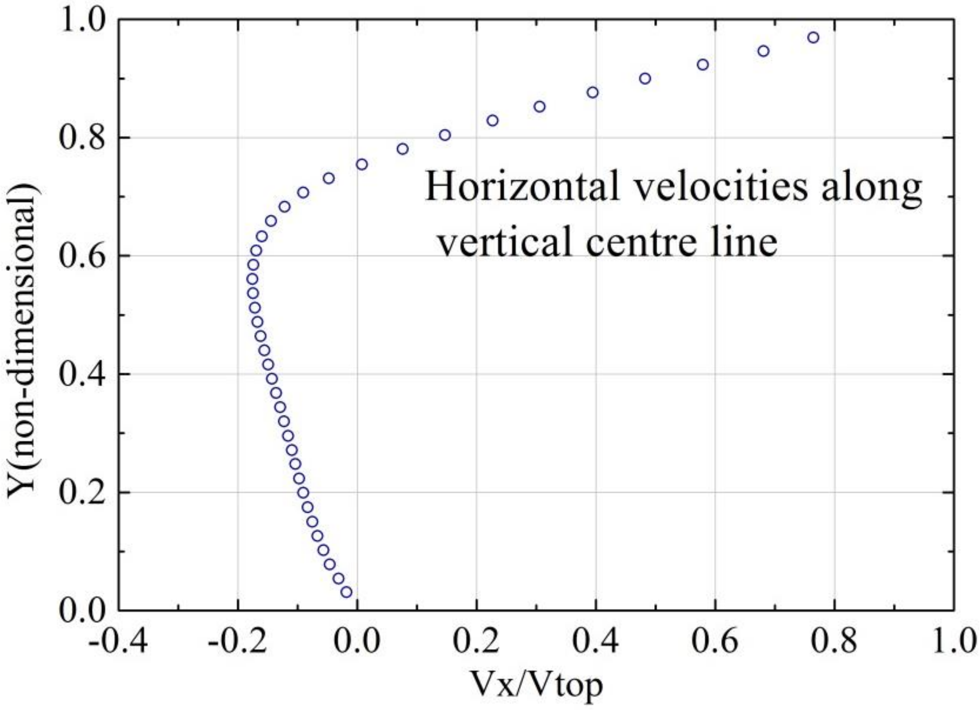

Figure 2.18 Non-dimensional horizontal velocities along the vertical centerline of shear cavity by the SPH code.

2.13.3 Dam break flow

The study has simulated dam break flow to check the ability to simulate free surface flow. Right wall of a 0.6m X 0.6m size water column was suddenly opened generating the dam break flow. The study has used 60 X 60 particles to represent the water column. The dimension of each particle 0.01m X 0.01 m, density of each particle 1000 kg/m^3, were taken.

Duration of each time step was 10^{-4} second, and simulation was run for 0.60 seconds. Horizontal wall was represented by the non-slip boundary particles and vertical wall was represented by the symmetric boundary particles. Figure 2.19 shows the dam break flow just after generation.

Table 3.3 Summary of parameters used for bam break flow.

Number of soil particles, N	3600
Initial particle spacing (m), Δd	0.01
Smoothing length (m)	0.012
Duration of a time step (s), Δt	0.0001
Density (kg/m^3), ρ	1000
Artificial viscosity parameter α, β	0.06, 0
Average velocity coefficient, ε	0.01
Boundary type at rigid base	Non-slip
Boundary type at vertical wall	symmetric

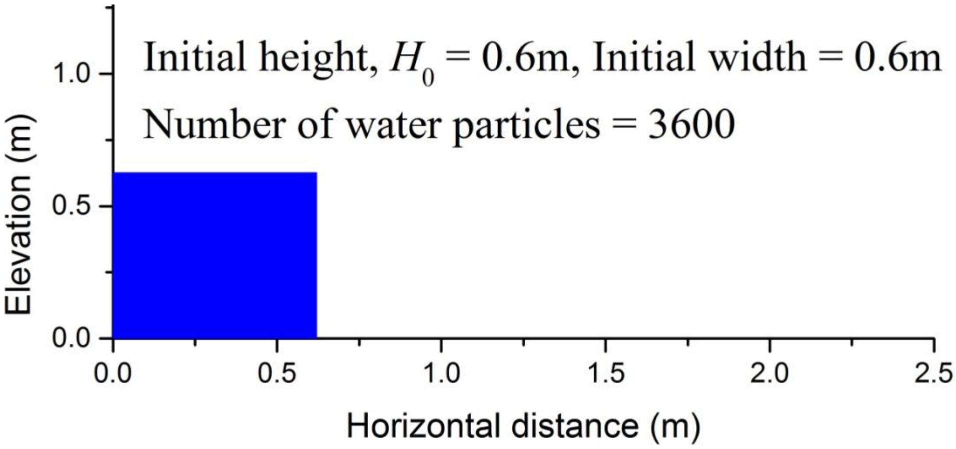

Figure 2.19 Simulation of water dam break at time 0.1 second.

Figure 2.20 shows the dam break profiles for representative times. It was found from visual observation that free surfaces generated by the SPH simulation match natural dam break flow pattern. So, it can be said that SPH code has the ability to generate free surface flow.

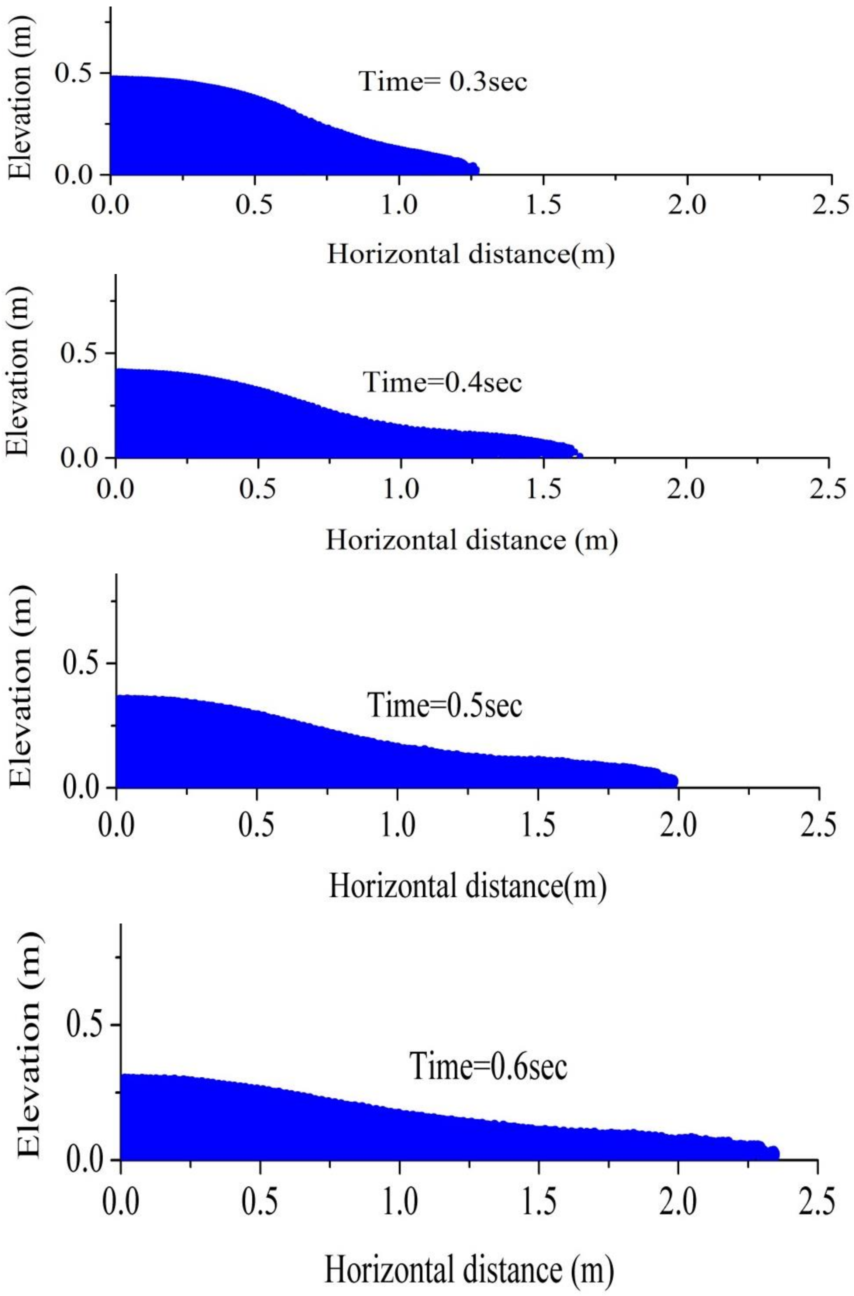

Figure 2.20 Progressive profiles for dam break flow by SPH.

Figure 2.21 shows the velocity distributions for the dam break flow simulated by SPH. Analytically, the approximate maximum velocity for dam break is $\sqrt{2gH_0}$, here g = 9.81 m/s^2, H_0 is 0.60 m, maximum velocity becomes 3.5 m/s. If we take average of the particle velocities from the wave front, it is almost same as the analytical values.

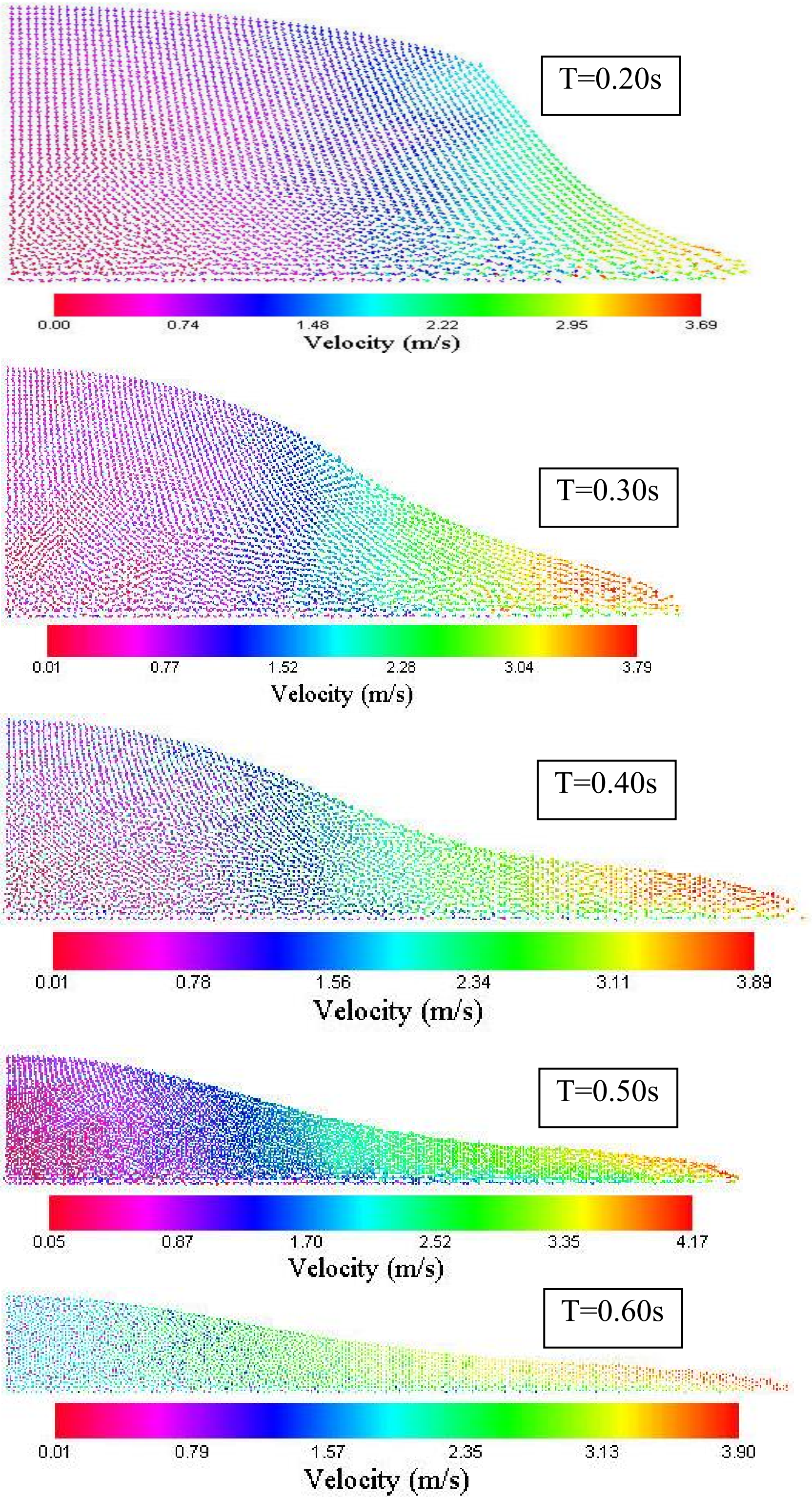

Figure 2.21 Velocity distributions for dam break flow by SPH.

Figure 2.22 and 2.23 show the comparison of wave fronts and elevation with experiment done by Martin & Moyce (1953) as cited by Monaghan (1994). The experimental data used here were found from Monaghan (1994).The wave fronts and elevations were normalized with respect to the initial height H_o, of the water column. Additionally, time was made dimensionless by t*(*g*/*H*$_o$) 1/2. It was found that results of the SPH code match nicely with experiment data.

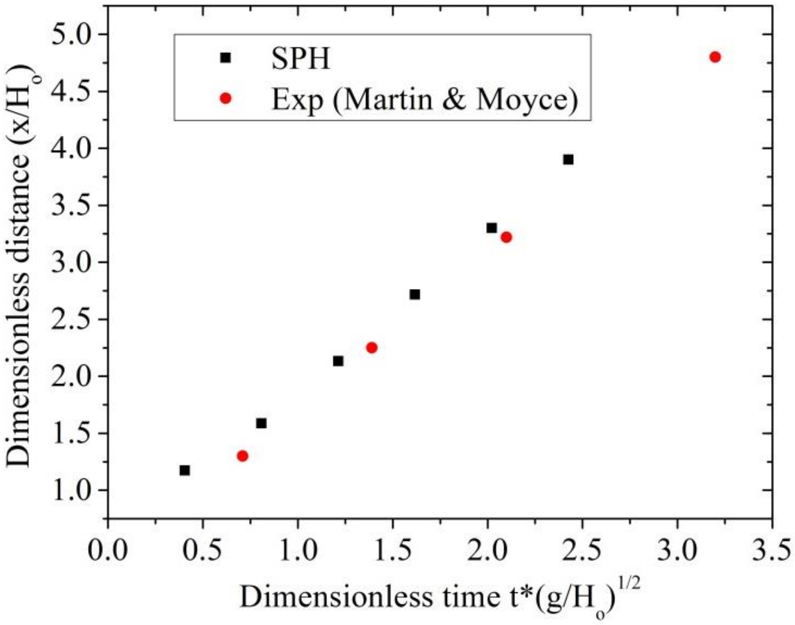

Figure 2.22 Comparison of wave front of the dam break with experiment.

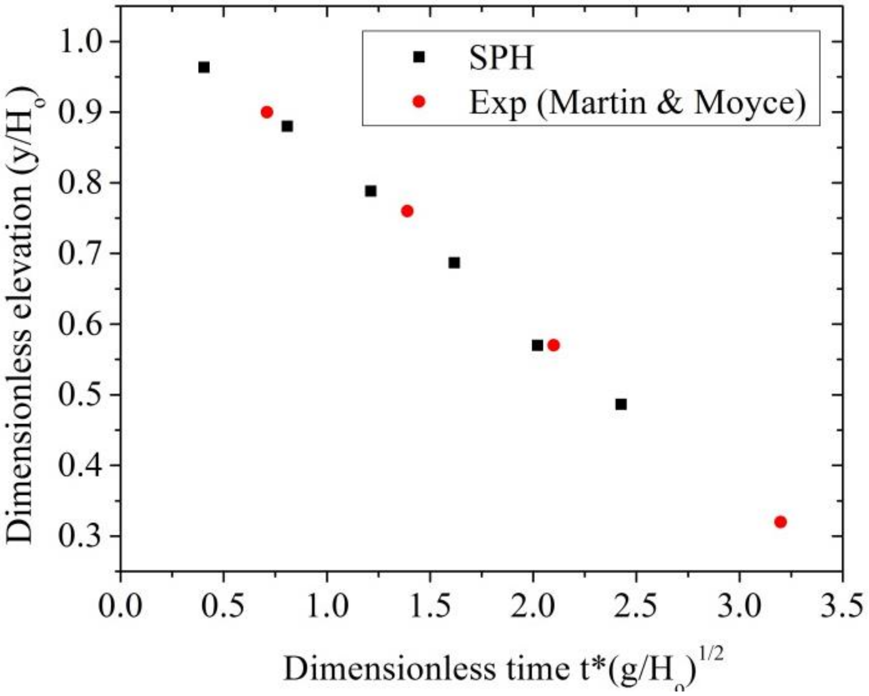

Figure 2.23 Comparison of elevation of the dam break with experiment.

2.14 Summary

The chapter has described fundamentals of the SPH in general and for fluid in particular. It has also described artificial viscosity, artificial compressibility, and equation of state, boundary definition, and duration of time step, and Leap-Frog algorithm for time integration that are important for implementation of the code. Moreover, it has presented the simulation results of coquette flow, shear cavity and dam break flow. Simulation results from the SPH code were found okay with comparisons to corresponding analytical or experimental results. Efficiency of the SPH code was found quite satisfactory to proceed for further applications.

CHAPTER 3

FORMULATIONS OF SPH FOR SOIL

3.1 Introduction

Chapter 3 discusses the soil constitutive relationship with Drucker-Prager (D-P) failure criteria. It contains the typical numerical errors appeared while implementing D-P model reported by literature. Some numerical tests performed by the developed SPH code were compared with analytical and experimental solutions. In this way verification of the developed SPH code for soils was accomplished in this chapter.

3.2 Soil constitutive model

The study has modelled the geo-material as elastic-perfectly plastic material. The definition of strain rate $\dot{\varepsilon}^{\alpha\beta}$ is

$$\dot{\varepsilon}^{\alpha\beta} = \frac{1}{2}\left(\frac{\partial v^{\alpha}}{\partial x^{\beta}} + \frac{\partial v^{\beta}}{\partial x^{\alpha}}\right) \qquad (3.1)$$

Moreover, the strain rate is combination of elastic strain rate and plastic strain rate.

$$\dot{\varepsilon}^{\alpha\beta} = \dot{\varepsilon}_e^{\alpha\beta} + \dot{\varepsilon}_p^{\alpha\beta} \qquad (3.2)$$

The elastic strain rate is calculated by the generalized Hooke's law:

$$\dot{\varepsilon}_e^{\alpha\beta} = \frac{\dot{s}'^{\alpha\beta}}{2G} + \frac{1-2v}{3E}\,\dot{\sigma}'^{\gamma\gamma}\delta^{\alpha\beta} \qquad (3.3)$$

Where, $\dot{s}'^{\alpha\beta}$ is the deviatoric stress rate and $\dot{\sigma}'^{\gamma\gamma}$ is the summation of the three normal stress rate components.

$$s'^{\alpha\beta} = \sigma'^{\alpha\beta} - 1/3\sigma'^{\gamma\gamma}\delta^{\alpha\beta} \qquad (3.4)$$

Here E is Young's modulus; G is the shear modulus. The plastic strain rate is computed by using the plastic flow rule

$$\dot{\varepsilon}_p^{\alpha\beta} = \dot{\lambda}\,\frac{\dot{\partial} g_p}{\partial \sigma'^{\alpha\beta}} \qquad (3.5)$$

Where $\dot{\lambda}$ is the rate of change of plastic multiplier and g_p is the plastic potential function that specifies the direction to which plastic strain will develop. For non-associated type flow rule g_p does not coincide with the yield function f of the material. The plastic multiplier λ has to satisfy the following conditions of the yield criteria:

- $\lambda = 0$ when $f < 0$ or $f = 0$ and $df < 0$ (elastic or plastic unloading)
- $\lambda > 0$ when $f = 0$ and $df < 0$ (plastic loading)

The value of the plastic multiplier λ can be determined from consistency condition

$$df = \frac{\partial f}{\partial \sigma'^{\alpha\beta}} d\sigma'^{\alpha\beta} = 0 \qquad (3.6)$$

The explanation of the above equation can be done

$$f\left(\sigma'^{\alpha\beta} + d\sigma'^{\alpha\beta}\right) = f\left(\sigma'^{\alpha\beta}\right) + df = f\left(\sigma'^{\alpha\beta}\right) \qquad (3.7)$$

The total strain rate tensor can now be written

$$\dot{\varepsilon}^{\alpha\beta} = \frac{\dot{s}'^{\alpha\beta}}{2G} + \frac{1-2\upsilon}{3E}\,\dot{\sigma}'^{\gamma\gamma}\delta^{\alpha\beta} + \dot{\lambda}\,\frac{\partial g_p}{\partial \sigma'^{\alpha\beta}} \qquad (3.8)$$

Now the general stress-strain relationship for an elastic-perfectly plastic material can be written as :

$$\frac{d\sigma'^{\alpha\beta}}{dt} = 2G\dot{e}^{\alpha\beta} + K\dot{\varepsilon}^{\gamma\gamma}\delta^{\alpha\beta} - \dot{\lambda}\left[\left(K - \frac{2G}{3}\right)\frac{\partial g_p}{\partial^{mn}}\delta^{mn}\delta^{\alpha\beta} + 2G\frac{\partial g}{\partial \sigma^{\alpha\beta}}\right] \qquad (3.9)$$

Where α , β are free indices and *m, n* are dummy indices.

$$\dot{e}^{\alpha\beta} = \dot{\varepsilon}^{\alpha\beta} - \frac{1}{3}\dot{\varepsilon}^{\alpha\beta}\delta^{\alpha\beta} \qquad (3.10)$$

$$K = \frac{E}{3(1-2\nu)} \qquad (3.11)$$

and $$G = \frac{E}{2(1+\nu)} \qquad (3.12)$$

3.3 Drucker-Prager model

The study has selected the Drucker-Prager (D-P) failure criteria to model the geo-material. The detailed discussions on Drucker-Prager (D-P) failure criteria can be found in Bui et al. (2008a). The yield criterion for the D-P is expressed through the following equation:

$$f(I_1,\, J_2) = \sqrt{J_2} + I_1\alpha_{\emptyset} - k_c = 0 \qquad (3.13)$$

Where I_1 and J_2 are the first and second invariants of the stress tensor, that are defined by

$$I_1 = \sigma'^{xx} + \sigma'^{yy} + \sigma'^{zz} \qquad (3.14)$$

and $$J_2 = \frac{1}{2}s'^{\alpha\beta}s'^{\alpha\beta} \qquad (3.15)$$

α_{ϕ} and k_c are two D-P constants, are related with soil cohesion *c* and frictional angle ϕ with

$$\alpha_{\emptyset} = \frac{tan\emptyset}{\sqrt{9+12tan^2\emptyset}} \qquad (3.16)$$

$$k_c = \frac{3c}{\sqrt{9+12tan^2\emptyset}} \qquad (3.17)$$

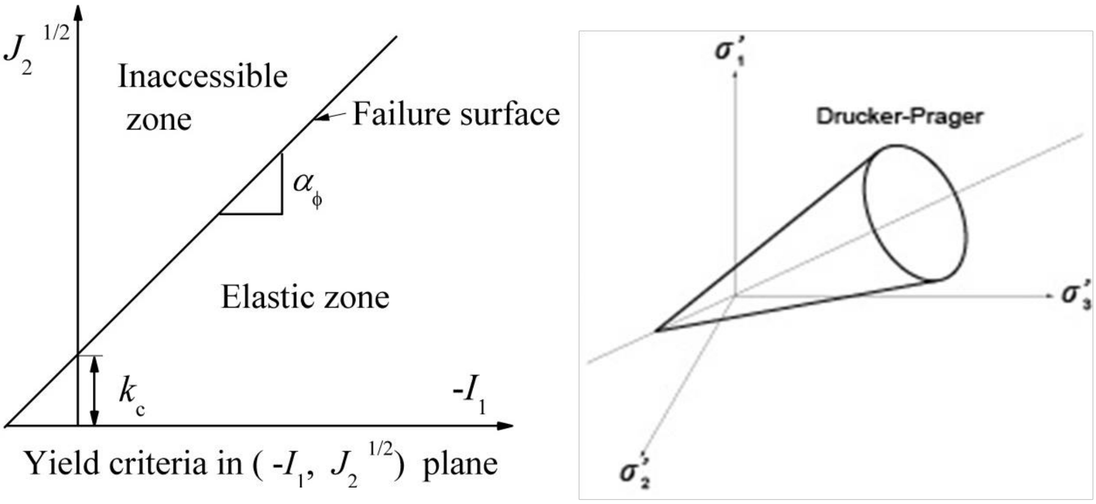

Figure 3.1 Drucker-Prager yield criteria.

In the study non-associated plastic flow rule is adopted where plastic potential function is given by

$$g_p = \alpha_\psi I_1 + \sqrt{J_2} - constant \qquad (3.18)$$

$$\alpha_\psi = \frac{tan\psi}{\sqrt{9+12tan^2\psi}} \qquad (3.19)$$

Where ψ is dilation angle.

The form of stress –strain relationship considering Jaumann stress rate for the D-P model is

$$\frac{d\sigma'^{\alpha\beta}}{dt} = \sigma'^{\alpha\gamma}\dot{\omega}^{\beta\gamma} + \sigma'^{\gamma\beta}\dot{\omega}^{\alpha\gamma} + 2G\dot{e}^{\alpha\beta} + K\dot{e}^{\gamma\gamma}\delta^{\alpha\beta} - \dot{\lambda}\left[3K\alpha_\psi\delta^{\alpha\beta} + \frac{G}{\sqrt{J_2}}s'^{\alpha\beta}\right] \qquad (3.20)$$

$$\dot{\omega}^{\alpha\beta} = \frac{1}{2}\left(\frac{\partial v^\alpha}{\partial x^\beta} - \frac{\partial v^\beta}{\partial x^\alpha}\right) \qquad (3.21)$$

$$\dot{\varepsilon}^{\alpha\beta} = \frac{1}{2}\left(\frac{\partial v^\alpha}{\partial x^\beta} + \frac{\partial v^\beta}{\partial x^\alpha}\right) \qquad (3.22)$$

$$\dot{\lambda} = \frac{3\alpha_\emptyset K\dot{\varepsilon}^{\gamma\gamma} + \frac{G}{\sqrt{J_2}}s'^{\alpha\beta}\dot{\varepsilon}^{\alpha\beta}}{9\alpha_\emptyset K\alpha_\psi + G} \qquad (3.23)$$

3.4 Numerical errors in D-P model implementation

Two common type of numerical errors arising during D-P implementation are solved in the study according to Bui et al. (2008a).

3.4.1 Tension cracking treatment

If the stress state of the material at time step *n* exceeds the apex of the yield surface, satisfying the condition:

$$-\alpha_\emptyset I_1^n + k_c < 0 \qquad (3.24)$$

Under such condition shearing stress components are kept unchanged and adjustment of the normal stress components are performed :

$$\tilde{\sigma}'^{xx}_n = \sigma'^{xx}_n - \frac{1}{3}\left(I_1^n - \frac{k_c}{\alpha_\emptyset}\right) \qquad (3.25)$$

$$\tilde{\sigma}'^{yy}_n = \sigma'^{yy}_n - \frac{1}{3}\left(I_1^n - \frac{k_c}{\alpha_\emptyset}\right) \qquad (3.26)$$

$$\tilde{\sigma}'^{zz}_n = \sigma'^{zz}_n - \frac{1}{3}\left(I_1^n - \frac{k_c}{\alpha_\emptyset}\right) \qquad (3.27)$$

3.4.2 Stress-scaling back procedure

As in the figure 3.2 when stress states reaches from A to B , it is scaled down to go to C. the scaling factor at time step *n* is defined by

$$r^n = \frac{-\alpha_\emptyset I_1^n + k_c}{\sqrt{J_2^n}} \qquad (3.28)$$

When stress state of material exceeds the yield surface defined by the following conditions

$$-\alpha_\emptyset I_1^n + k_c < \sqrt{J_2^n} \qquad (3.29)$$

Under such stress condition deviatoric shear stress components are scaled down but normal stress components I_1 are kept unchanged

$$\tilde{\sigma}'^{xx}_n = r^n s'^{xx}_n + 1/3\sqrt{J_2^n} \qquad (3.30)$$

$$\tilde{\sigma}'^{yy}_n = r^n s'^{yy}_n + 1/3\sqrt{J_2^n} \qquad (3.31)$$

$$\tilde{\sigma}'^{zz}_n = r^n s'^{zz}_n + 1/3\sqrt{J_2^n} \qquad (3.32)$$

$$\tilde{\sigma}'^{xy}_n = r^n s'^{xy}_n \qquad (3.33)$$

$$\tilde{\sigma}'^{xz}_n = r^n s'^{xz}_n \qquad (3.34)$$

$$\tilde{\sigma}'^{yz}_n = r^n s'^{yz}_n \qquad (3.35)$$

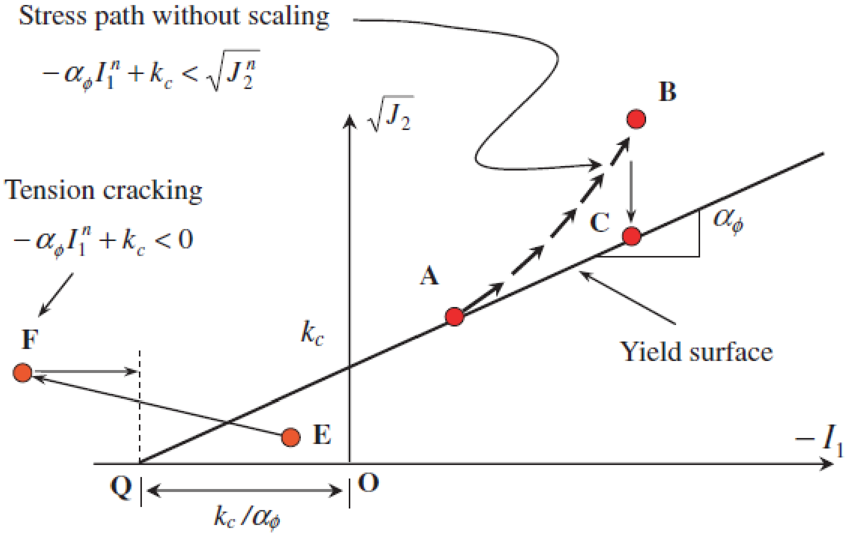

Figure 3.2 stress states in tension cracking (E to F) and imperfectly plastic (A to B) responses

3.4.3 Artificial stress

In SPH simulation, formations of clumps are termed as the tensile instability. It was first reported by Swegle et al. (1995). To remove tensile instability problem in the SPH, solution proposed by Monaghan (2000) and Grey et al. (2001) is used here. In this solution, small repulsive forces between the neighboring particles are introduced that come too close to each other. Let us write the momentum equation with artificial stress.

$$\frac{Dv_i^\alpha}{Dt} = \sum_{j=1}^{N} m_j \left(\frac{\sigma_i^{\alpha\beta}}{\rho_i^2} + \frac{\sigma_j^{\alpha\beta}}{\rho_j^2}\right)\frac{\partial W_{ij}}{\partial x_i^\beta} - \Pi_{ij}\,\delta^{\alpha\beta} + f_{ij}^n\left(R_i^{\alpha\beta} + R_j^{\alpha\beta}\right)\frac{\partial W_{ij}}{\partial x_i^\beta} + g^\alpha \qquad (3.36)$$

In equation (3.36), $f_{ij}^n\left(R_i^{\alpha\beta} + R_j^{\alpha\beta}\right)$ term is the artificial stress term. Where, n is an exponent dependent on the smoothing kernel , according to Bui et al. (2008a) the value is 2.55 for cubic spline function, Grey et al. (2001) has used as 4; f_{ij} is the repulsive force term and defined according to Monaghan (2000):

$$f_{ij} = \frac{W_{ij}}{W(\Delta d, h)} \qquad (3.37)$$

Where Δd is the initial particle spacing.

For two dimensional cases the artificial stress tensor $R_i^{\alpha\beta}$ for the i particle in the reference coordinate system is computed from the principal components $R_i'^{xx}$ and $R_i'^{yy}$ by the standard transformation:

$$R_i^{xx} = R_i'^{xx}\cos^2\theta_i + R_i'^{yy}\sin^2\theta_i \qquad (3.38)$$

$$R_i^{yy} = R_i'^{xx}\sin^2\theta_i + R_i'^{yy}\cos^2\theta_i \qquad (3.39)$$

$$R_i^{xy} = \left(R_i'^{xx} - R_i'^{yy}\right)\cos\theta_i\,\sin\theta_i \qquad (3.40)$$

Where θ_i is defined by

$$tan2\theta_i = \frac{2\sigma_i^{xy}}{\sigma_i^{xx} - \sigma_i^{yy}} \quad (3.41)$$

Where σ_i^{xx}, σ_i^{yy}, σ_i^{xy} are stress tensor componenets of *i* particle in the reference coordinate. The diagonal components of the artificial stress tensor are calculated according to Grey et al (2001)

$$R_i'^{xx} = \begin{cases} -\varepsilon \frac{\sigma_i'^{xx}}{\rho_i^2}, \; if \; \sigma_i'^{xx} < 0 \; (tension) \\ 0, \; otherwise \end{cases} \quad (3.42)$$

Where ε is a constant ranging from 0 to 1. $\sigma_i'^{xx}$ is the principal stress tensor for *i* particle. The principal stress components can be found

$$\sigma_i'^{xx} = cos^2\theta\sigma_i^{xx} + \; 2\, cos\theta \; sin\theta\sigma_i^{xy} + sin^2\theta\sigma_i^{yy} \quad (3.43)$$

$$\sigma_i'^{yy} = sin^2\theta\sigma_i^{xx} - \; 2\, cos\theta \; sin\theta\sigma_i^{xy} + cos^2\theta\sigma_i^{yy} \quad (3.44)$$

3.5 Verification of SPH code for the D-P model

The study has implemented the D-P model by SPH. However, it is important to check whether the code is working correctly prior to application in the current research. The verification of the code is performed by simulating some problems that have analytical or experimental solutions.

3.5.1 Simple shear test

Simple shear test by SPH was first performed by Nonoyama (2011). Actually, simple shear test is a very effective way to check the accuracy of the code. To prove the accuracy of the code the study has also performed the simple shear test. Soil layer with 30cm X 30 cm area was represented by 900 particles. In the simulation soil layer was forcibly deformed with a constant velocity to represent the simple shear test condition. The parameters used in the simulation are summarized in table 3.1. The soil layer was given a constant horizontal velocity in the following way as shown in the figure 3.3.

$$v_x(m/s) = 0.01 * y \quad (3.37)$$

Measurements of stress, strain, stress invariants, were taken from the central area of the soil sample. The results of the simulations were compared with analytical solution of the failure surface for D-P model.

$$\sqrt{J_2} + I_1\alpha_{\emptyset} - k_c = 0 \quad \text{from equation (3.13)}$$

Table 3.1 Parameters used for simulation of simple shear test.

Number of soil particles, N	900
Initial particle spacing (m), $\varDelta d$	0.01
Smoothing length (m), h	0.012
Duration of a time step (s), $\varDelta t$	0.00001
Density (kg/m^3), ρ	1800
Artificial viscosity parameter α, β	1.0
Modulus of elasticity (MPa), E	15
Poisson's ratio, ν	0.35

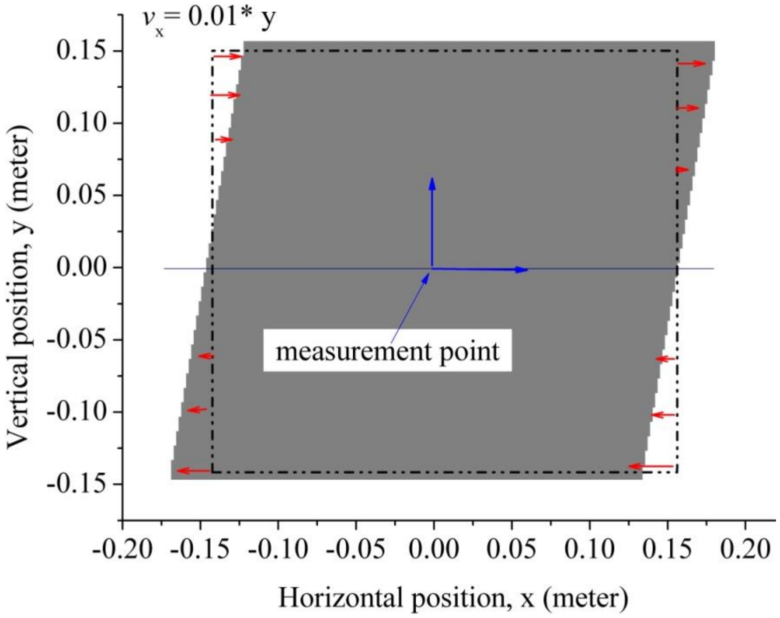

Figure 3.3 Initial and deformed shape during simple shear test by SPH.

Figure 3.4 shows the stress strain relationship for an elastic material. Stress-strain relationship is linear and slope of the line is the shear modulus *G* of the material. From the figure 3.4, *G* is found to be 5.55 MPa that matches exactly with the input value when obtained from modulus of elasticity *E* and Poisson's ratio.

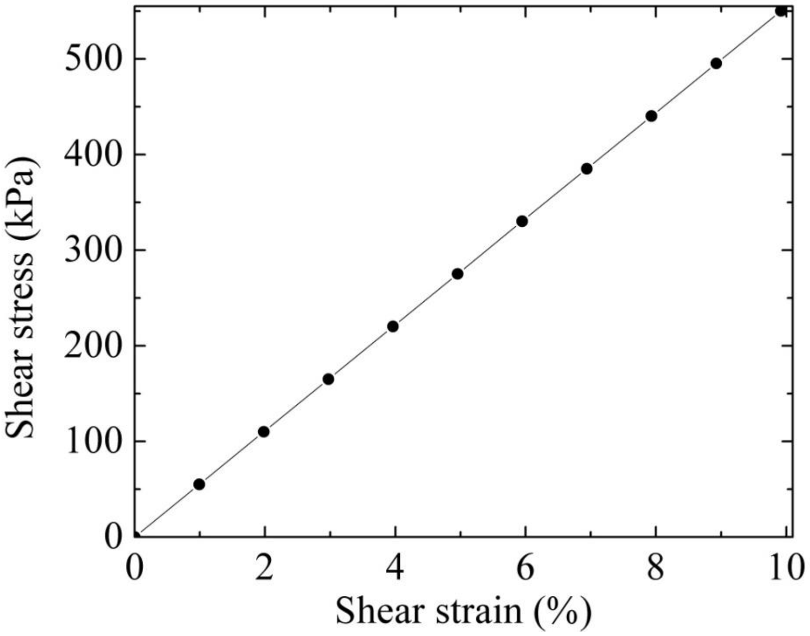

Figure 3.4 Stress strain relationship for elastic material from simple shear test by SPH.

Figure 3.5 describes the stress- strain relationships with frictional coefficient 30^0 for all cases but cohesion values were 0, 50 kPa, 100 kPa. It was found that with the increase of cohesion value the yield stress was found to increase. Moreover, the stress remained constant after reaching the failure surface.

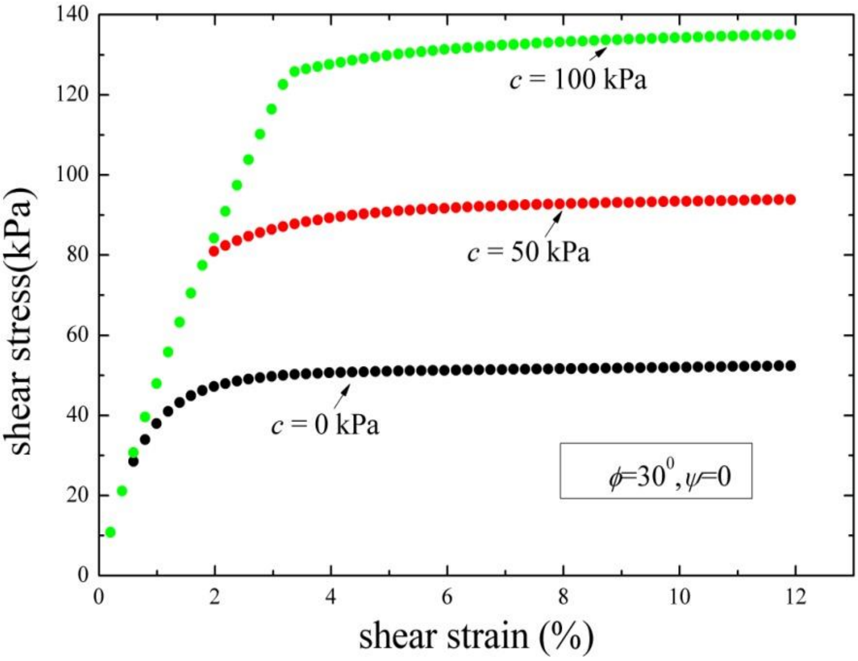

Figure 3.5 Shear stress and shear strain plot with different cohesion from the simple shear test by SPH.

Figure 3.6 shows the stress paths for same strength parameters as in figure 3.5. It was found that failure surface by SPH match satisfactorily with the analytical failure surface by equation

3.13. It was found that D-P constants α_{ϕ} and k_c from the failure surface by SPH were exactly same with those of the input values.

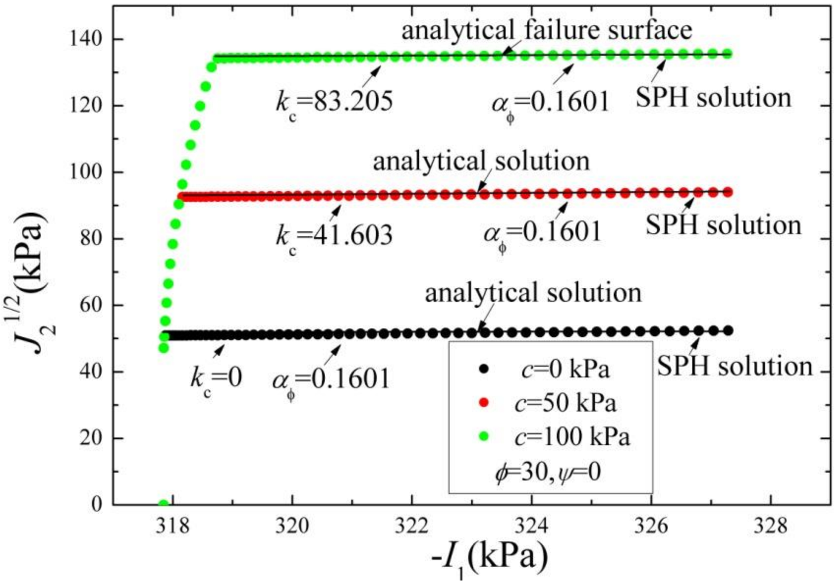

Figure 3.6 Stress paths from the simple shear test by SPH.

Figures 3.7 and 3.8 describe the results for simple shear test with initial confining pressure 5.3 kPa, 318 kPa and 530 kPa. Sterss and strain relationships were established in the figure 3.7. It was found that with increase of initial confining pressures the yield stress were also found to be increased. The analytical solutions for the failure surface with different confining pressures were found to match with the SPH solution as shown in Figure 3.8.

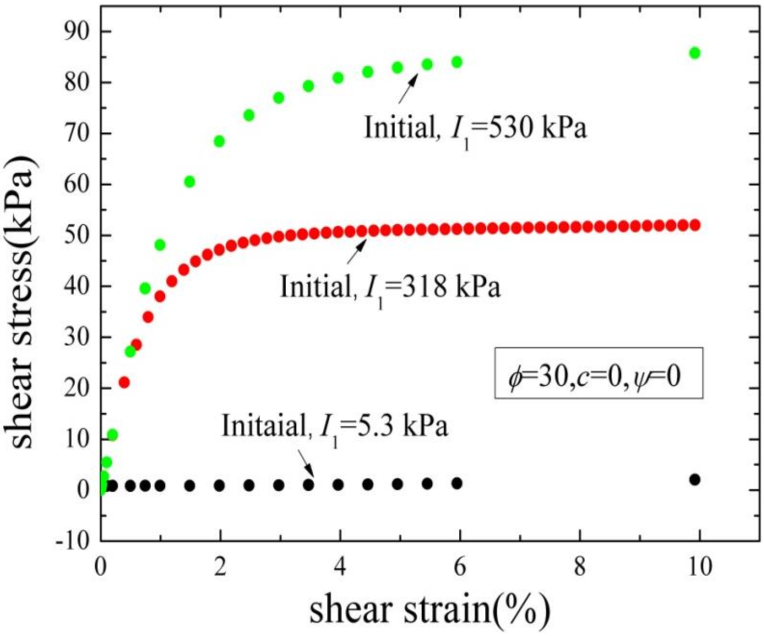

Figure 3.7 Shear stress and shear strain plot with different confining pressure from the simple shear test by SPH.

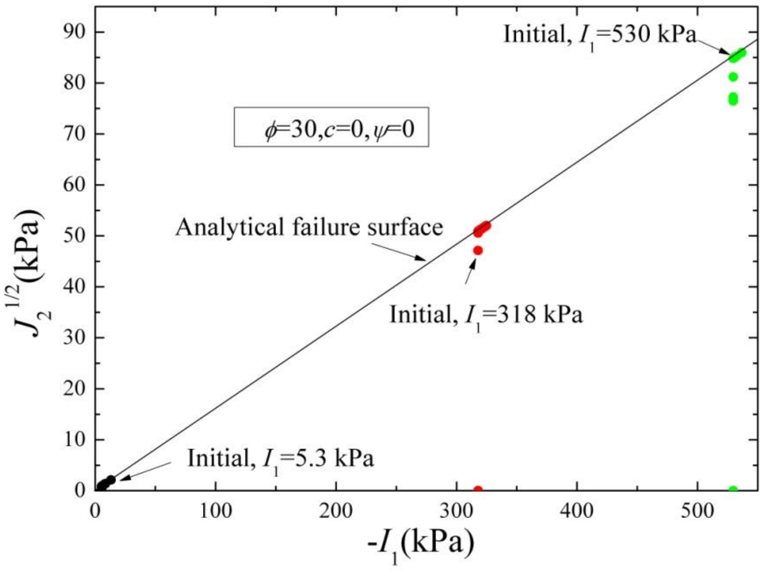

Figure 3.8 Stress paths for different confining pressure.

3.5.2 Granular flow

To check the efficiency of the developed SPH code the study has simulated the flow of granular material which was experimented by Bui et al. (2008a). In the original experiment, granular material was kept in a rectangular arrangement of 200mm X 100mm. Aluminum bars were used as the granular materials with diameter of 1mm and 1.5 mm , length 50 mm the material parameters used in the experiment is summarized in table 3.2.

Table 3.2 Parameters used for experiment. [Bui et al. (2008)]

Size of the rectangular granular material	200mm X 100 mm
Density (kg/m^3), ρ	2650
Frictional coefficient, ϕ	19.8^0
Bulk modulus of elasticity, K (Mpa)	0.70
Poisson's ration, ν	0.30

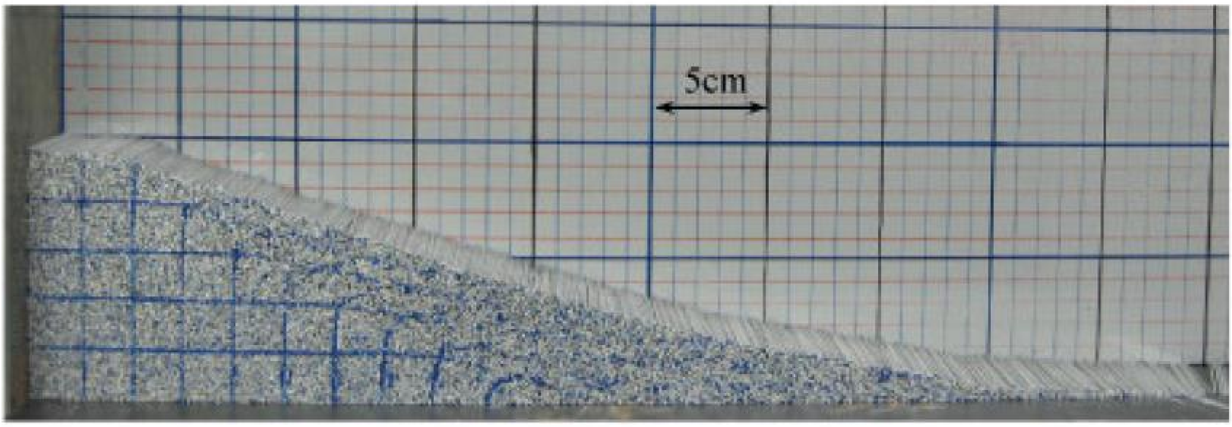

Figure 3.9 Non-cohesive soil collapse by Bui et al. (2008a)

In the SPH simulation, exactly same geometric and material properties were used with particle size of 0.0025m X 0.0025m. Parameters used in the simulations are summarized in the table 3.3. Initial arrangements are shown in the figure 3.10.

Table 3.3 Parameters used in the simulation

Number of particles representing granular material, *N*	3200
Initial spacing (m), Δd	0.0025
Smoothing length (m), *h*	0.003
Duration of a time step (s), Δt	10^{-5}
Boundary type at horizontal base	Non-slip boundary
Boundary type at vertical wall	Symmetric boundary
Artificial viscosity parameter α, β	0.1

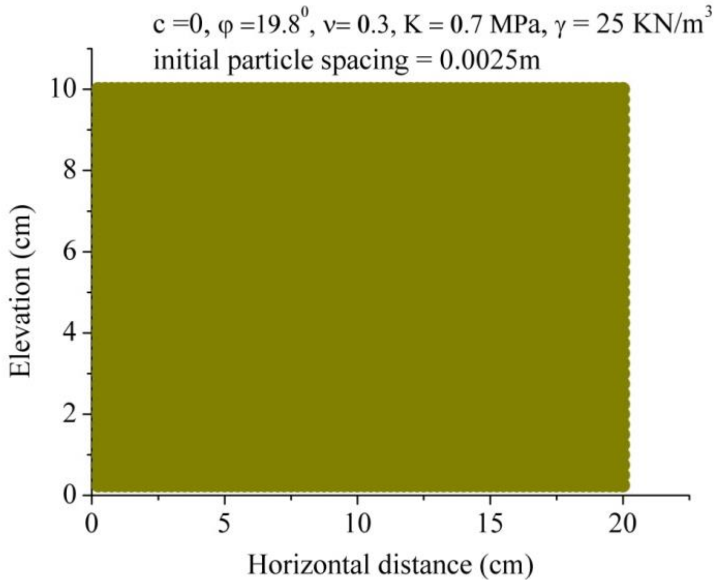

Figure 3.10 Initial arrangements for SPH simulation.

From the figures 3.11 to 3.12 progressive flow of the granular material are shown.

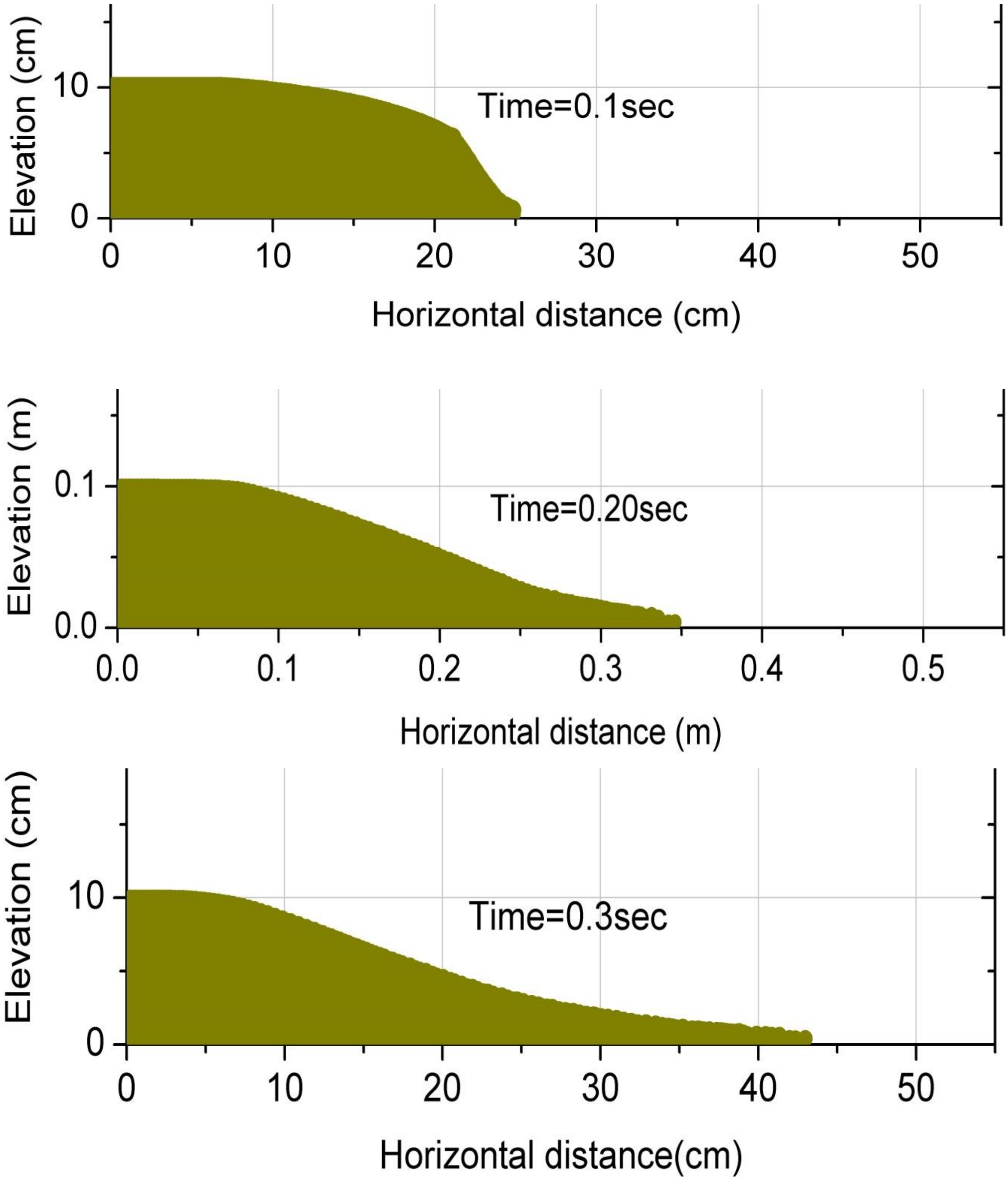

Figure 3.11 Progress of granular flow from 0.1 second to 0.30second.

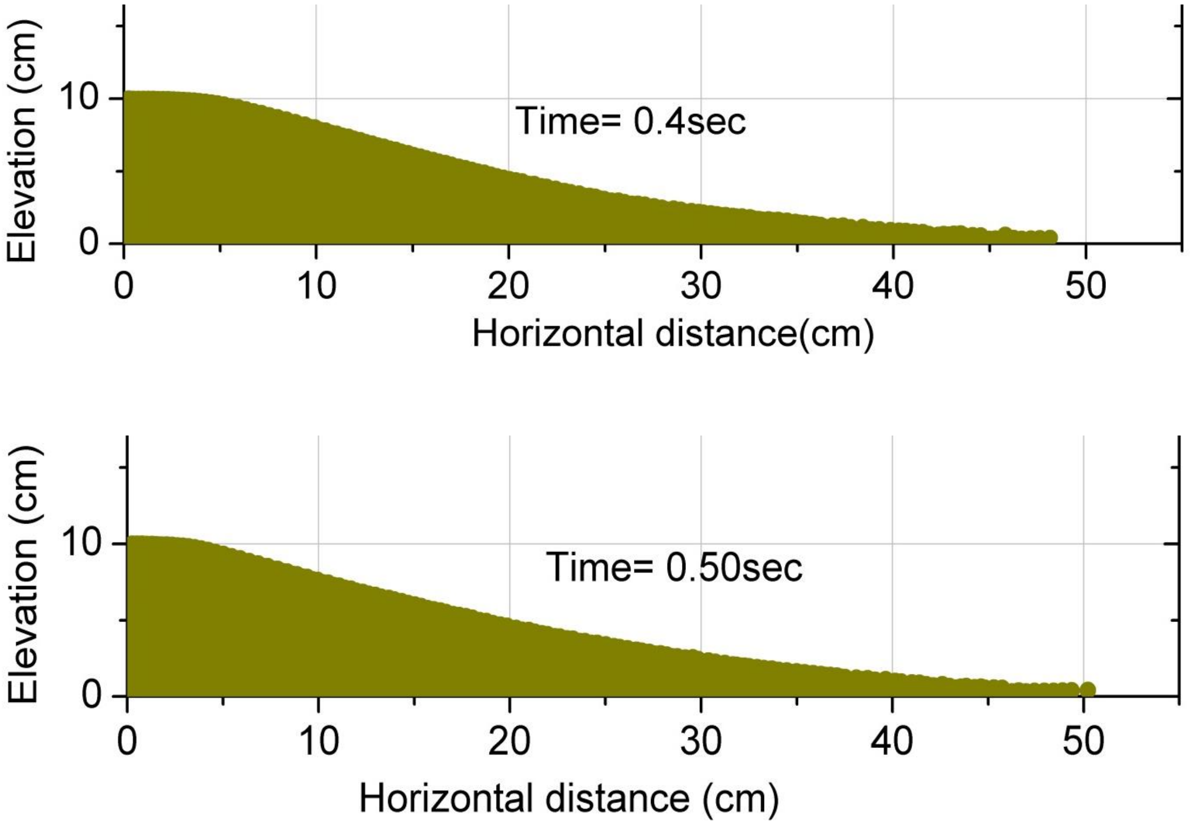

Figure 3.12 Progress of granular flow from 0.4 second to 0.50second.

However, for understanding of the granular flow it is important to visualize the failure surface. Figure 3.13 shows the progressive maximum shear strain distributions of the granular flow by the developed code. Although no data were available to check the progressive failure surface, however it shows the increase of maximum shear strain progressively. Additionally, it shows the failure surface of the granular flow.

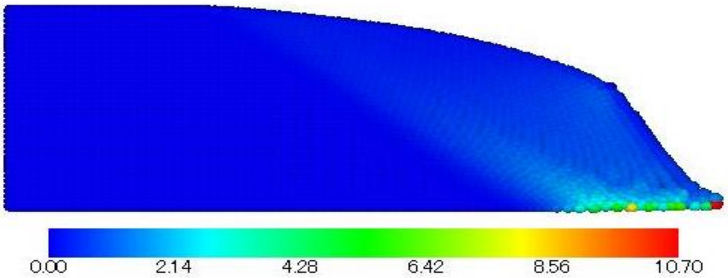

Max shear strain at 0.10 second flow

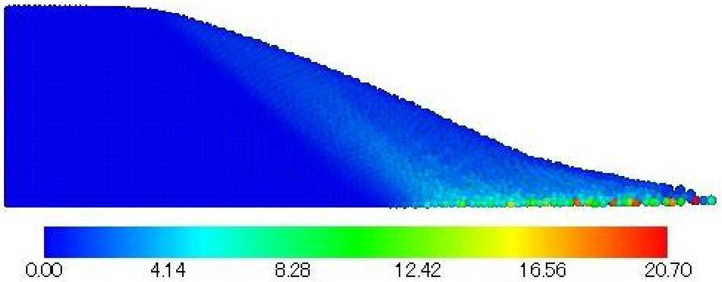

Max shear strain at 0.20 second flow

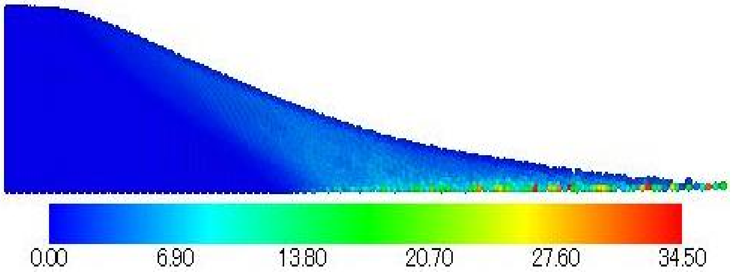

Max shear strain at 0.40 second flow

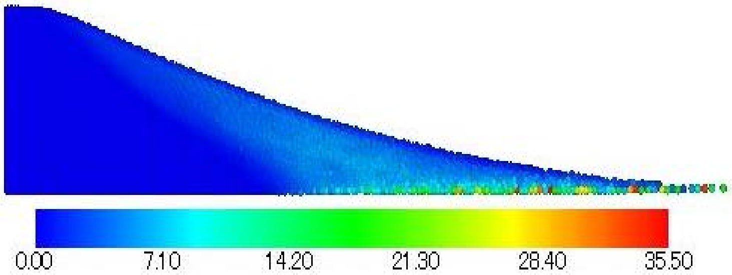

Max shear strain at 0.50 second flow

Figure 3.13 Distributions of maximum shear strains for granular flow by developed SPH code.

To check the accuracy of the developed SPH code deformed surface level generated by granular flow simulation was compared with the experiment. Figure 3.14 shows the comparison of the surface of the granular flow by the developed code with experiment and solution by Bui et al. (2008a). It was found that the SPH surface profile of the study matches nicely with both experimental and solution by Bui et al. (2008a).

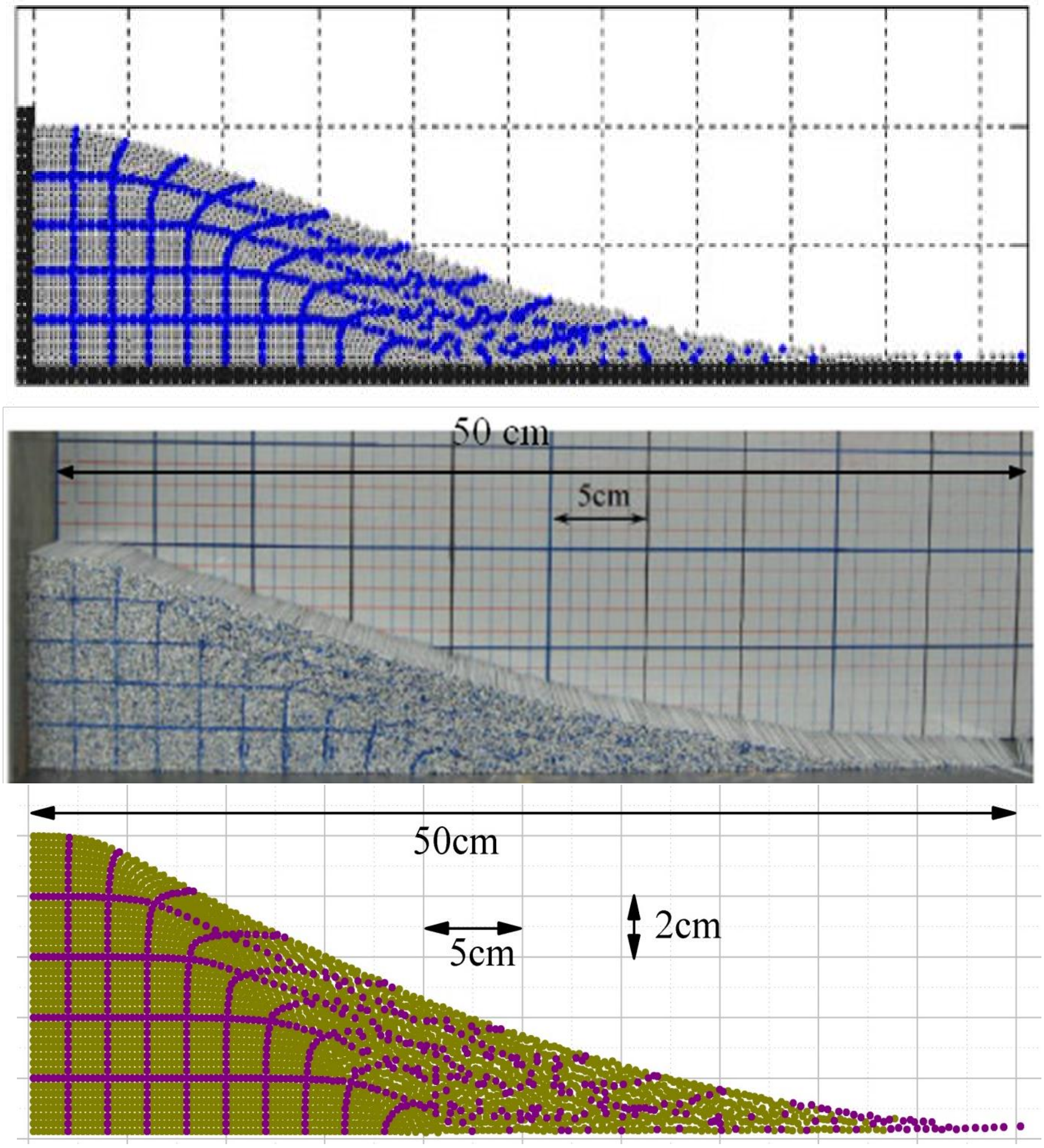

Figure 3.14 Comparison of the collapsed granular material among by the study with solution from Bui et al. (2008a) and the experiment. Upper figure is from Bui et al. (2008a), middle one is experiment, lower one is SPH solution by the study.

3.5.3 Bearing capacity test for soil

A rigid footing was allowed to settle into the soil layer at a constant rate. The mean stress below the footing was recorded with respect to the amount of settlement. Then it was plotted in the graph and checked with the analytical values. SPH solution was checked with the Prandtl solution for ultimate bearing capacity for the cohesive material

$$q_b = (2+\pi)c \cong 5.14\, c \qquad (3.38)$$

Here, q_b is the ultimate bearing capacity (N/m^2), c is cohesion (N/m^2). The parameters used for the simulations are summarized in table 3.4.

Table 3.4 Parameters used for SPH simulation of cohesive soil

Number of particles for soil, N	2500
Initial spacing (m), Δd	0.01
Gravity for cohesive material (m/s^2), g	0
Duration for a times step (s), Δt	10^{-5}
Boundary type at the rigid base	Non-slip boundary
Boundary type at the vertical walls	Symmetric boundary
Density of soil (kg/m3), ρ	1800
Cohesion values for cohesive soil (kPa), c	10, 15, 30, 50,100
Settlement rate of footing (m/s)	0.02
Width of footing (m), B_f	0.07

Figure 3.15 shows the arrangement for bearing capacity test for cohesive soils. Figure 3.15 show the deformation of the cohesive soil for footing settlement.

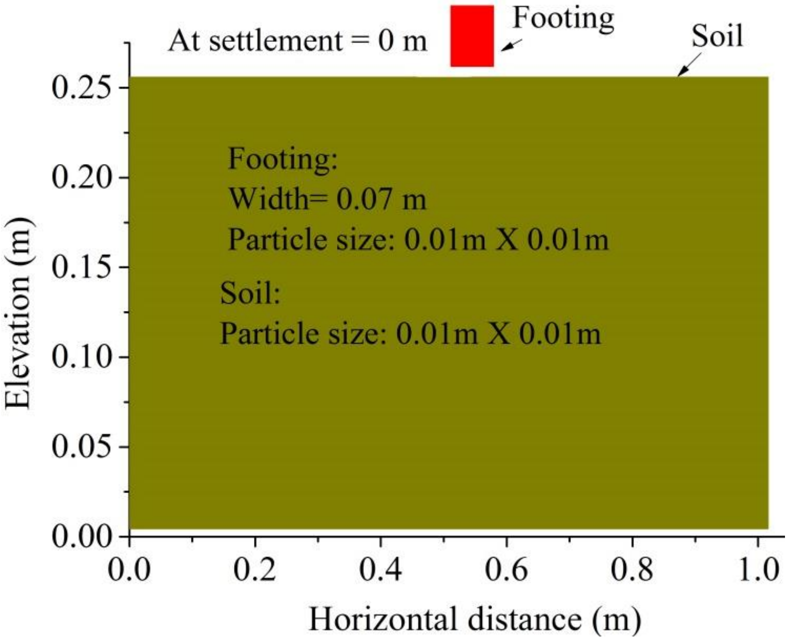

Figure 3.15 Bearing capacity test of cohesive soil by SPH.

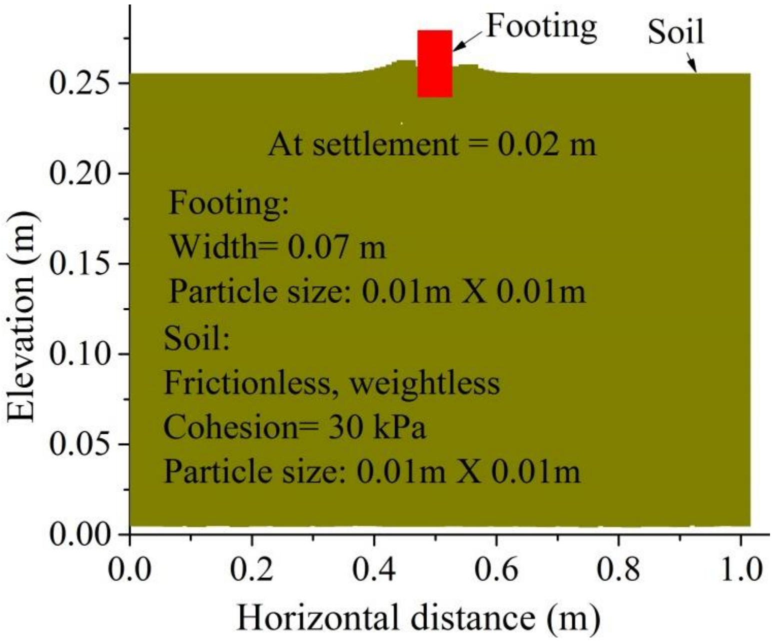

Figure 3.16 Progress of the bearing capacity test of cohesive soil by SPH at settlement of 0.02m.

Figure 3.17 shows the distribution of the maximum shear strains with progressive settlements of the footing for soil with c =30kPa. It was found that the failure surfaces were of circular shapes with a radius of approximately equal to the width of the footing. The failure surface developed by the SPH code was qualitatively correct.

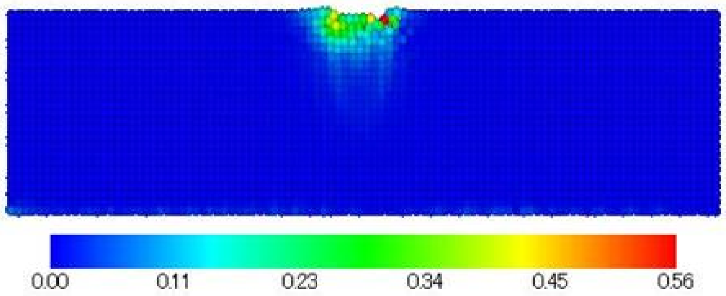

Max shear strain at settlement of 0.012 meter

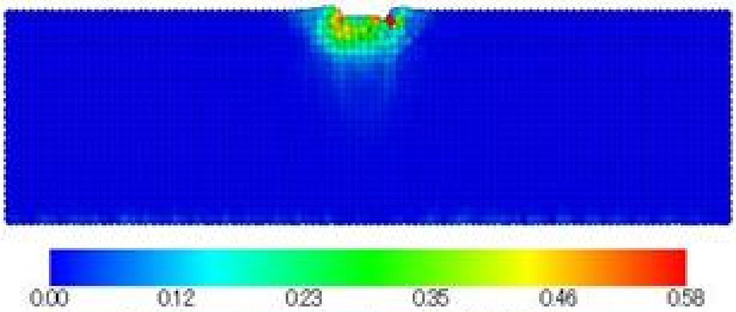

Max shear strain at settlement of 0.014 meter

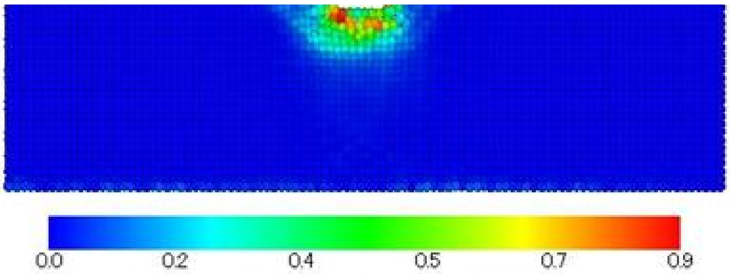

Max shear strain at settlement of 0.024 meter

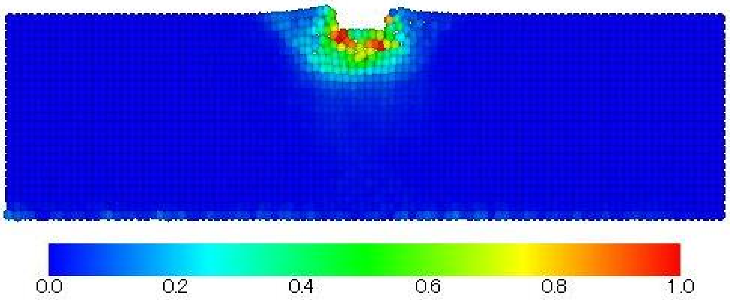

Max shear strain at settlement 0.026 meter

Figure 3.17 Maximum shear strain distribution for *c*= 30kPa at different settlement.

Figure 3.18 shows the relationships for settlement of footing and pressure below the footing for cohesive soils. Figure 3.18 shows comparison of SPH results with the analytical solution. It was found that ultimate bearing capacity generated by SPH simulations match satisfactorily with the analytical solutions. Figure3.20 shows the effect of SPH particle size on the bearing capacity test. It was found that bearing capacity with smaller particle size provided better result than that of coarser particle.

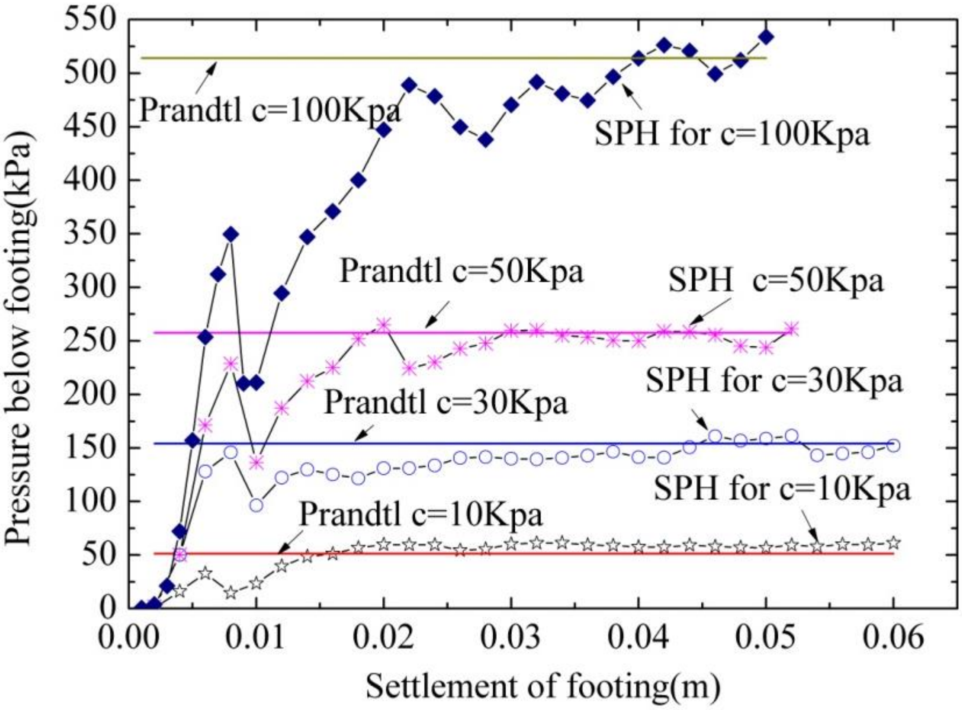

Figure 3.18 Bearing capacity test results for different cohesion values.

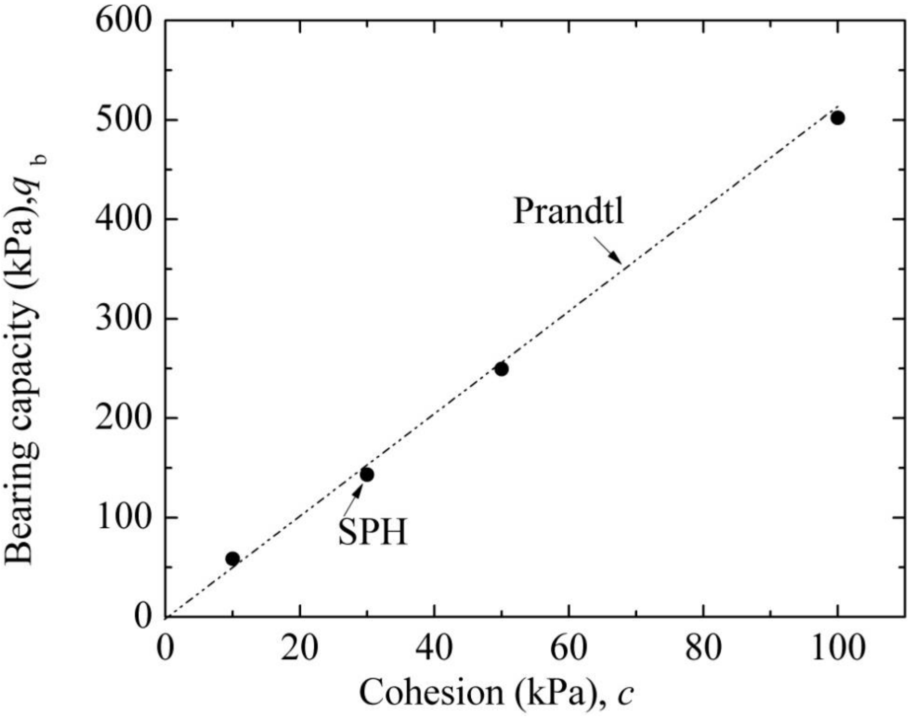

Figure 3.19 Comparison of bearing capacity for cohesive soil by SPH with Prandtl.

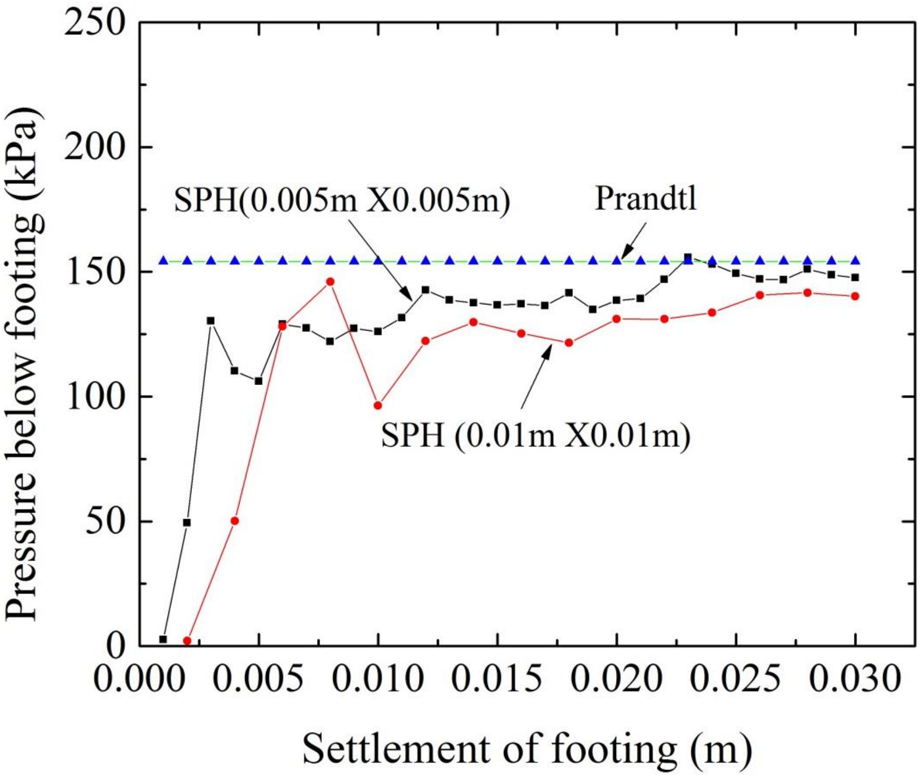

Figure 3.20 Comparison of bearing capacity for cohesive soil by SPH for different particle size.

Bearing capacity test for the frictional material was performed by the developed SPH code. Moreover, the ultimate bearing capacity for the soil was compared with the analytical solution. The analytical solution used for the frictional material was

$$q_b = 0.5\,\gamma_{soil}\,B_f\,N_\gamma \qquad (3.39)$$

Here, q_b is the ultimate bearing capacity (N/m^2) , B_f is the width of footing (m), N_γ is bearing capacity factors related with frictional angle of soil , taken from Meyerhof, Vesic and Hensen. The parameters used for the simulations are summarized in table 3.5.

Table 3.5 Parameters used for SPH simulation of frictional soil

Number of particles for soil, *N*	1400
Initial spacing (m), Δd	0.01
Gravity for frictional material (m/s^2), *g*	9.81
Duration for a times step (s), Δt	10^{-5}
Boundary type at the rigid base	Non-slip boundary
Boundary type at the vertical walls	Symmetric boundary
Density of soil (kg/m3), ρ	1800
Frictional angle for frictional soil (degree), ϕ	35
Settlement rate of footing (m/s)	0.01
Width of footing (m), B_f	0.07

Figure 3.21 shows the initial arrangement for the bearing capacity test. Figure 3.22 shows the progress of the bearing capacity test for frictional soil.

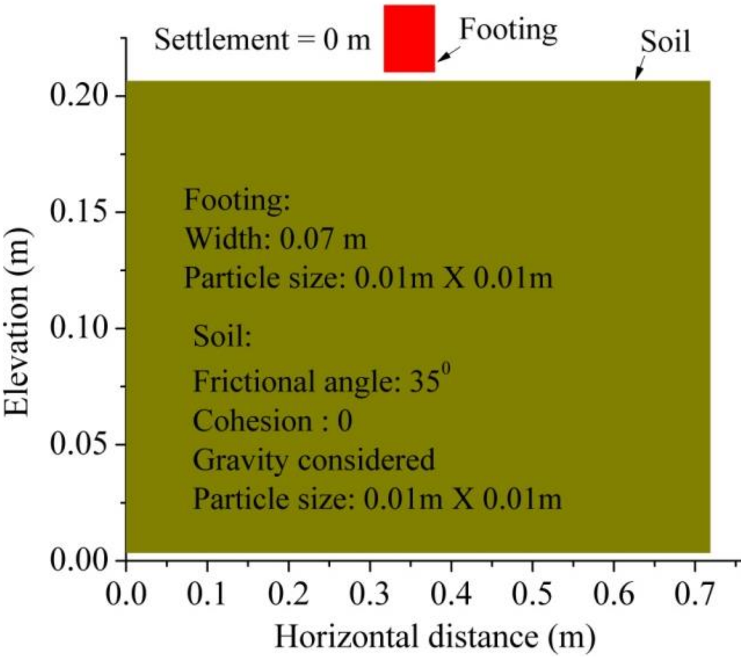

Figure 3.21 Initial set up for bearing capacity test of frictional soil.

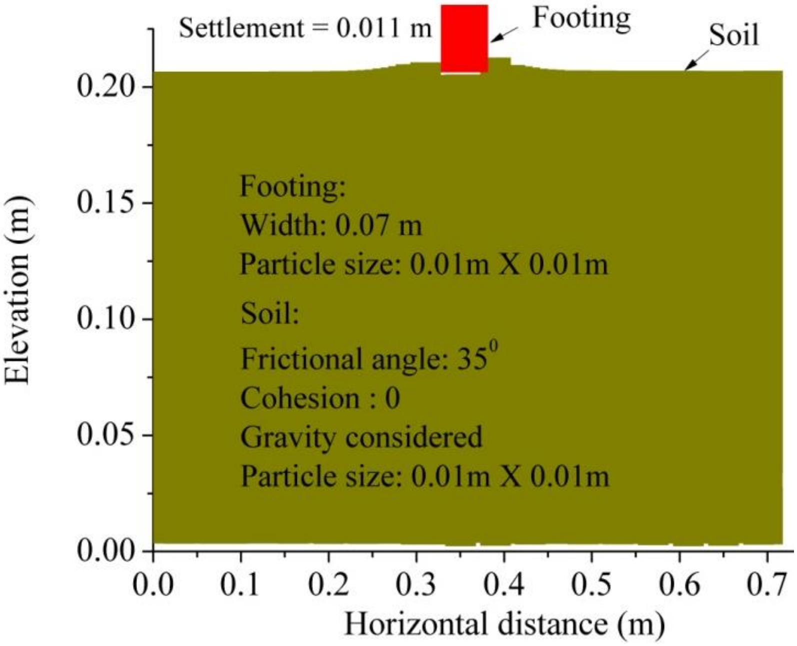

Figure 3.22 Progress of bearing capacity test of frictional soil.

Figure 3.23 shows the failure surface for the progressive settlement of the footing into the frictional materials.

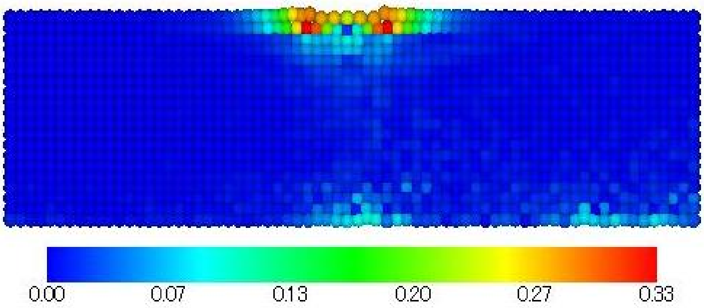

Max shear strain at settlement of 0.01 meter

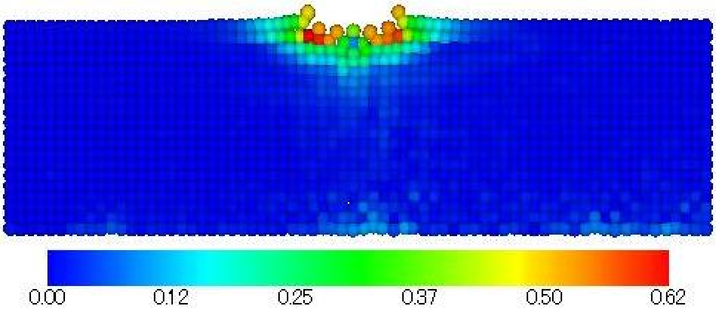

Max shear strain at settlement of 0.015 meter

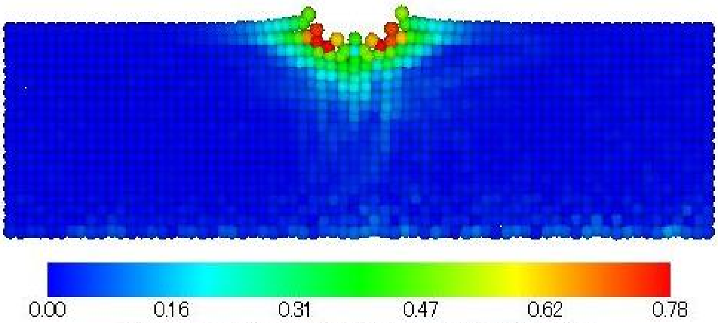

Max shear strain at settlement of 0.02 meter

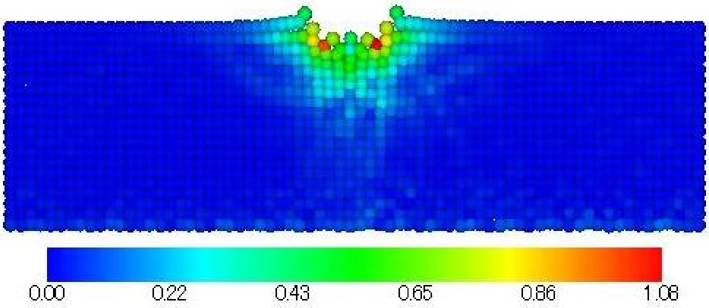

Max shear strain at settlement of 0.025 meter

Figure 3.23 Maximum shear strain distribution for $\phi = 35^0$ at different settlements.

Figure 3.24 shows the relationship between the pressure below footing and settlement. Figure 3.25 shows comparison of the ultimate bearing capacity results for frictional soils by the SPH code with that of the analytical solutions. It was found that ultimate bearing capacity predicted by the SPH code satisfactorily matches with analytical solution.

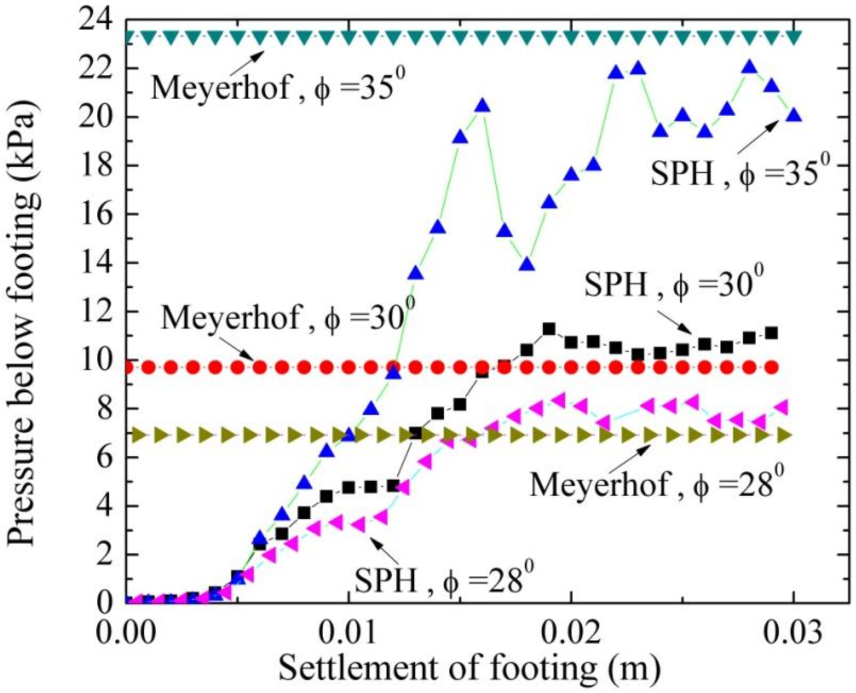

Figure 3.24 Bearing capacity test results for frictional soils.

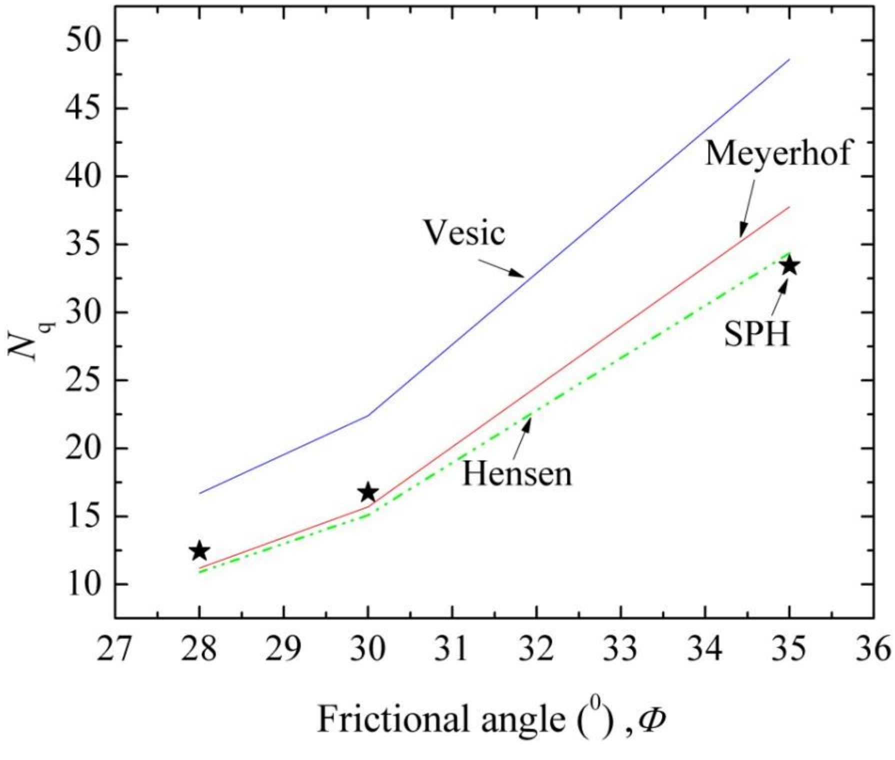

Figure 3.25 Bearing capacity test results for frictional soils.

3.6 Summary

This chapter has discussed about the formulations of D-P model in plane strain condition. SPH code was written based on the contents of this chapter. To verify the developed code simple shear test, granular flow test and bearing capacity test were performed. Simulation results were found okay when compared with the corresponding analytical or experimental results. So, developed SPH code is accurate enough to use for achieving the objective of the research.

CHAPTER 4

PERMEABILITY AND BOILING

4.1 Introduction

Chapter 4 describes the two phase SPH model to simulate deformation behavior of saturated soil. Permeability test and boiling test were performed to verify the code. Finally, the two phase model was applied to simulate the collapse of the mound under seepage condition and results are presented in this chapter.

4.2 Soil-water two phase model

In chapter 2 and chapter 3 SPH model for fluids and soils were described. However, those were only suitable for one phase flow. To simulate water and soil together it is necessary to use two-phase model. In the two phase soil-water model, soil and water will be governed by their own governing equations but additionally they will interact each other. To simulate interaction between water and soil, the study has considered the seepage force in two phase model. Water flowing through the pore space of the porous soil will exert seepage force to the soil structure and vice versa. The seepage force *f* will depend on the relative velocity, porosity and co efficient of permeability of the soil Maeda et al. (2004), Bui et al. (2007).

$$f = \gamma_{\mathrm{w}} n \frac{(v_{\mathrm{water}} - v_{\mathrm{soil})}}{k} \qquad 4.1$$

Where γ_{w} is the unit weight of water, *n* is the porosity and *k* is permeability coefficient of soil.

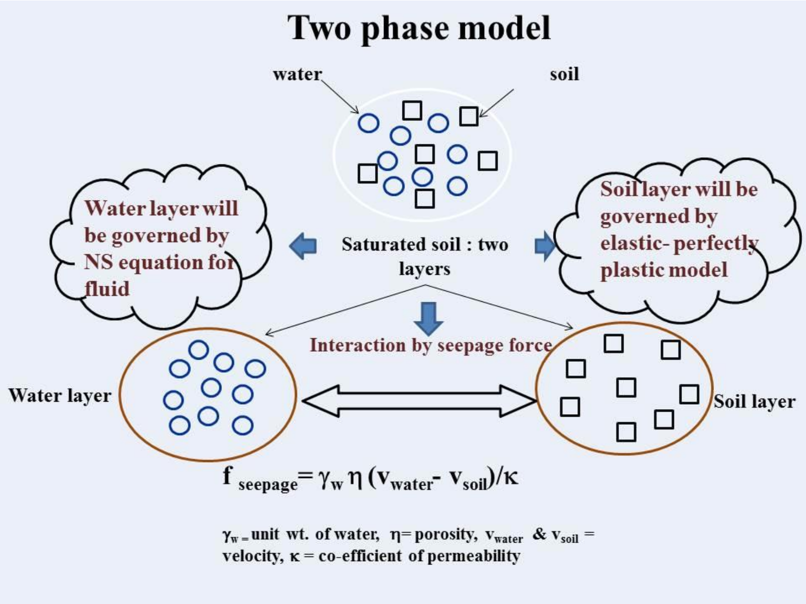

Figure 4.1 Description of two phase model.

In the two phase model the momentum equation for soil will be:

$$\frac{Dv_i^\alpha}{Dt} = \sum_{j=1}^{N} m_j \frac{\sigma_i' + \sigma_j'}{\rho_i \rho_j} \frac{\partial W_{ij}}{\partial x_i^\beta} - \prod_{ij} \delta^{\alpha\beta} + \sum_{j=1}^{N} m_j \frac{\gamma_{\mathrm{w}} n \frac{(v_{\mathrm{a}} - v_{\mathrm{i}})}{k}}{\rho_i \rho_a} W_{ia} + g_i^\alpha \qquad (4.2)$$

And the momentum equation for water will be

$$\frac{Dv_a^\alpha}{Dt} = - \sum_{b=1}^{N} m_b \frac{p_a + p_b}{\rho_a \rho_b} \frac{\partial W_{ab}}{\partial x_a^\beta} + \sum_{b=1}^{N} m_b \frac{\mu_a \varepsilon_a^{\alpha\beta} + \mu_b \varepsilon_b^{\alpha\beta}}{\rho_a \rho_b} \frac{\partial W_{ab}}{\partial x_a^\beta} - \prod_{ab} \delta^{\alpha\beta} - \sum_{b=1}^{N} m_b \frac{\gamma_{\mathrm{w}} n \frac{(v_{\mathrm{a}} - v_{\mathrm{i}})}{k}}{\rho_i \rho_a} W_{ia} + g_a^\alpha \quad (4.3)$$

Here, Π is the artificial viscosity term and δ is Dirac delta function, *g* is the body force in this case only gravitational force .

4.3 Verification of the two phase model

4.3.1 Falling head permeability test

To verify the two phase model, the study has performed a falling head permeability test. The head difference *h* at progressive time intervals were recorded and was divided by length of soil sample *L* to get the hydraulic gradient *i*, *i=h/L*. Local velocity at the middle section of the soil sample was measured and multiplied by the porosity *n* of the soil to get the average velocity *v*, *v* =v_{local} X *n*. The definitions of the terms are shown in figure 4.2. By using Darcy's law, *k*= *v/i,* was determined. The values of *k* from the simulations were compared with that of input values. Table 4.1 summarizes the parameters for the simulation.

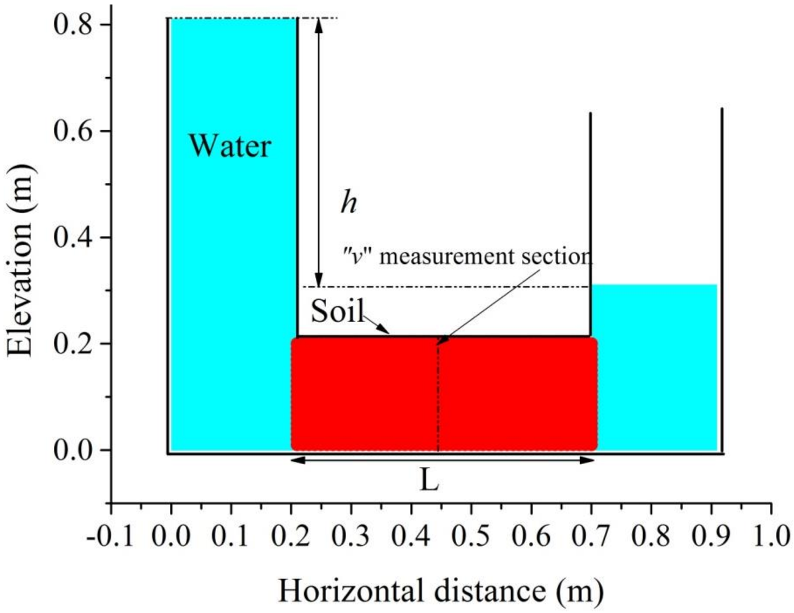

Figure 4.2 Description of permeability test.

Table 4.1 Summary of the parameters for the permeability test.

Number of soil particles	1000
Number of water particles	3200
Initial particle spacing (m), Δd	0.01
Smoothing length (m)	0.012
Duration of a time step (s), Δt	5×10^{-5}
Density for soils (kg/m^3)	2008
Density for water (kg/m^3)	1000
Theoretical coefficient of permeability (cm/s), k	0.10, 0.50, 1.0
Porosity, n	0.40
Length of soil (cm), L	50
Initial water level difference (cm), h	50
Artificial viscosity parameter for water α,β	0.01, 0.01
Average velocity coefficient for water, ε	0.001
Boundary type at rigid base	Non-slip
Boundary type at vertical wall	symmetric

Figure 4.3 shows relationship between the hydraulic gradient and average velocities obtained from the simulation. All the lines pass through the origin indicating that if h=0 there will be no velocity.

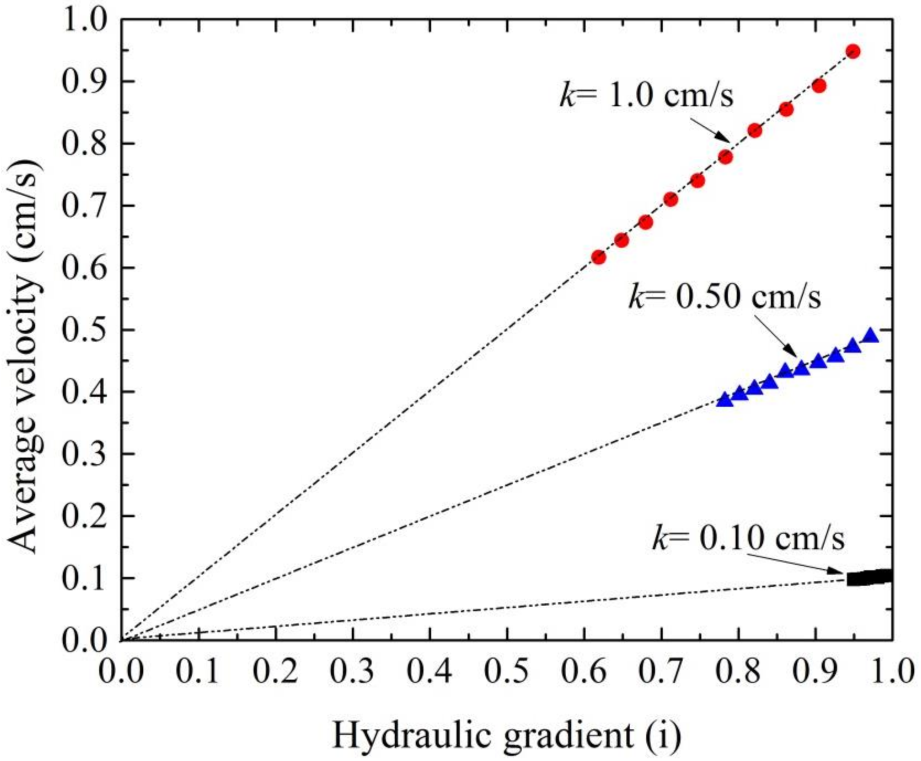

Figure 4.3 Hydraulic gradient and average velocity relationships from simulations.

Figure 4.4 shows the *k* values obtained from simulation dividing the average velocity by hydraulic gradient. *k* values were determined for progresssive time and found stable during the entire simulation.

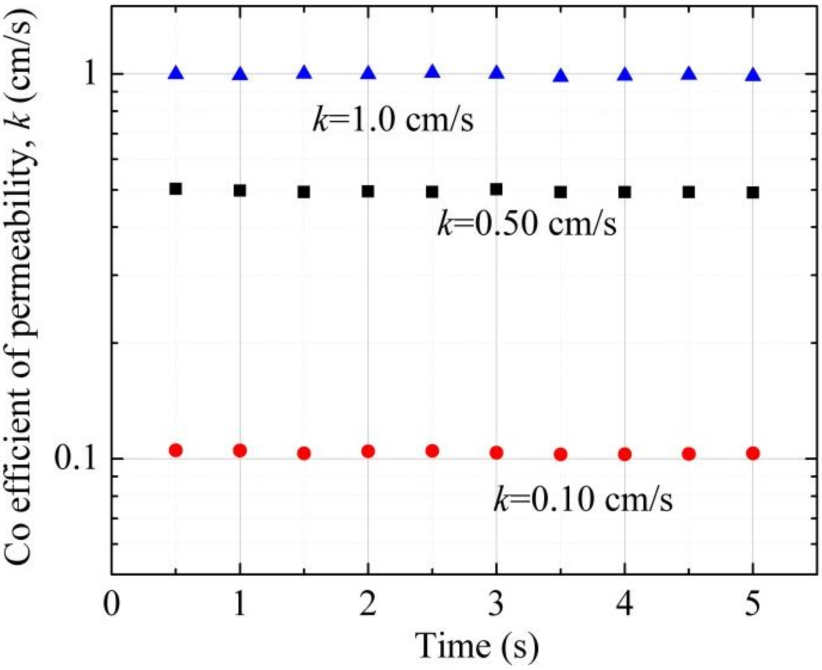

Figure 4.4 *k* values from simulations at different time.

Average *k* values for the total time for each case found in figure 5.4 were compared with the theoretical values in figure 4.5. The *k* values from the simulation match nicely with theoretical values.

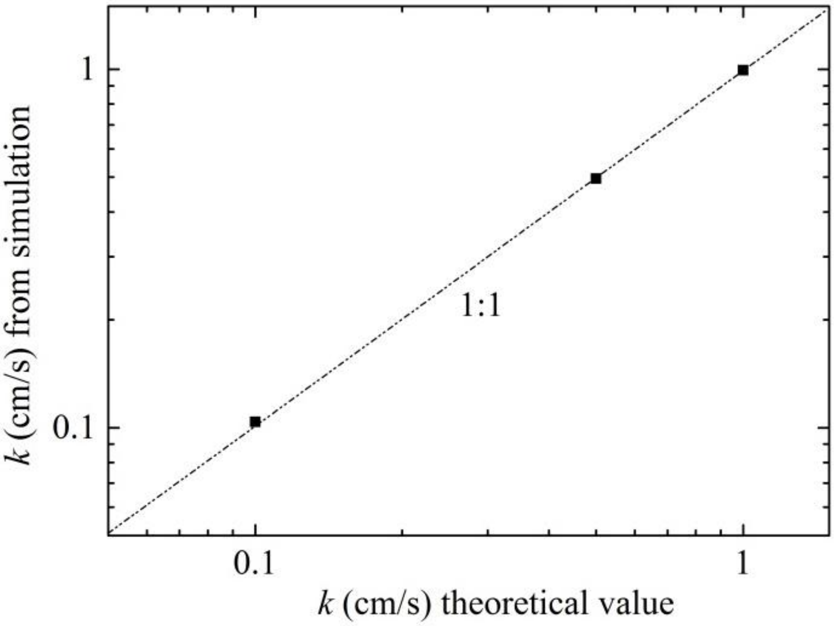

Figure 4.5 comparison of *k* values from simulation with theoretical.

4.3.2 Seepage flow and boiling

Seepage flow simulation was performed to check the ability of the developed SPH code for reproducing of boiling phenomenon. Figure 4.6 shows the model arrangement and table 4.2 summarizes the parameters for the simulation.

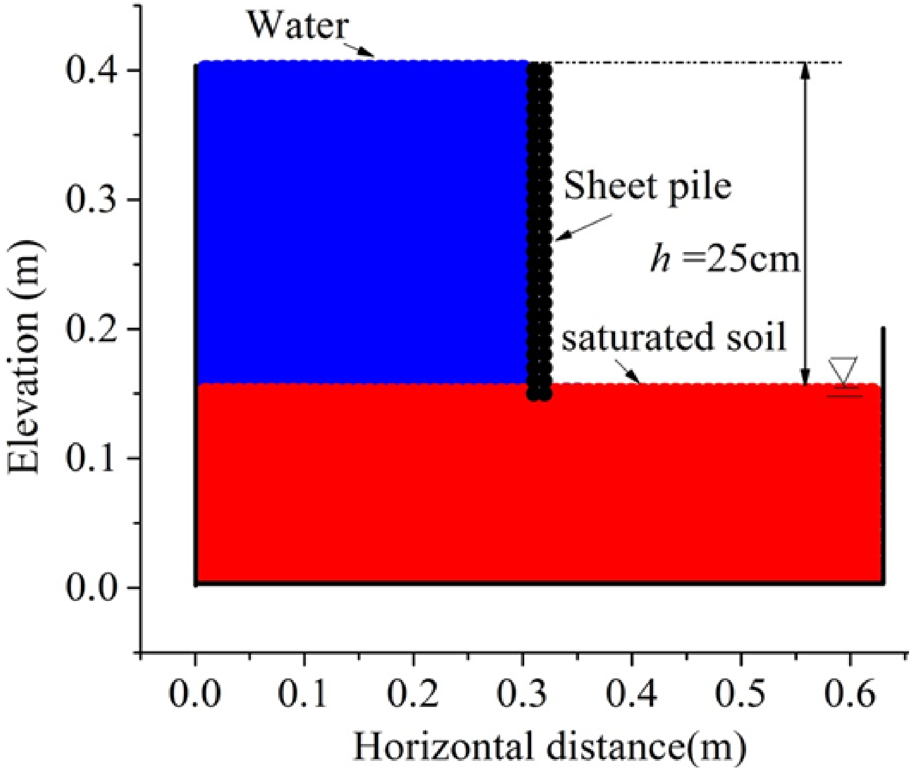

Figure 4.6 Arrangement of seepage and boiling test.

Table 4.2 Parameters for seepage flow and boiling test.

Number of soil particles	928
Number of water particles (initial)	1678
Initial particle spacing (m), Δd	0.01
Smoothing length (m)	0.012
Duration of a time step(s), Δt	2x 10^{-5}
Density for soils (kg/m^3)	2008
Density for water (kg/m^3)	1000
Theoretical coefficient of permeability(cm/s), k	0.10
Porosity , n	0.50
Head difference (constant) (cm), h	25
Embedded depth of sheet pile (cm)	3
Thickness for sheet pile (cm)	2
Artificial viscosity parameter for soil α, β	0.1, 0.1
Artificial viscosity parameter for water α, β	0.001, 0.
Average velocity coefficient for water, ε	0.30
Average velocity coefficient for water, ε	0.30
Boundary type at rigid base	Non-slip
Boundary type at vertical wall	symmetric

Figure 4.7 shows the generation heave in the soil due to seepage force. Figure 4.9 shows the maximum shear strain distribution and also shows clearly the generation of the heave. Figure 4.8 shows the velocity vector of water particles in the simulation.

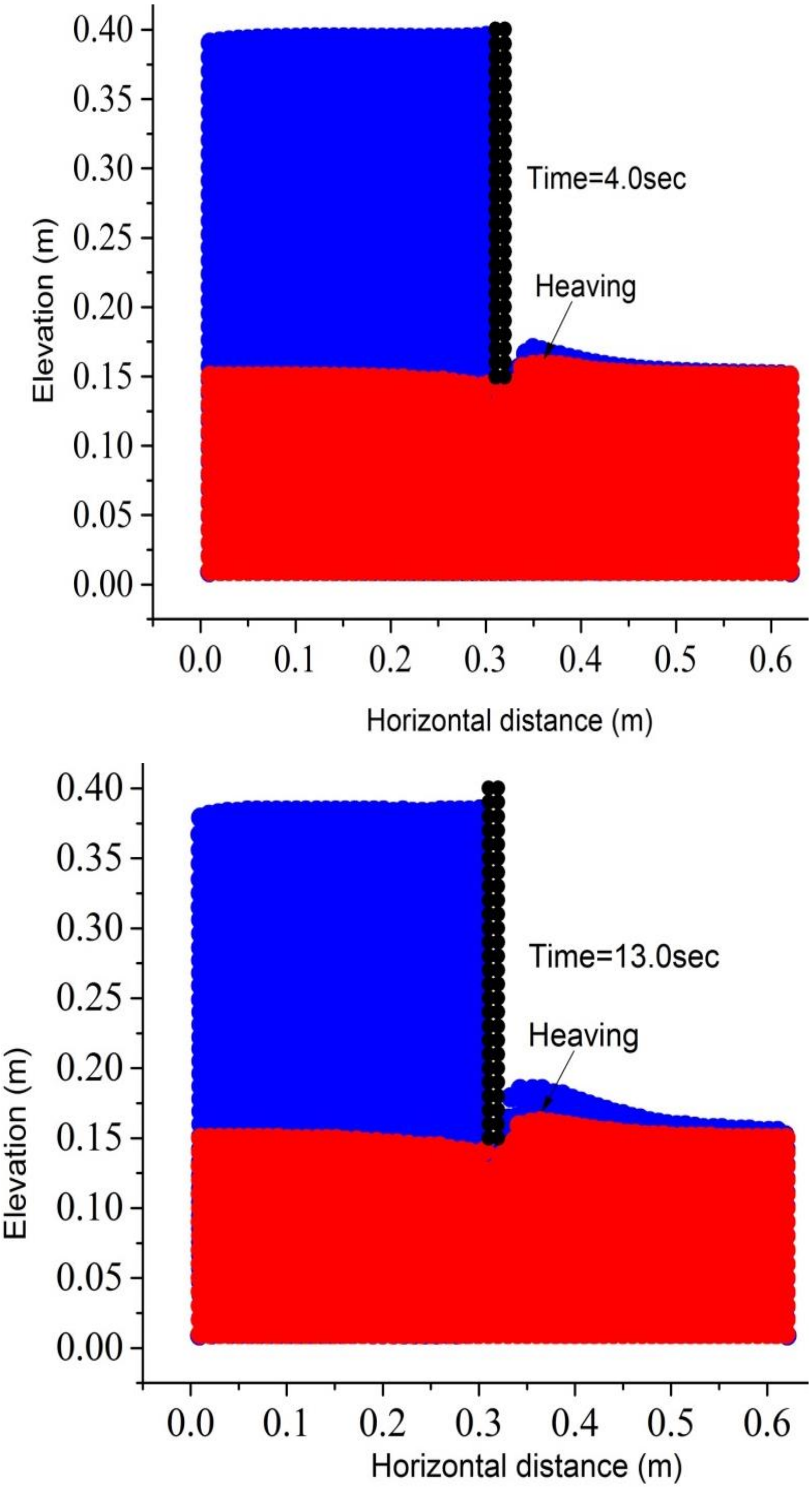

Figure 4.7 Generation of heaving.

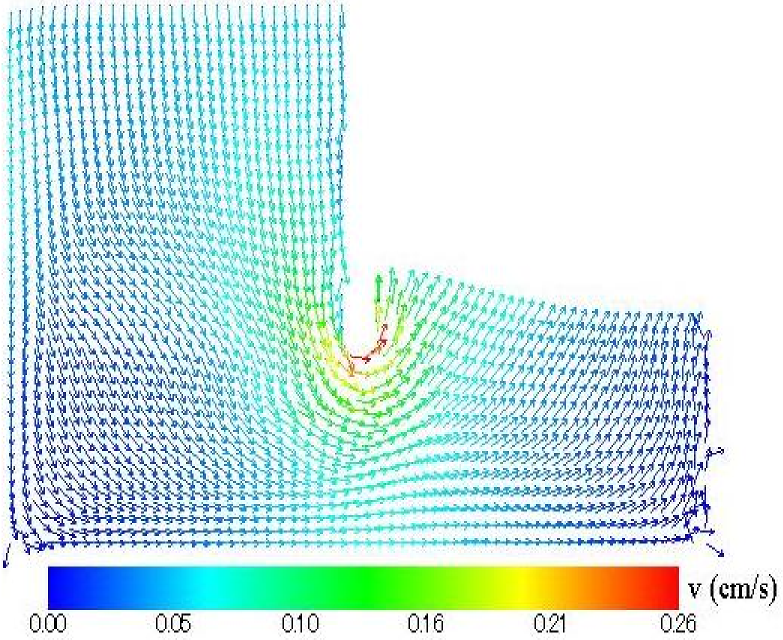

Figure 4.8 Velocity vector of water at 13 seconds.

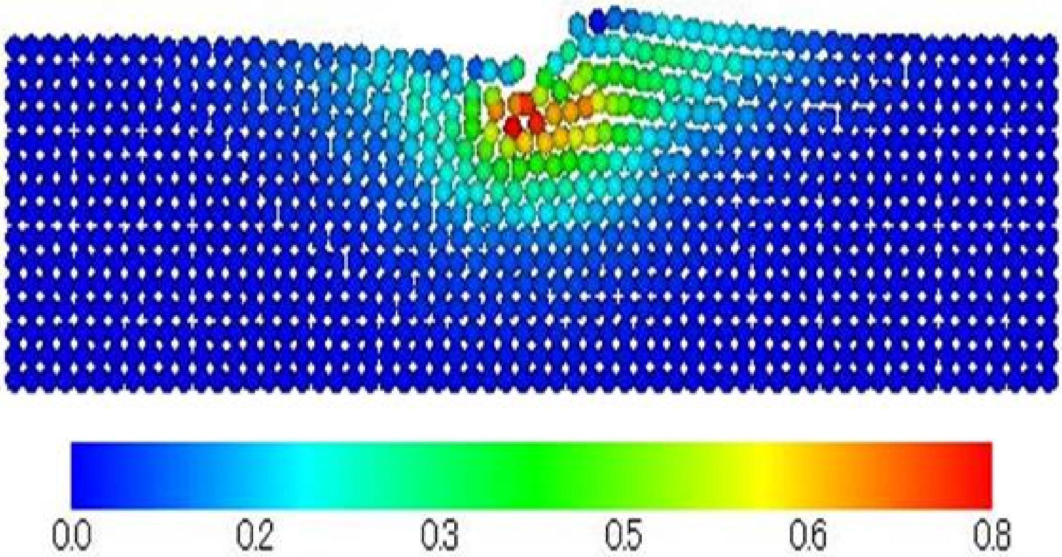

Figure 4.9 Maximum shear strain distribution at time 13 seconds.

4.4 Boiling during tsunami

4.4. 1 Model test for boiling during tsunami

A physical model of a breakwater and a mound was prepared in a soil box with a scale of 1/200 of prototype size. The soil box contains all the experimental arrangement as shown in figure 4.10. Breakwater mounds were prepared with silica sand # 2 (D_{50} = 3.2mm, Uc = 0.9) with the target relative density Dr = 70%. A caisson of breakwater made with cement mortar 12.5 cm in height, 10 cm in width and 11.5 cm in length was used in each test. Here, a Mariotte's tube tank and a pipeline were used to keep the sea-side water level stable.

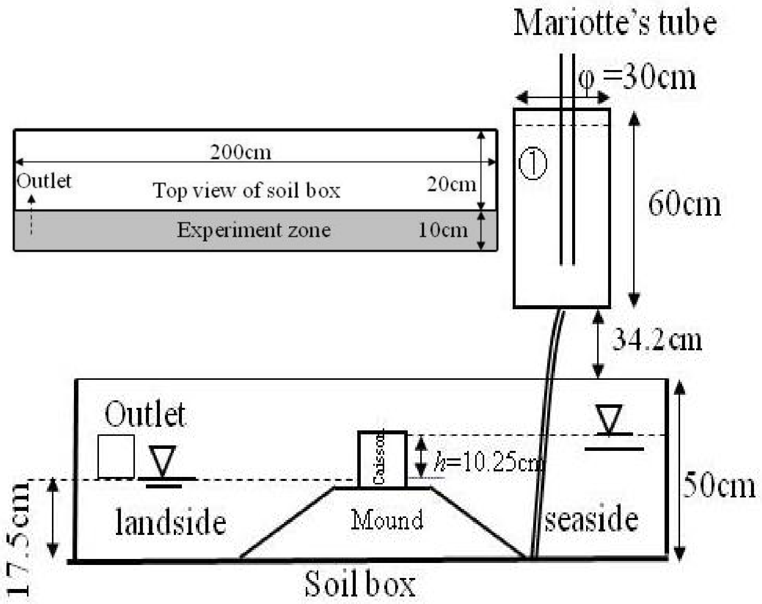

Figure 4.10 Arrangement of the experiment for seepage and boiling.

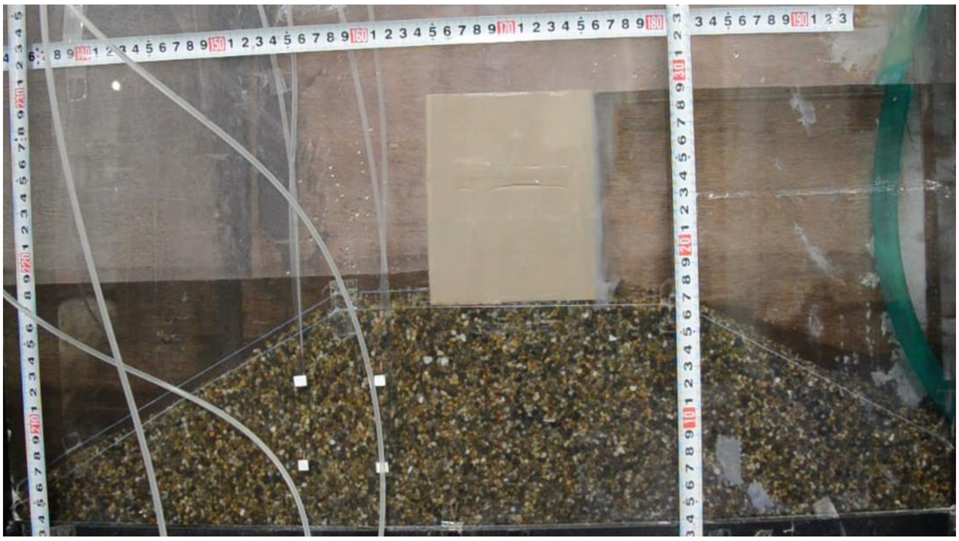

Photo 1 Experimental condition.

Initially water level at seaside and landside was kept same. Gradually seaside water level was increased and when the head difference *h* was about 10.25 cm air bubble was found at the downstream edge of caisson. Head difference with 10.25 cm was kept for sometimes. At first, some soil particles near the downstream edge of the caisson were displaced from its position. Afterwards a heave was formed. Some more soil particles from the downstream edge were found eroding. When soil particles from the downstream edge were eroding, flow of water through the pore spaces was increasing. Finally, a violent flow caused total wash out of soil particles below the caisson. The occurrence of boiling is shown by photo 4.2.

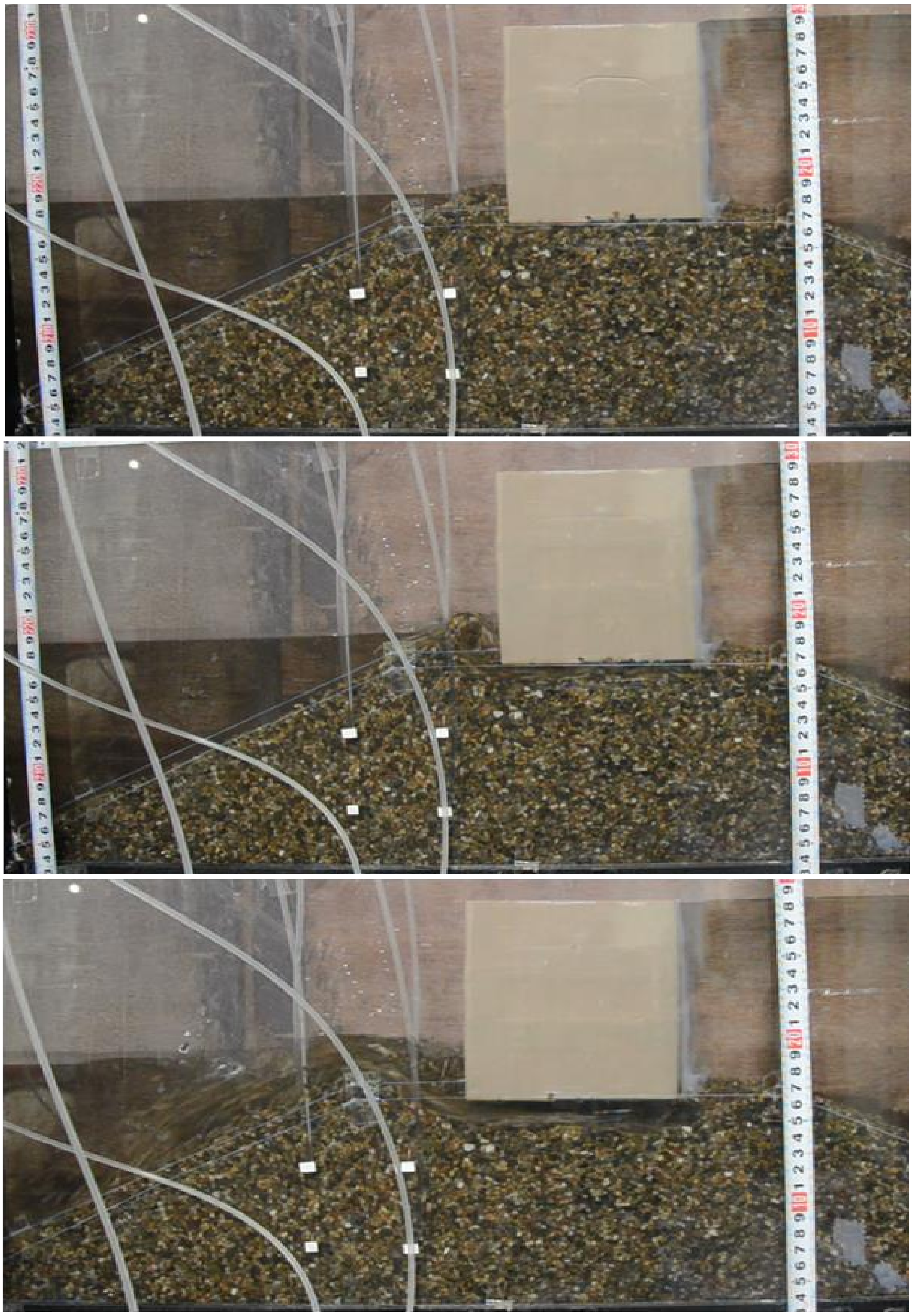

Photo 4.2 Gradual formation of heave and boiling. (top : heave formation, middle: stronger water flow, bottom: boiling)

4. 4.2 Simulation of boiling during tsunami

To simulate the experimental demonstration of the boiling during tsunami a simulation with developed SPH code was performed. Material properties for the simulation were kept same as the experiment. However, for reducing the simulation time, unaffected region of the mound observed during the experiment was excluded in simulation. Table 4.3 and figure 4.11 summarize the parameters for the simulation.

Table 4.3 Parameters for simulation of boiling during tsunami.

Number of soil particles	1496
Number of water particles (initial)	1836
Initial particle spacing (m), Δd	0.01
Smoothing length (m)	0.012
Duration of a time step (s), Δt	$2\text{x } 10^{-5}$
Density for soils (kg/m^3)	2008
Density for water (kg/m^3)	1000
Frictional angle for soil (degree), ϕ (c=0)	35
Theoretical coefficient of permeability(cm/s), k	0.10
Porosity, n	0.50
Head difference (constant) (cm), h	15 (13.2)
Thickness of caisson (cm)	11.5
Artificial viscosity parameter for soil α, β	0.1, 0.1
Artificial viscosity parameter for water α, β	0.001, 0.
Average velocity coefficient for water, ε	0.30
Average velocity coefficient for water, ε	0.30
Boundary type at rigid base	Non-slip
Boundary type at vertical wall	symmetric

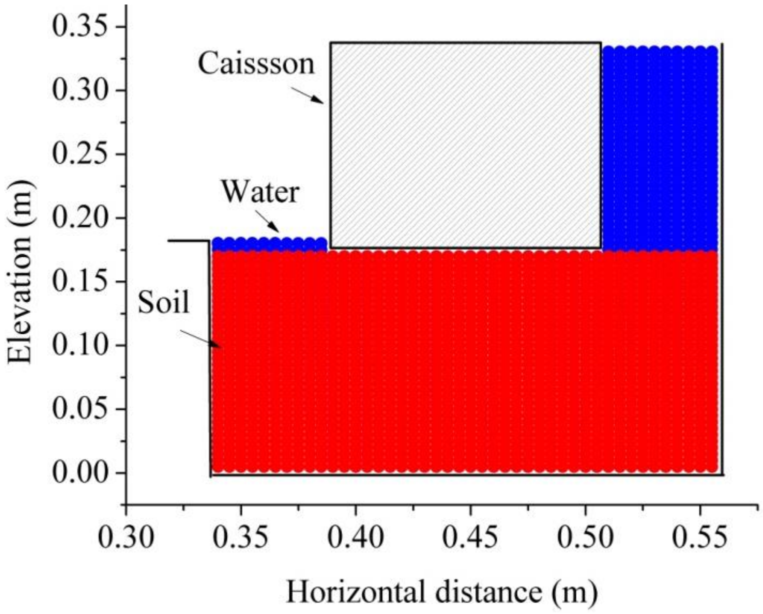

Figure 4.11 Arrangement for boiling simulation during tsunami.

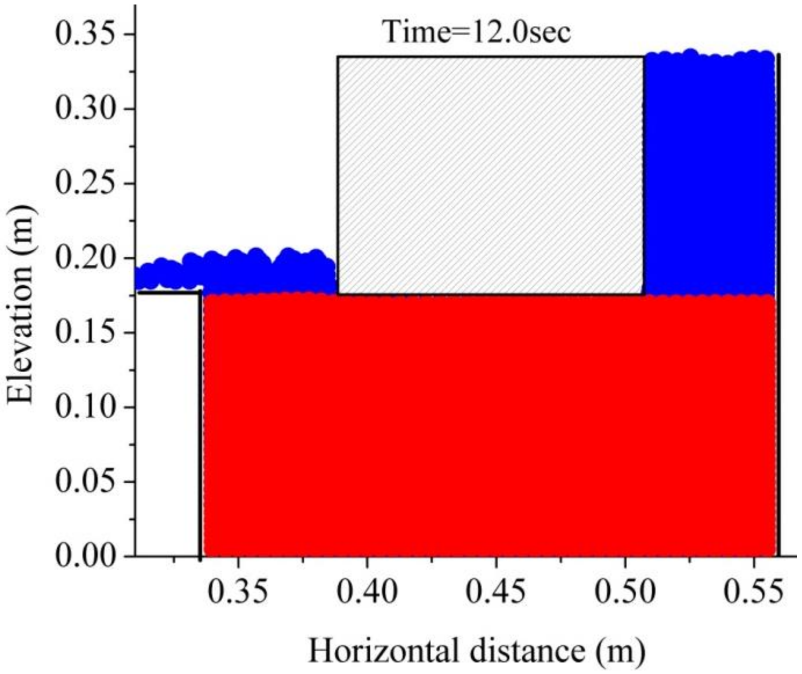

Figure 4.12 Boiling during tsunami at 12 seconds seepage flow.

Figure 4.12 shows the effect of 12 seconds seepage flow with keeping the head difference approximately 15 cm (13.2cm). Due to scale effect and small amount of heave generation it is very difficult to visualize the boiling phenomenon. However, figure 4.14 shows clearly the formation of heave due to the seepage flow. Figure 4.13 show the velocity vector at 12 seconds of seepage flow.

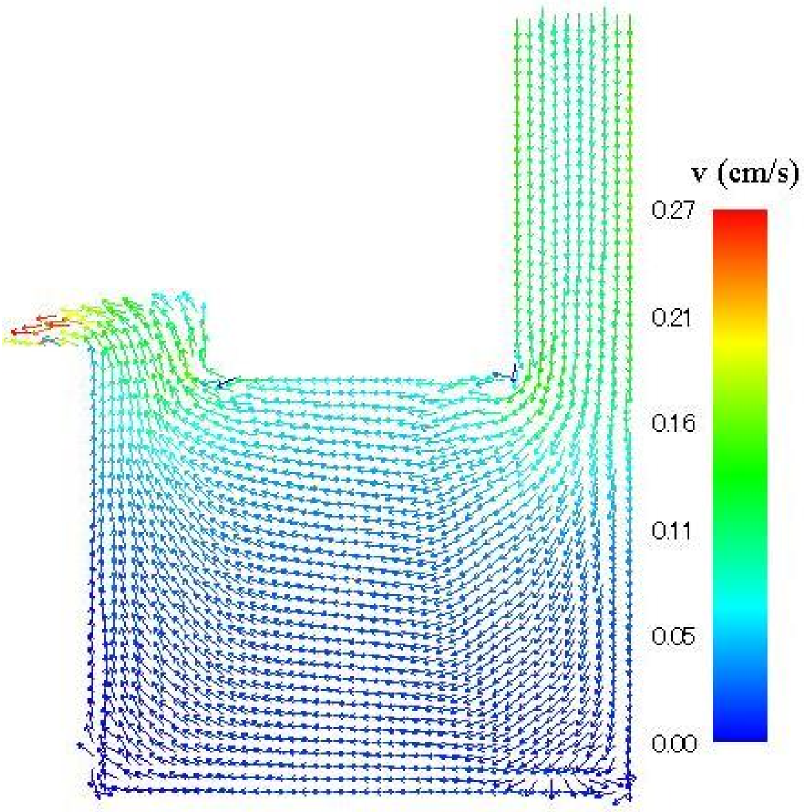

Figure 4.13 Velocity vector at 12 seconds seepage flow.

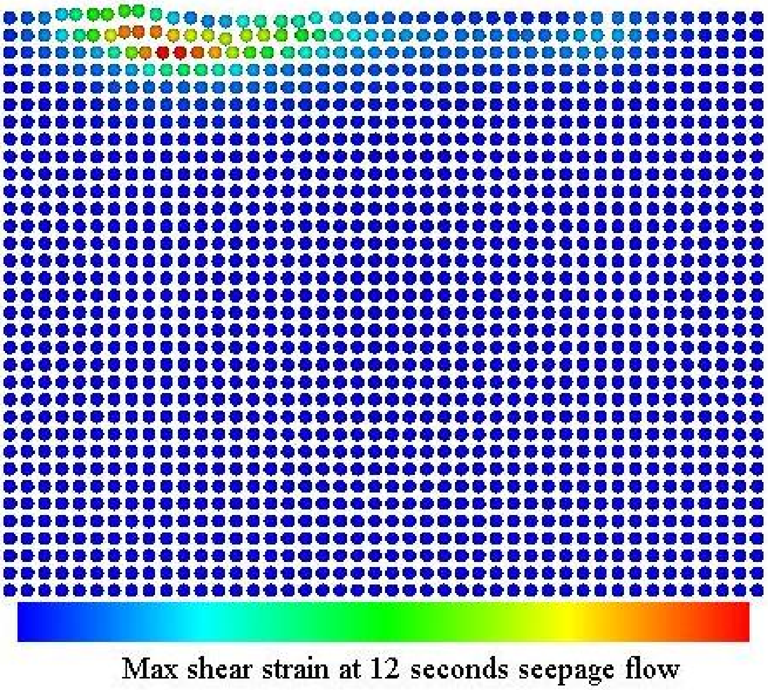

Figure 4.14 Maximum shear strain at 12 seconds seepage flow.

4.5 Summary

This chapter has described the formulations of two phase model. Based on the formulations in this chapter SPH code was written. Verification of the code was performed firstly by comparing the results of constant head permeability test with analytical values. Results had shown excellent matching with the analytical values. Ability of reproducing the boiling phenomenon was also checked. It was observed that SPH could simulate the generation of heave nicely.

CHAPTER 5

EXPERIMENTAL INVESTIGATION FOR SCOUR MECHANISMS IN A BREAKWATER MOUND

5.1 Introduction

Several countermeasures have been suggested to increase ductility of breakwater mounds against scouring induced by tsunami. However, the scour mechanisms can be sometimes complicated as pointed out by Imase et al. (2012). For example, the effect of overflow on the collapse of breakwater mounds has been demonstrated by Arikawa et al. (2012). So far it has not been well clarified how these mechanisms on scours can be changed by countermeasures. Therefore, simple models of a breakwater mound with and without countermeasures under seepage flow and overflow conditions were prepared in this study. Then the changes of the scour mechanisms were investigated.

5.2 Model test conditions and methods

A physical model of a breakwater and a mound was prepared in a soil box with a scale of 1/200 of prototype size as shown in figure 5.1. Moreover, two mound models with countermeasures were prepared. The soil box contains all the experimental arrangement as shown in figure 5.1. The experimental conditions are described in table 5.1. For all the cases, breakwater mounds were prepared with silica sand # 2 (D_{50} = 3.2mm, U_c = 0.9) with the target relative density D_r = 70%. Four pore water pressure gauges (PP gauges) were installed in the mounds as shown in the figure 5.1. A caisson of breakwater made with cement mortar 12.5 cm in height, 10 cm in width and 11.5 cm in length was used in each test. Tsunami overflow was produced for approximately 80 seconds with using a Mariotte's tube tank and a wooden channel. Here, the tank was used to keep the flow rate constant during the overflow. Moreover, another Mariotte's tube tank and a pipeline were used to keep the sea-side water level stable.

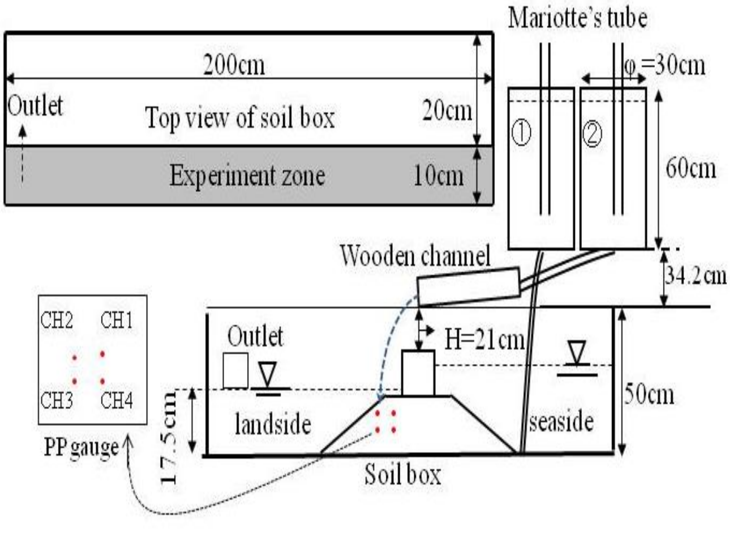

Figure 5.1 Model test arrangement.

The flow rate q was set to be 8.5×10^{-3}(m^3/s/m), and the falling height z_f was set to be 34.5 cm. This combination of q and z_f made the whirlpool diameter R, 0.04 m in each test. During overflow, the sea level at the landside was set to be 17.5 cm in all tests.

Table 5.1 Experimental conditions.

Identification	h(cm)	Countermeasures	Description
Case A	0	None	Only overtopping
Case B_1	5.0	None	Overtopping + seepage
Case B_2	6	None	Overtopping + seepage
Case B_3	7	None	Overtopping + seepage
Case C	5.0	Widening and raising of embankment	Overtopping + seepage
Case D	5.0	Widening and raising of embankment + sheet pile	Overtopping + seepage

In case A, the water head difference h between seaside and landside was set to be 0 cm as shown in figure 5.2. That meant that there was no seepage flow from the seaside during the overflow. On the other hand, in the cases B_1, B2 and B_3, h were set to be 5 cm, 6 cm and 7 cm during the overflow as shown in figure 5.3. Countermeasure experiments were conducted in case C and case D. In Case C, widening and raising of the mound was conducted with a thickness of 1.0cm at the landside as shown in figure 5.4. In case D, in addition to the widening and raising of the mound, a sheet pile made of a wooden panel was installed in the mound as shown in figure 5.5. The thickness of the wooden panel was 12 mm.

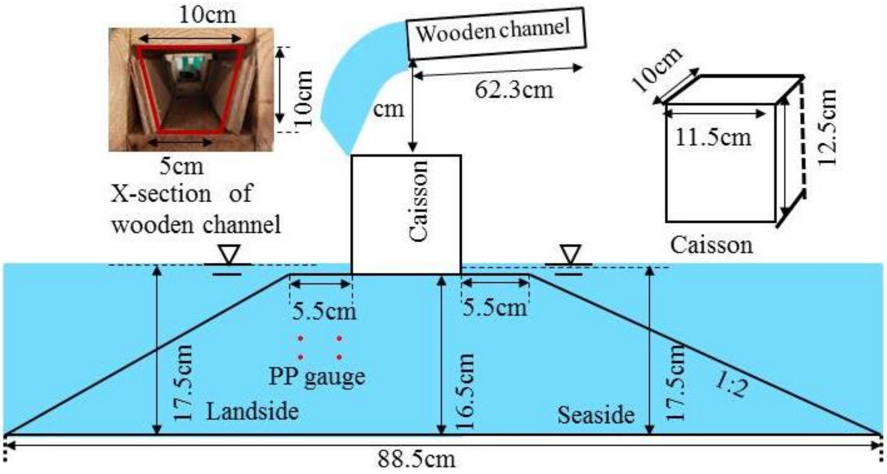

Figure 5.2 Arrangement for case A.

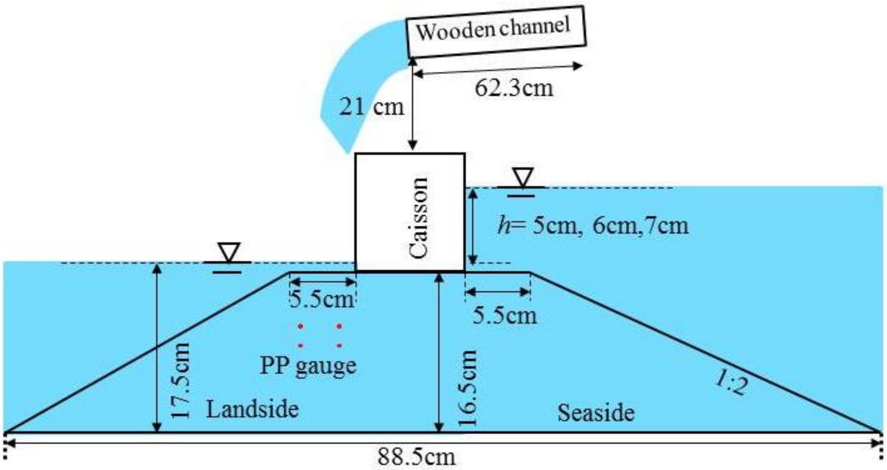

Figure 5.3 Arrangement for case B_1, B_2, B_3.

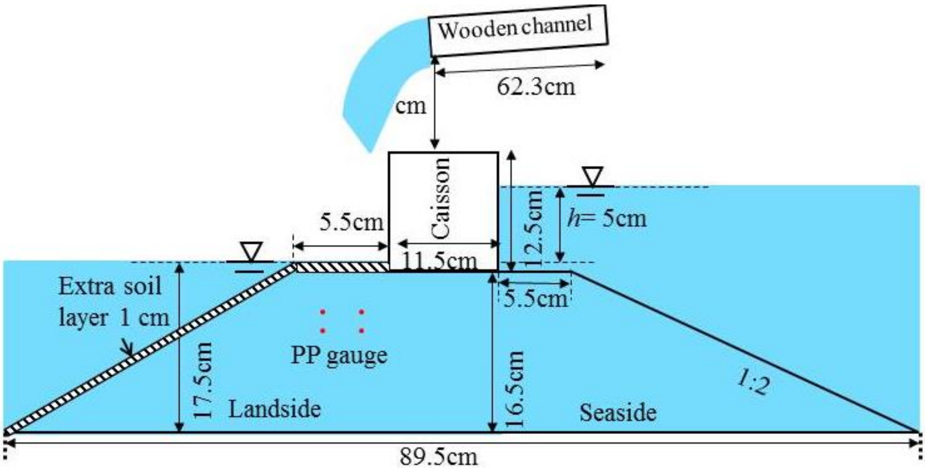

Figure 5.4 Arrangement for case C.

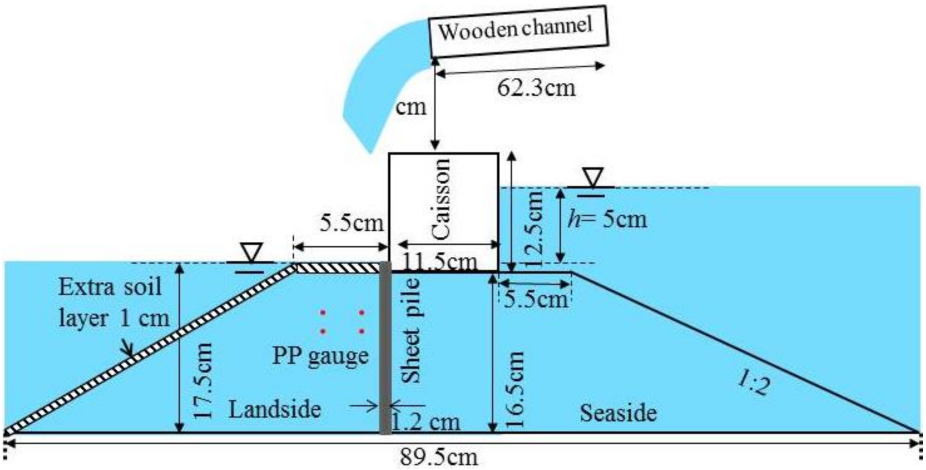

Figure 5.5 Arrangement for case D.

5.3 Model test results

5.3.1 Deformation and scour of breakwater mounds

Photo 5.1 and photo 5.2 show the scour progress for case A and B_1. Deformation and scour profiles for cases A and C can be realized from the figure 5.6. According to figure 5.6, elevation of landside top edges of the deformed profiles of case C with dotted lines were significantly higher than those of case A. As a result, transportation of the scoured soils was more difficult for case C resulting in resettlement of the scoured soils. However, the deformed profiles in case A with smoother shapes will easily allow transportations of scoured soils. Change of transportation characteristics due to introduction of counter measure might be one of the reasons for reducing the maximum scour depths for cases C and D observed in figure 5.5. Photo 5.3 shows the scour progress for case D. Here installation of the sheet pile stopped the soil collapse.

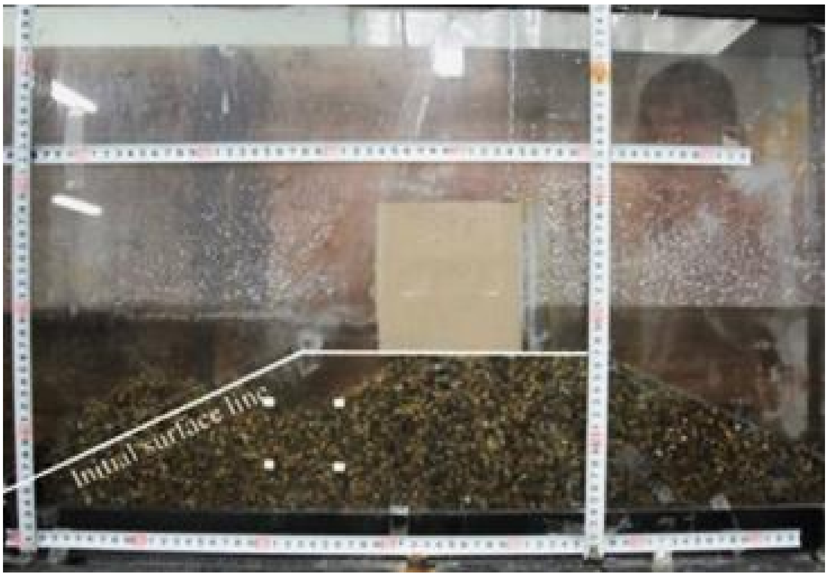

Photo 5.1 Progress of scouring for case A.

Photo 5.2 Scouring progress for case B_1.

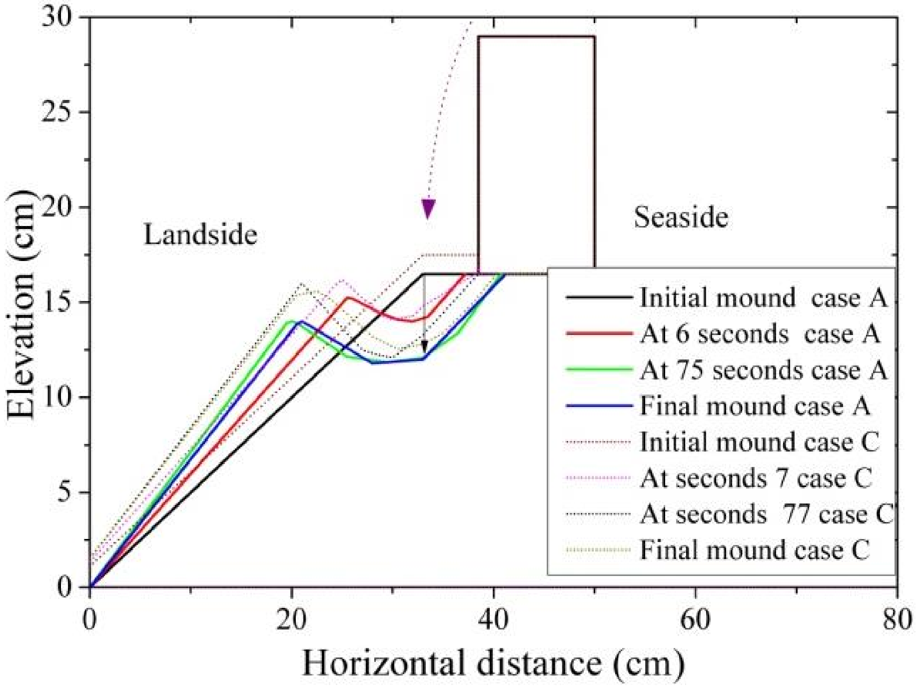

Figure 5.6 Change of longitudinal profile of the mound with time, observed in the cases A and C.

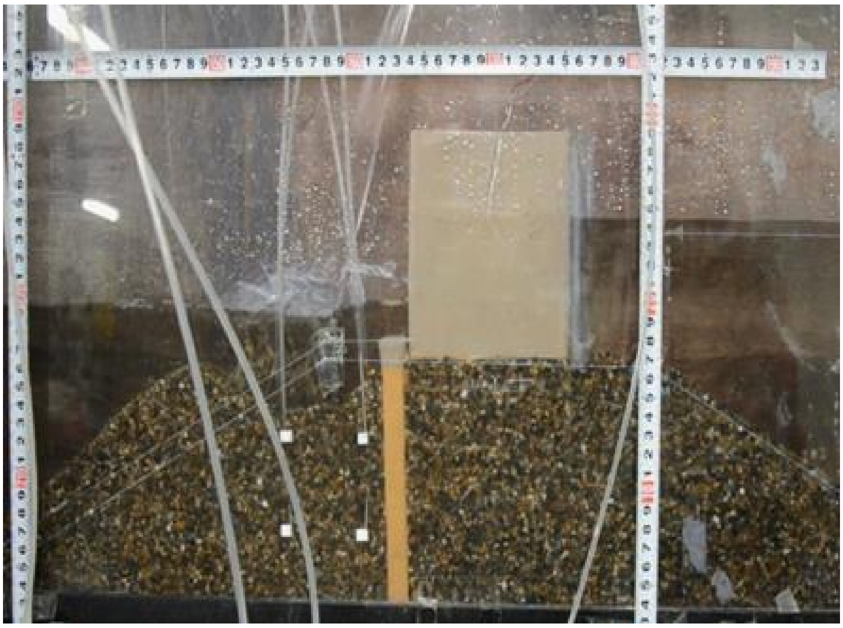

Photo 5.3 Scouring progress for Case D.

5.3.2 Maximum scour depth and scour width

Based on the time series of the longitudinal profiles of the mounds as shown in figure 5.6, change of maximum scour depth $SD_{\max}$ and that of scour width $SW_{\max}$ were evaluated. Here for all the cases, $SD_{\max}$ was defined vertically from the shoulder edge and $SW_{\max}$ was defined from the shoulder edge towards the caisson. It is to be noted that, shoulder level means excluding the counter soil layer used in countermeasures.

In figures 5.7 & 5.8, the scour depths and widths with progress of time for head differences of 0 cm, 5 cm, 6 cm and 7 cm were plotted. For head differences with 6 cm and 7 cm, the boiling phenomenon was so strong that caisson was found to be collapsed after some time. As a result, measurements data for cases B_2 & B_3 were not possible to record after the collapse. That is why in figures 5.7 & 5.8, data lines for cases B_2 & B_3 are smaller than that of other cases.

From figures 5.7 & 5.8, it was found that both scour depths and widths increased with the increase of head difference between seaside and landside of the mound. Increase in head difference meant, increase in seepage force. So, seepage force was found to increase both the scour depth and width.

As seen in the figure 5.9, $SD_{\max}$ for case A were less than those of case B_1 by 0.6 cm. Case A and case B_1 were conducted under the same condition except that case B_1 has an additional effect of seepage.

$SD_{\max}$ for case C and case D were significantly lower than that of case B_1. The difference is more than 1.0 cm which was the thickness of the counter soil layer. Focusing on the results of the two countermeasures, 31 percent of $SW_{\max}$ of case C was reduced by installing the sheet pile in case D.

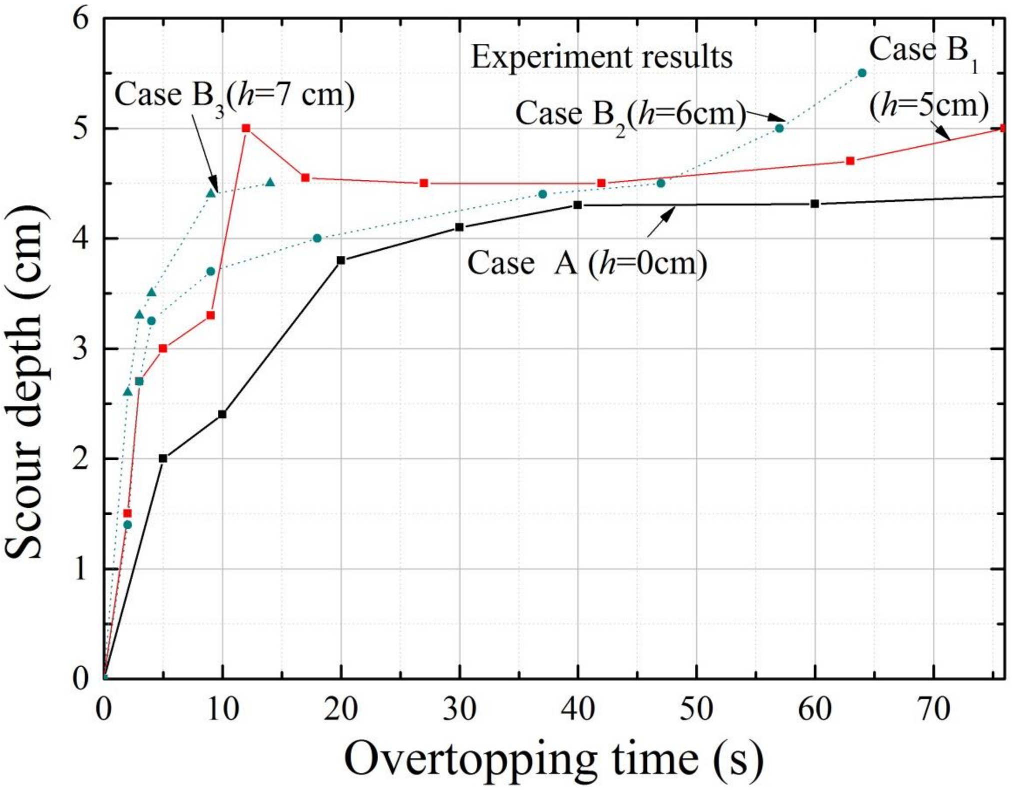

Figure 5.7 Scour depths with progress of time for various head differences.

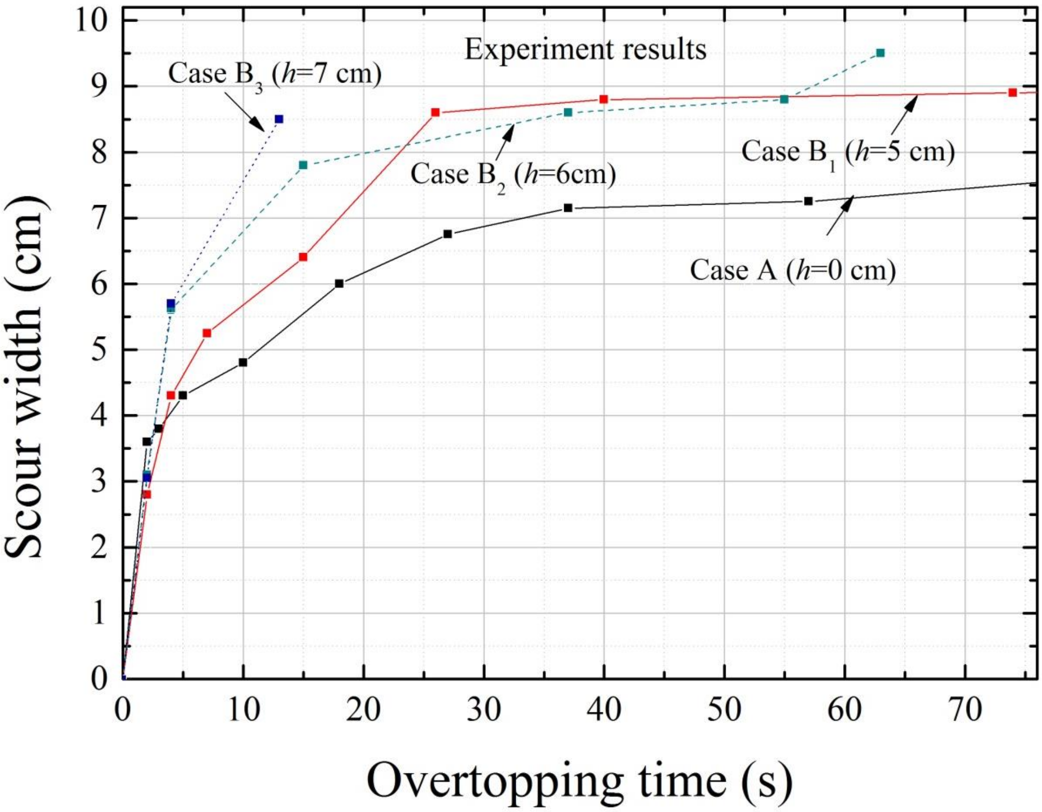

Figure 5.8 Scour widths with progress of time for various head differences.

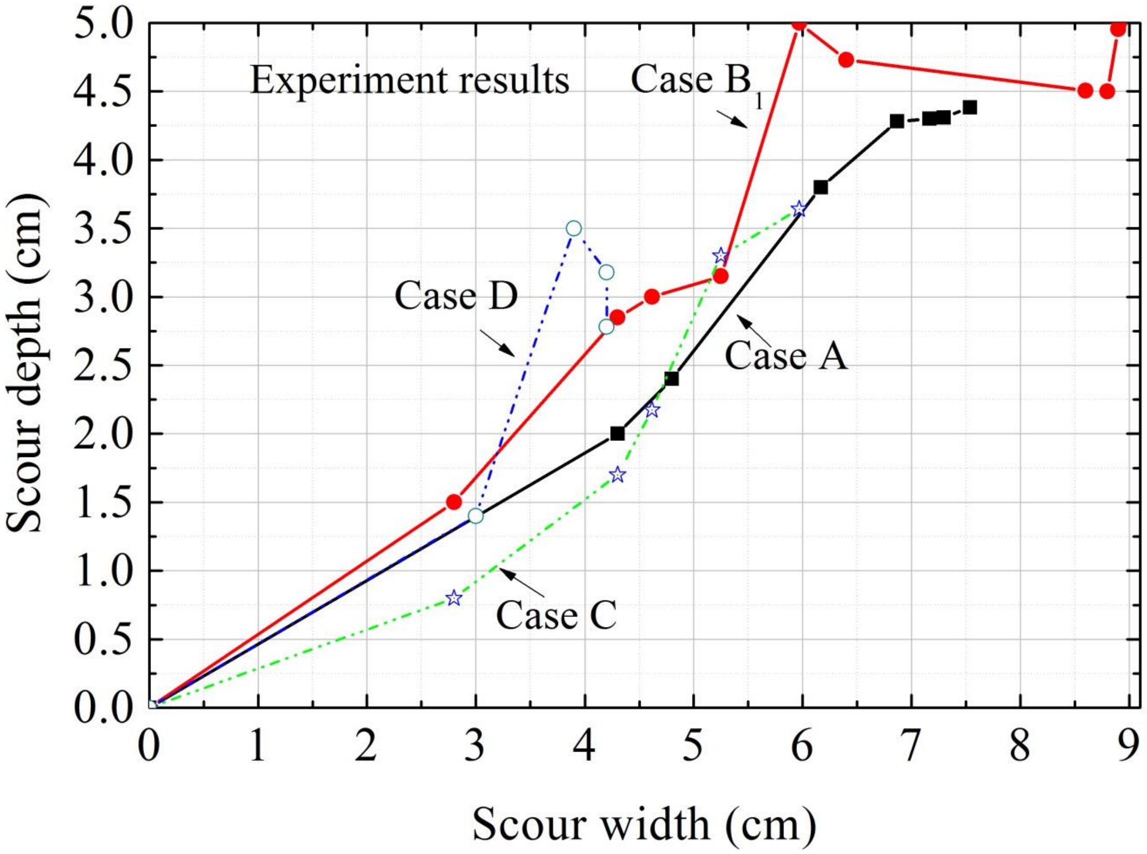

Figure 5.9 Relationships between scour widths and scour depths up to overtopping time of 76 seconds.

5.3.3 Hydraulic gradient

Figure 5.10 shows relationships between horizontal hydraulic gradients (i_x) and vertical hydraulic gradients (i_y) in the mound. For calculating i_x for CH1 - CH2 , difference of pore pressure was divided by the distance between them. Moreover, for calculating i_y for CH3 - CH2 , difference of pore pressure was divided by the distance between them. For sign convention, pore pressure gradients going down towards landside and down towards the surface were taken as positives for i_x and i_y respectively.

According to figure 5.10, case B_1 had the maximum $(i_y)_{max}$ of 0.42 and minimum $(i_y)_{min}$ of 0.05 . On the other hand, case A had the $(i_y)_{max}$ of 0.24 and $(i_y)_{min}$ of 0.03. The hydraulic gradients' differences between case A and case B_1 might be resulting in the difference of SD_{max} seen in figure 5.9. The $(i_y)_{max}$ of cases C and D was 0.33 and 0.30 respectively which were lower than that of case B_1. This also might contribute to the decrease of SD_{max} in cases C and D with respect to that in case B_1. The reason why the $(i_y)_{max}$ of case D was not lower than that of case A might be attributed to some leakage of seepage water between the sheet pile and the soil box.

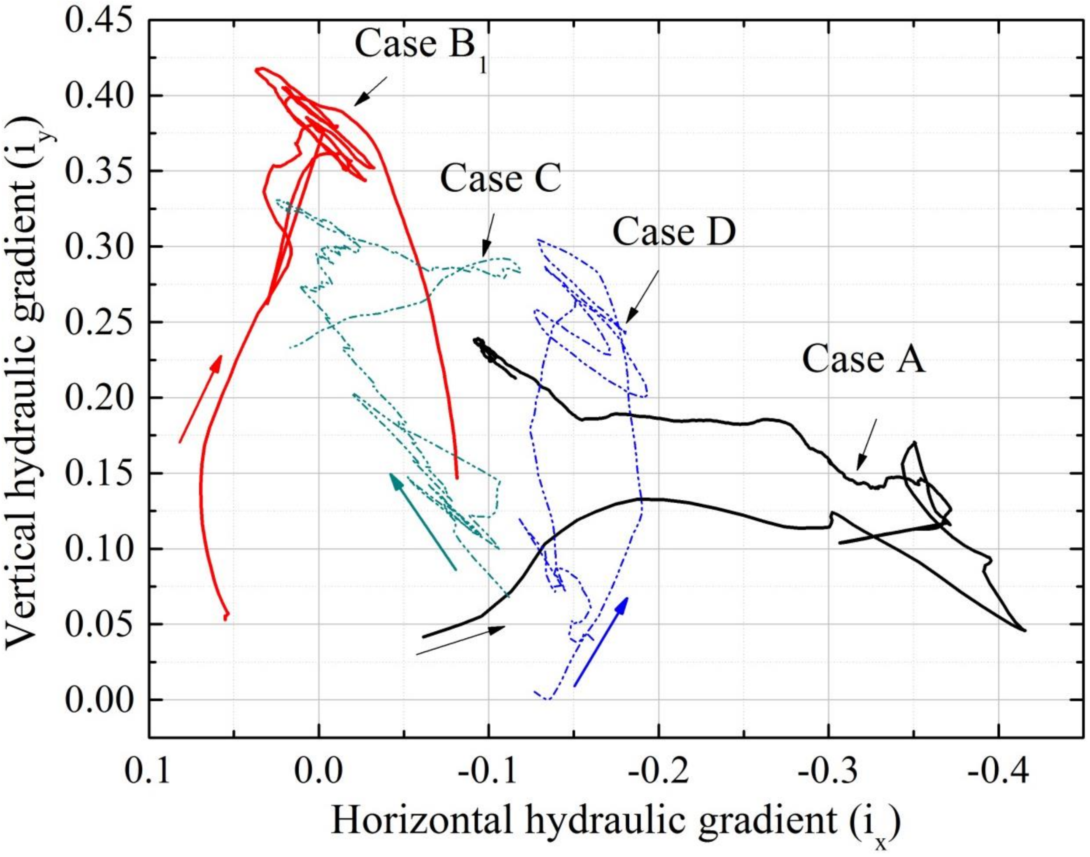

Figure 5.10 Relationships between horizontal and vertical hydraulic gradients in the mound.

5.4 Summary

It was found that scour depth and width due to tsunami overtopping was found to increase when seepage flow was combined with it. It was also found that two countermeasures could reduce the scour depth owing to not only the physical reinforcement effects but also due to the change of hydraulic gradient and transportation characteristics of scoured soil in the mound.

CHAPTER 6

SIMULATIONS OF SCOUR BY SPH

6.1 Introduction

Chapter 6 presents the simulations of scour by SPH. Simulations were performed for the experimental cases described in the previous chapter. Simulations of scour were performed by two phase SPH model. Two phase model is based on seepage force due to relative velocity between water and soil. Table 6.1 provides the simulation cases keeping similarity with the experiment.

Table 6.1 Simulations of scour by SPH.

Identification	h(cm)	Countermeasures	Description
Case A	0	None	Only overtopping
Case B_1	5.0	None	Overtopping + seepage
Case B_2	7.5	None	Overtopping + seepage
Case C	5.0	Widening and raising of embankment	Overtopping + seepage
Case D	5.0	Widening and raising of embankment + sheet pile	Overtopping + seepage

6. 2 Simulation of scour: Case A

In the scour model, water soil interaction defined in chapter 4 is considered. Whirlpool diameters, $R=g^{-1/4}q^{1/2}z_f^{1/4}$, where q is the flow rate (m^3/s/m), z_f (m) is the fall heights, is the considered the key parameters for scour. The flow rate q was set to be 0.015(m^3/s/m), and the falling height z_f was set to be 0.135m. This combination of q and z_f made the whirlpool diameter R to be the same value as in experiment, 0.04 m in each simulation. Table 6.2 summarizes the parameters for simulation of scour for case A. Figure 6.1 shows simulation condition clearly. Figure 6.2 shows progress of scour, velocity and seepage force vectors. Figure 6.3 and photo 6.1 show the scoured profile for case A observed in simulation and in experiment. Both the scoured profiles look similar with a little difference. Actually, in experiment scoured profile is the result of impact force, particle detachment, transportation and resettling of the scoured particles. However, in the simulation scoured profile is the result of impact force only.

Table 6.1 Parameters for simulation of scour Case A.

Number of soil particles	1300
Initial number of water particles	1822
Initial particle spacing (m), Δd	0.005
Smoothing length (m), h	0.006
Duration of a time step (s), Δt	10^{-5}
Density for soils (kg/m^3)	2008
Density for water (kg/m^3)	1000
Theoretical coefficient of permeability (cm/s), k	0.10
Porosity, n	0.50
Frictional angle of soil (degree) , ϕ (c=0)	38
Artificial viscosity parameters α, β for soil	0.1, 0.1
Artificial viscosity parameters α, β for water	0.1, 0
XSPH co-efficient ε for water	0.01
Boundary type at rigid base	Non-slip
Boundary type at vertical wall	symmetric

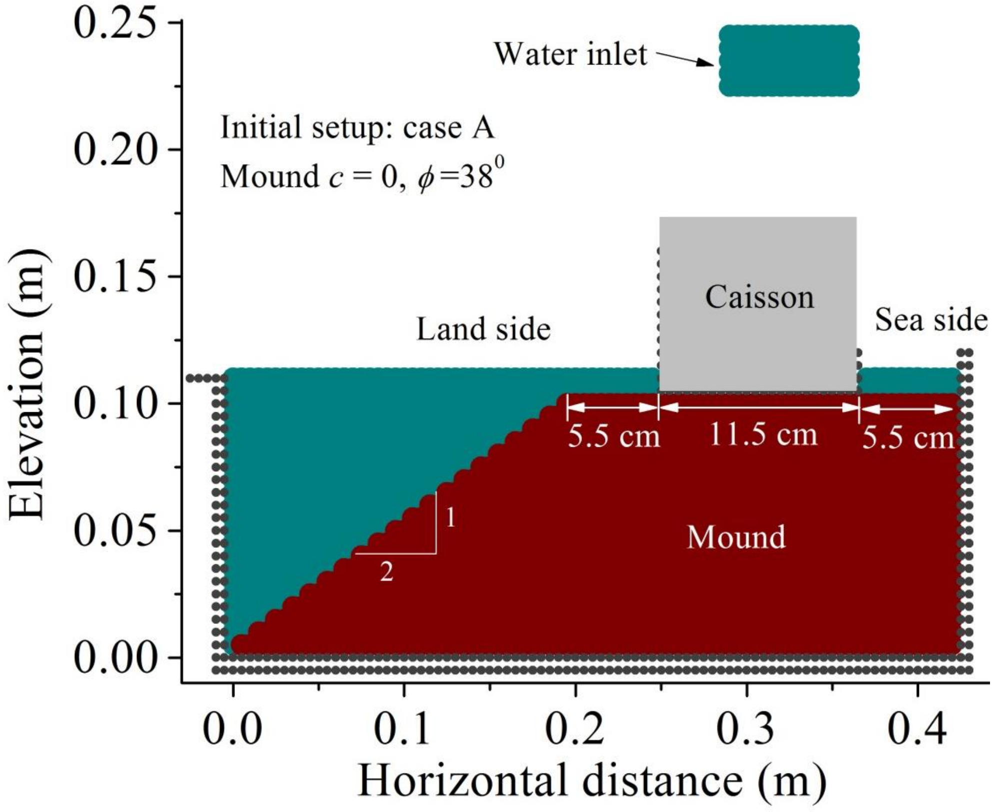

Figure 6.1 Initial set up for case A.

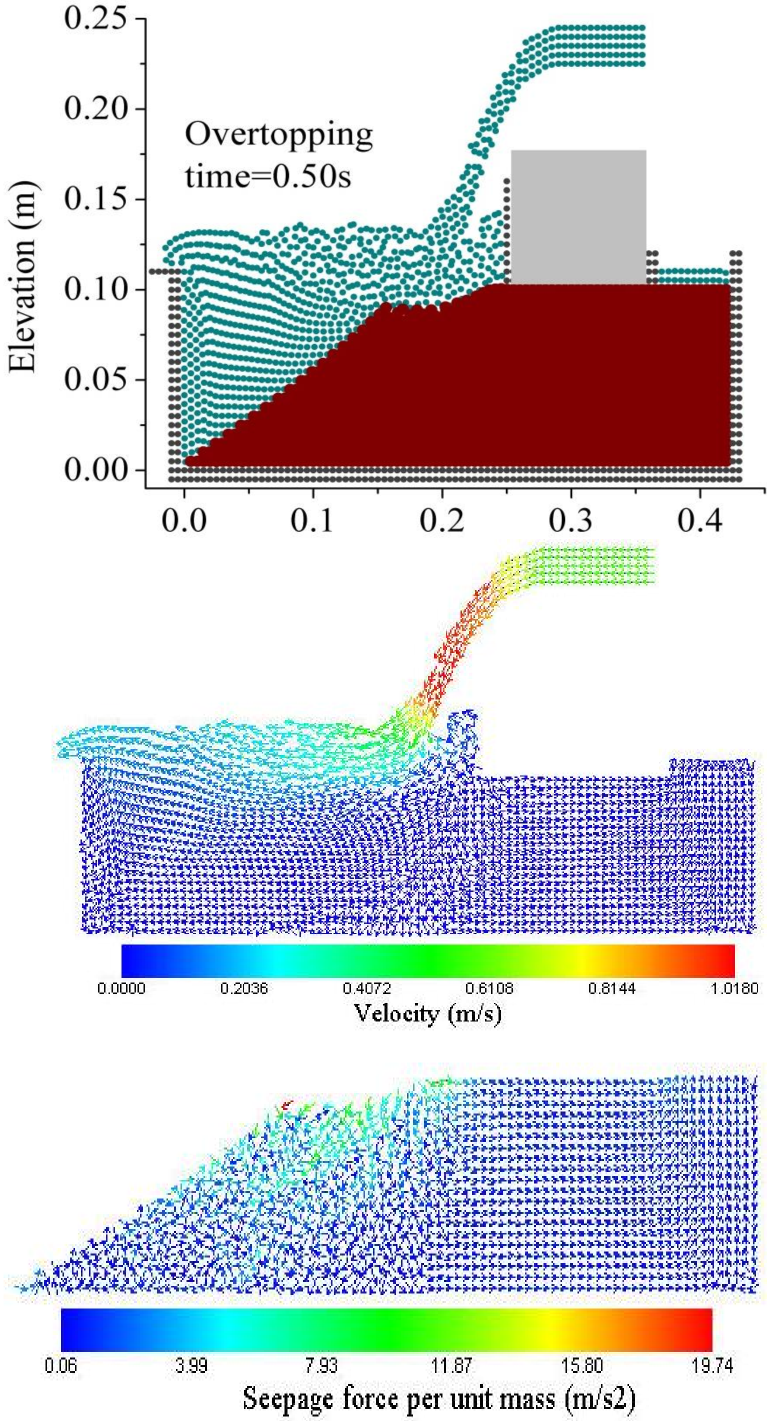

Figure 6.2 Scoured profile, velocity and seepage force distribution at overtopping time of 0.50second for case A.

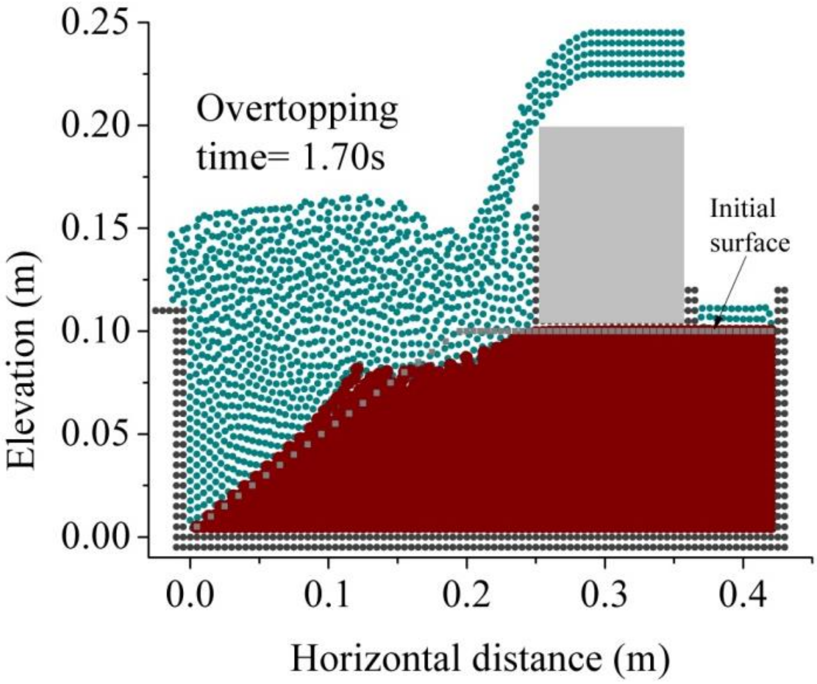

Figure 6.3 Scoured profile at overtopping time 1.70seconds for case A.

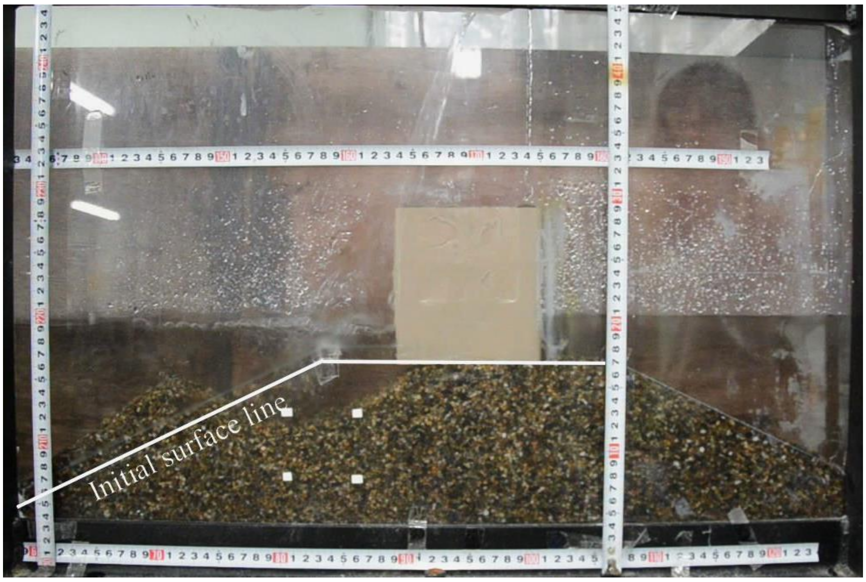

Photo 6.1 Scoured profile for case A in experiment.

6.3 Simulation of scour: Case B_1

Table 6.2 summarizes the parameters for simulation of scour for case B_1. Figure 6.4 shows simulation and seepage conditions just before the tsunami overtopping. Figure 6.5 shows progress of scour, velocity and seepage force vectors. Figure 6.6 shows the deviation of the scoured profile from the initial surface for case B_1 as observed in simulation. Figure 6.7 shows comparison of maximum shear strain distribution for case A and case B_1. It was found that maximum shear strain in case B_1 with a head difference h=5 cm was found higher than that of case A with a head difference h=0 cm.

Table 6.2 Parameters for simulation of scour case B$_1$.

Number of soil particles	1300
Initial number of water particles	1932
Initial particle spacing (m), Δd	0.005
Smoothing length (m), h	0.006
Duration of a time step (s), Δt	10^{-5}
Density for soils (kg/m^3)	2008
Density for water (kg/m^3)	1000
Theoretical coefficient of permeability (cm/s), k	0.10
Porosity, n	0.50
Frictional angle of soil (degree) , ϕ (c=0)	38
Artificial viscosity parameters α, β for soil	0.1, 0.1
Artificial viscosity parameters α, β for water	0.1, 0
XSPH co-efficient ε for water	0.01
Boundary type at rigid base	Non-slip
Boundary type at vertical wall	symmetric

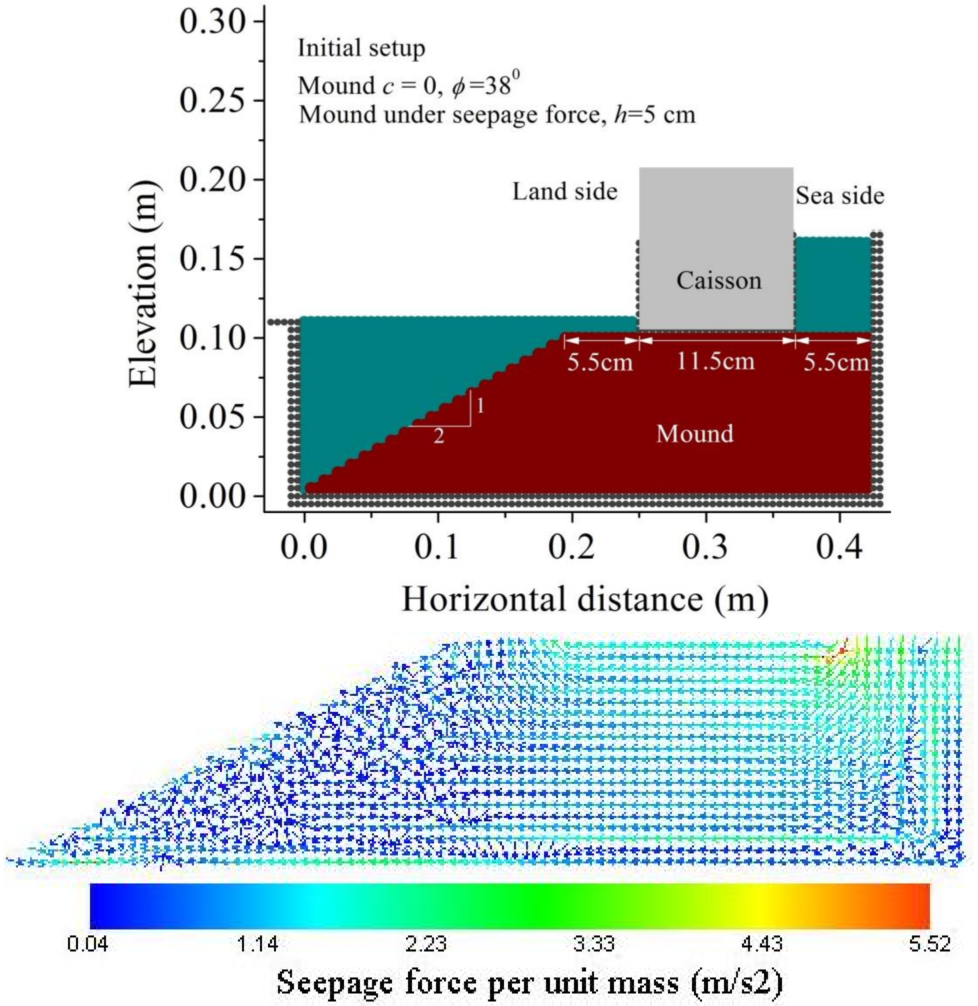

Figure 6.4 Initial setup and seepage condition just before tsunami overtopping for case B_1.

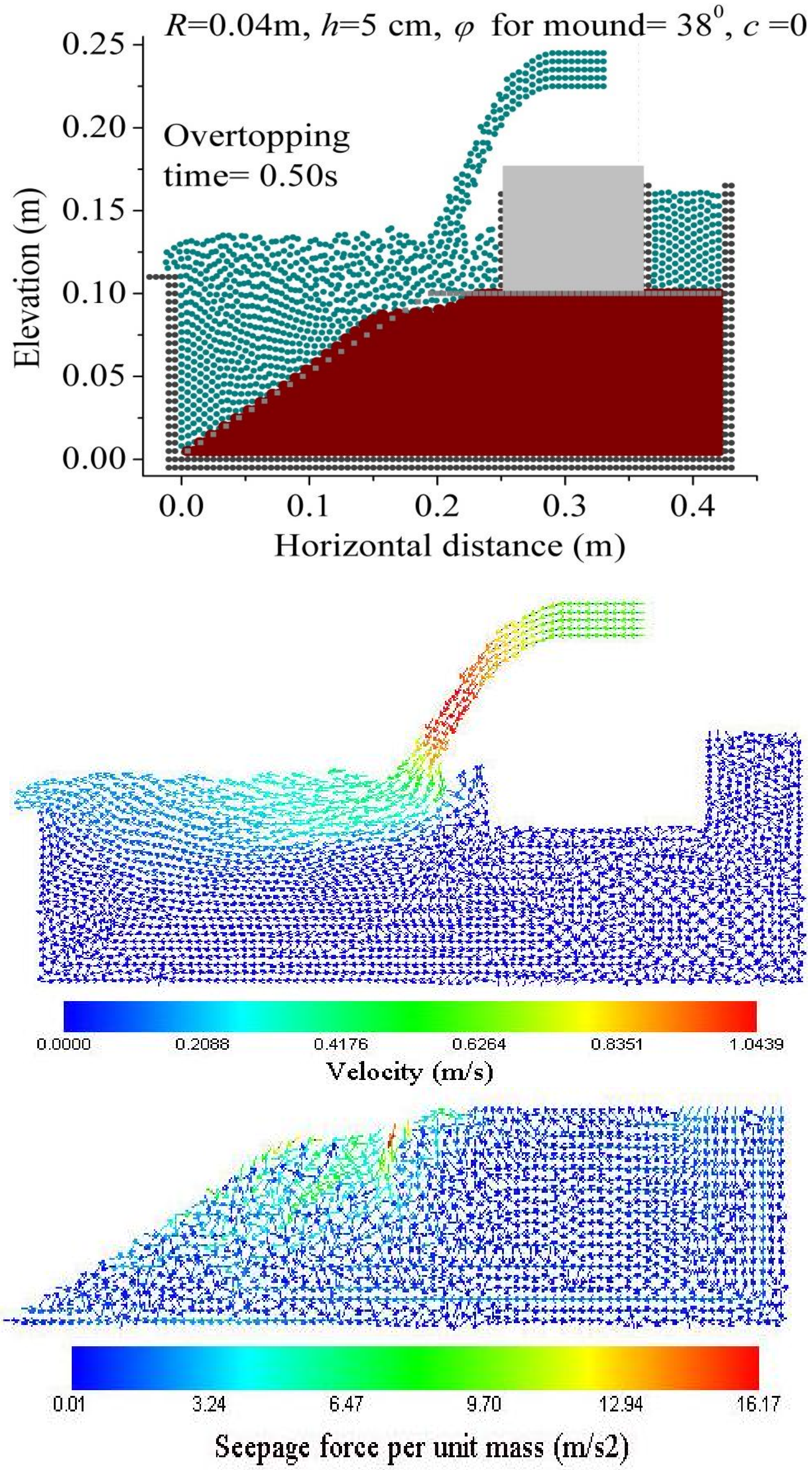

Figure 6.5 Scoured profile, velocity and seepage force distribution at overtopping time of 0.50second for case B_1.

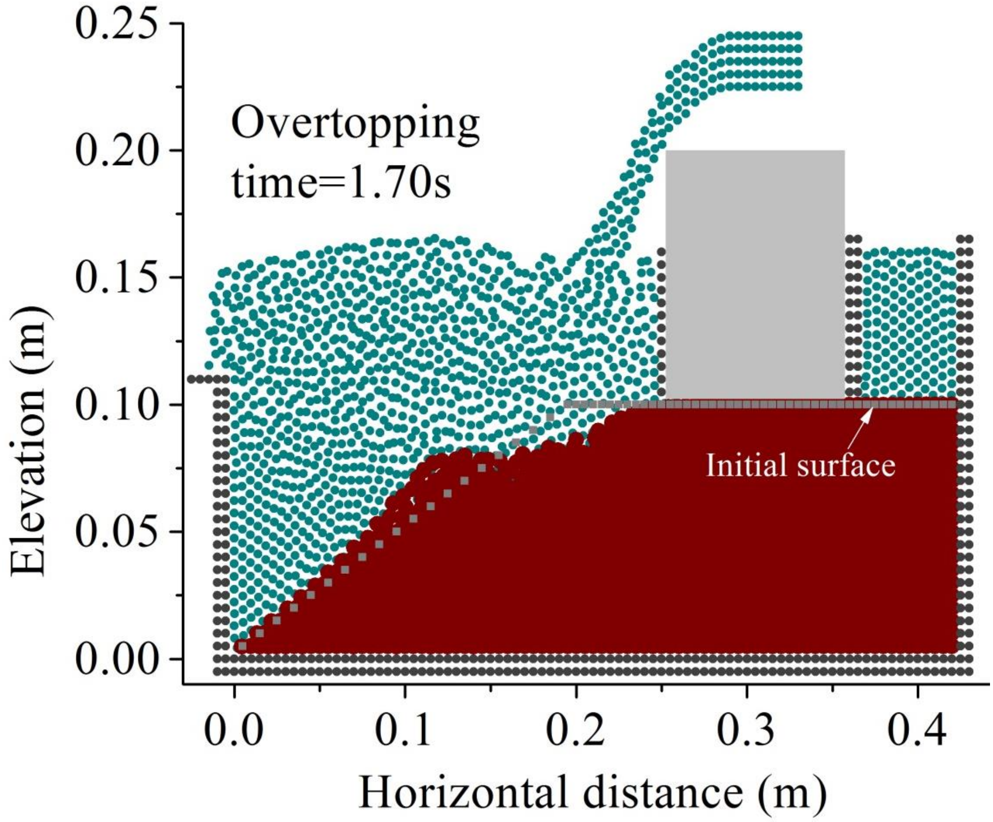

Figure 6.6 Scoured profile at overtopping time 1.70seconds for case B_1.

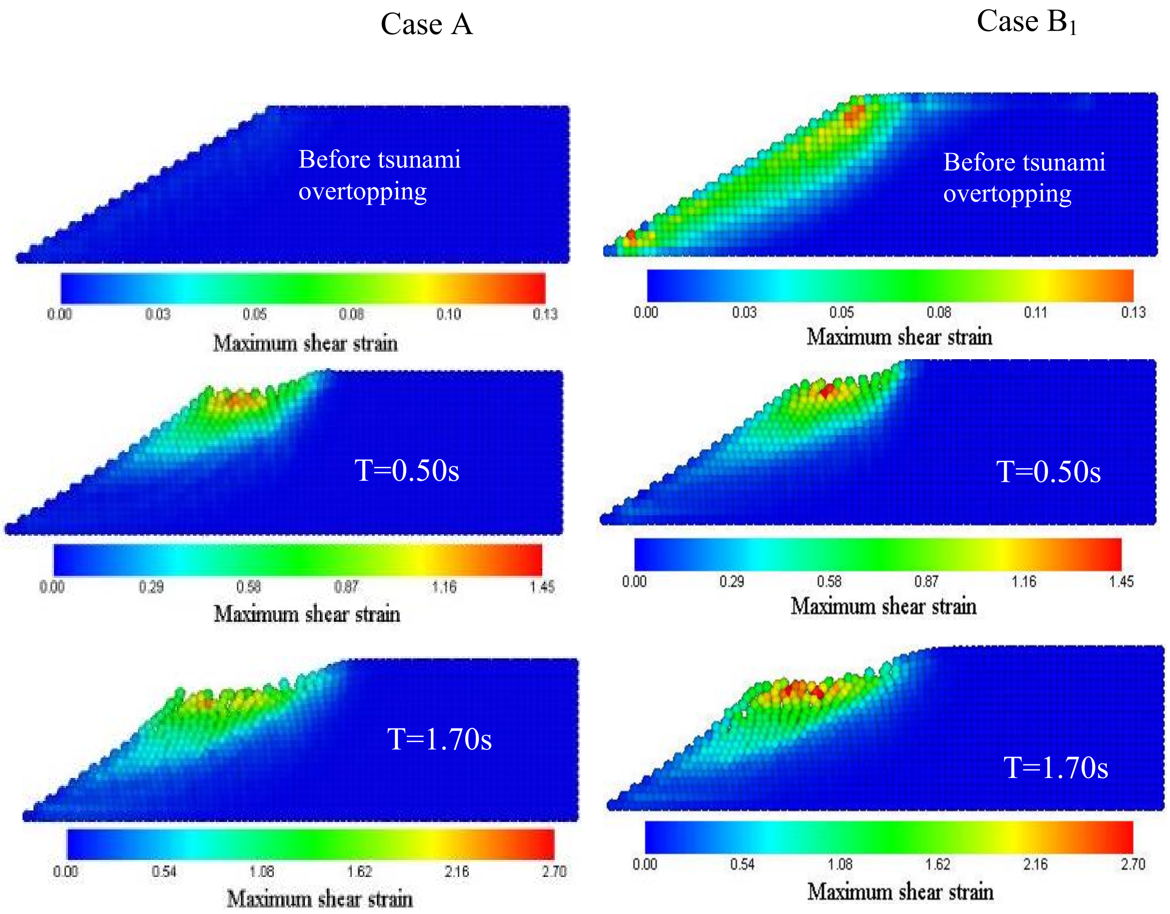

Figure 6.7 Comparison of maximum shear strain distribution for case A and case B_1.

6.4 Simulation of scour: Counter measure case C

Table 6.3 summarizes the parameters for simulation of scour for case C. Figure 6.8 shows simulation and seepage conditions just before the tsunami overtopping. Figure 6.9 shows progress of scour, velocity and seepage force vectors. Figure 6.10 shows the deviation of the scoured profile from the initial surface for case C as observed in the simulation.

Table 6.3 Parameters for simulation of scour case C.

Number of soil particles	1404
Initial number of water particles	1998
Initial particle spacing (m), Δd	0.005
Smoothing length (m), h	0.006
Duration of a time step (s), Δt	10^{-5}
Density for soils (kg/m^3)	2008
Density for water (kg/m^3)	1000
Theoretical coefficient of permeability (cm/s), k	0.10
Porosity, n	0.50
Frictional angle of soil (degree) , ϕ (c=0)	38
Artificial viscosity parameters α, β for soil	0.1, 0.1
Artificial viscosity parameters α, β for water	0.1, 0
XSPH co-efficient ε for water	0.01
Boundary type at rigid base	Non-slip
Boundary type at vertical wall	symmetric

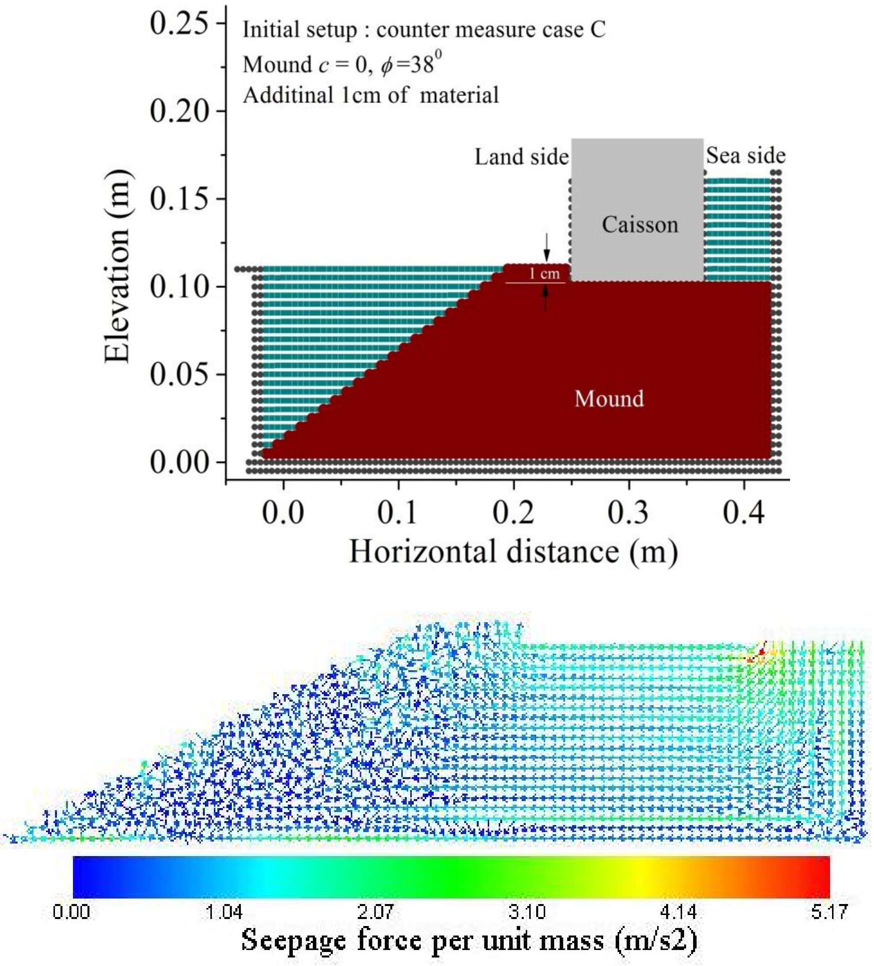

Figure 6.8 Initial set up and seepage condition just before tsunami overtopping case C.

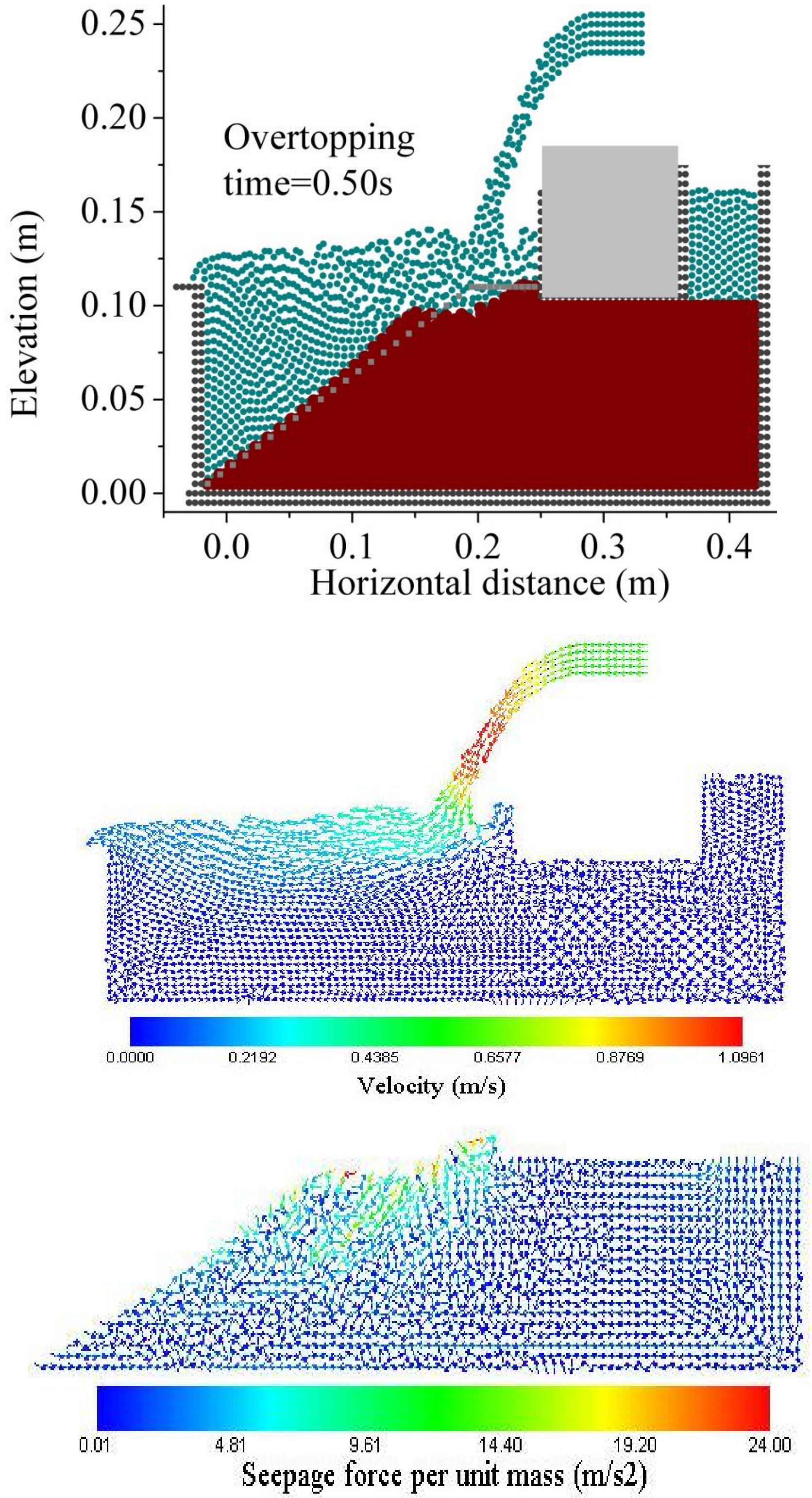

Figure 6.9 Scoured profile, velocity and seepage force distribution at overtopping time of 0.50second for case C.

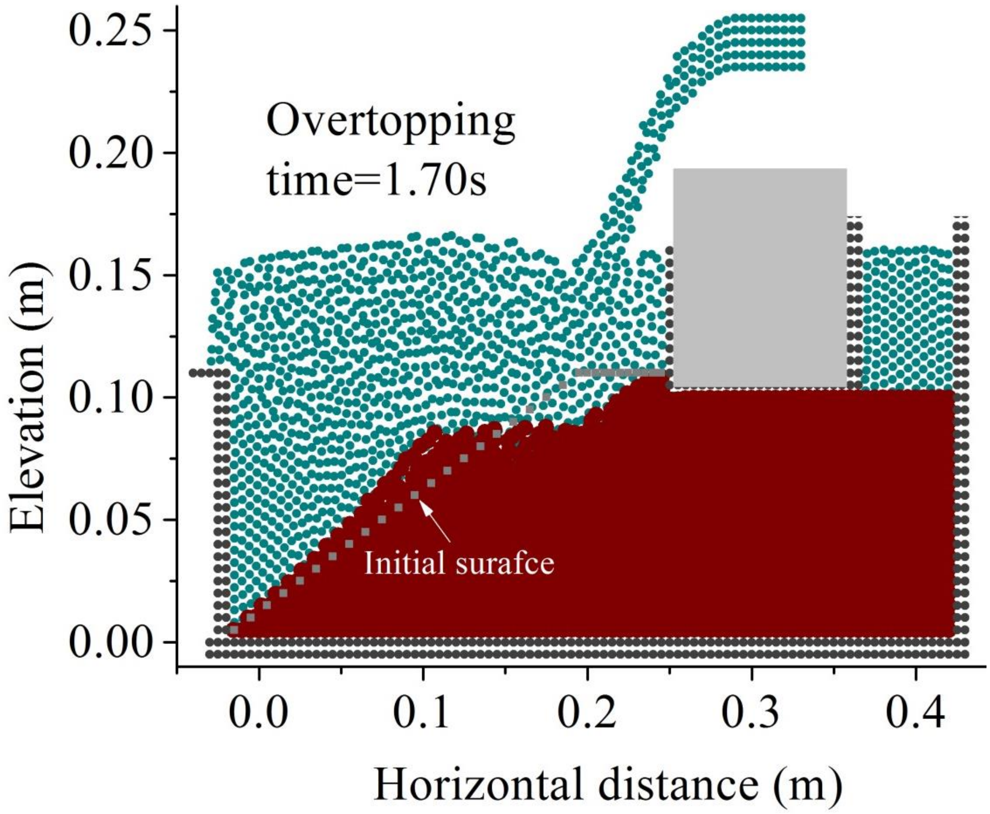

Figure 6.10 Scoured profile at overtopping time 1.70seconds for case C.

6.5 Simulation of scour: Counter measure case D

Table 6.4 summarizes the parameters for simulation of scour for case D. Figure 6.11 shows simulation condition and seepage forces just before the tsunami overtopping. Figure 6.12 shows progress of scour, velocity and seepage force vectors. Figure 6.13 shows the deviation of the scoured profile from the initial surface for case D as observed in the simulation. Figure 6.14 shows comparison of maximum shear strain for case C and case D. Just before the tsunami overtopping case C with *h*=5 cm shows higher value of maximum shear strain than that of case D for the influence of seepage flow. However, case D having a sheet pile, it does not have any seepage flow for head difference. However, after the start of tsunami overtopping, no definite trend was found in maximum shear strain between the case C and case D. It appeared that influence of tsunami overtopping was strong enough to ignore the influence of head difference.

Table 6.4 Parameters for simulation of scour case D.

Number of soil particles	1404
Initial number of water particles	1998
Initial particle spacing (m), Δd	0.005
Smoothing length (m), h	0.006
Duration of a time step (s), Δt	10^{-5}
Density for soils (kg/m^3)	2008
Density for water (kg/m^3)	1000
Theoretical coefficient of permeability (cm/s), k	0.10
Porosity, n	0.50
Frictional angle of soil (degree) , ϕ (c=0)	38
Artificial viscosity parameters α, β for soil	0.1, 0.1
Artificial viscosity parameters α, β for water	0.1, 0
XSPH co-efficient ε for water	0.01
Boundary type at rigid base	Non-slip
Boundary type at vertical wall	symmetric

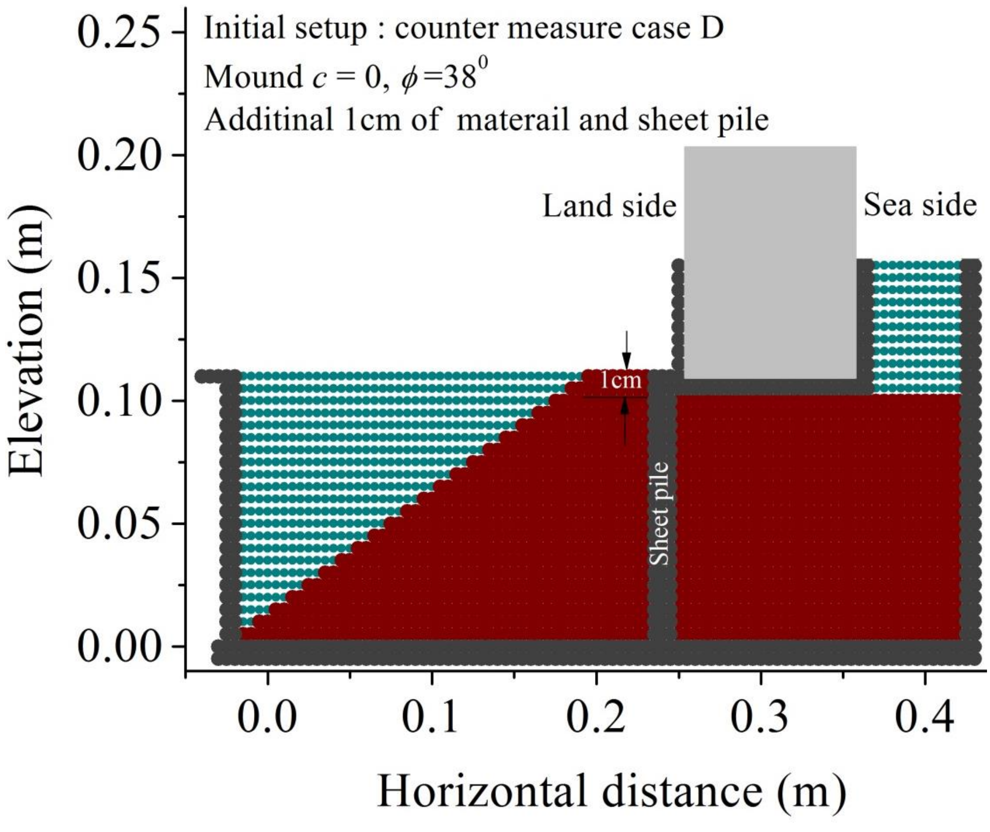

Figure 6.11 Initial set up for case D.

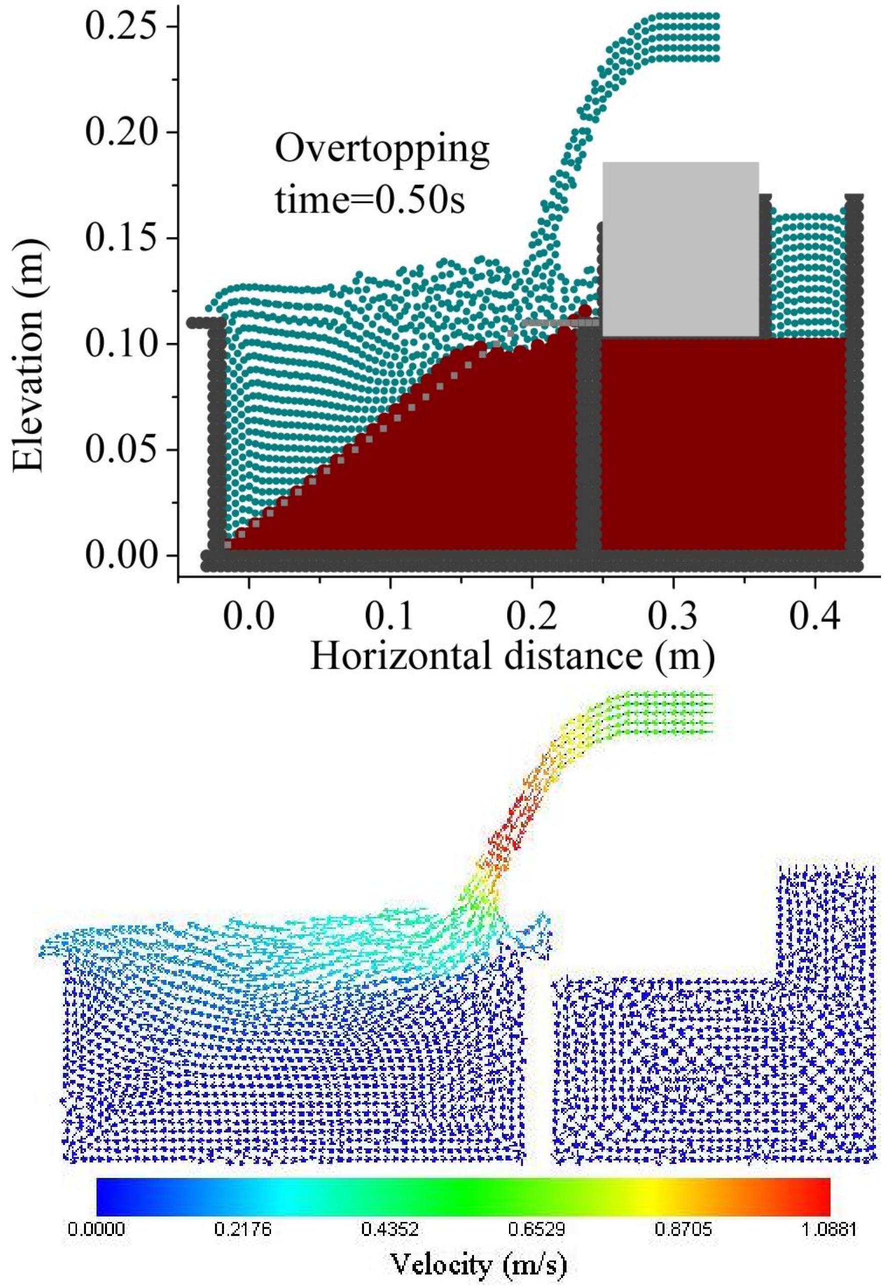

Figure 6.12 Scoured profile, velocity distribution at overtopping time of 0.50second for case D.

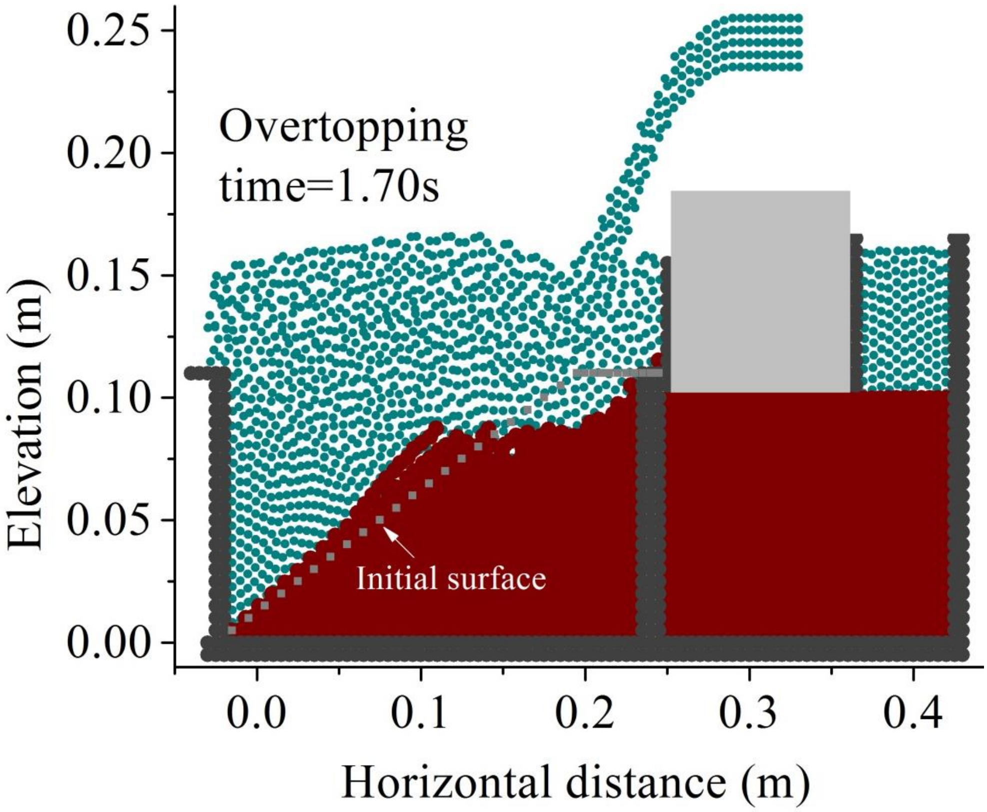

Figure 6.13 Scoured profile at overtopping time of 1.70 second for case D.

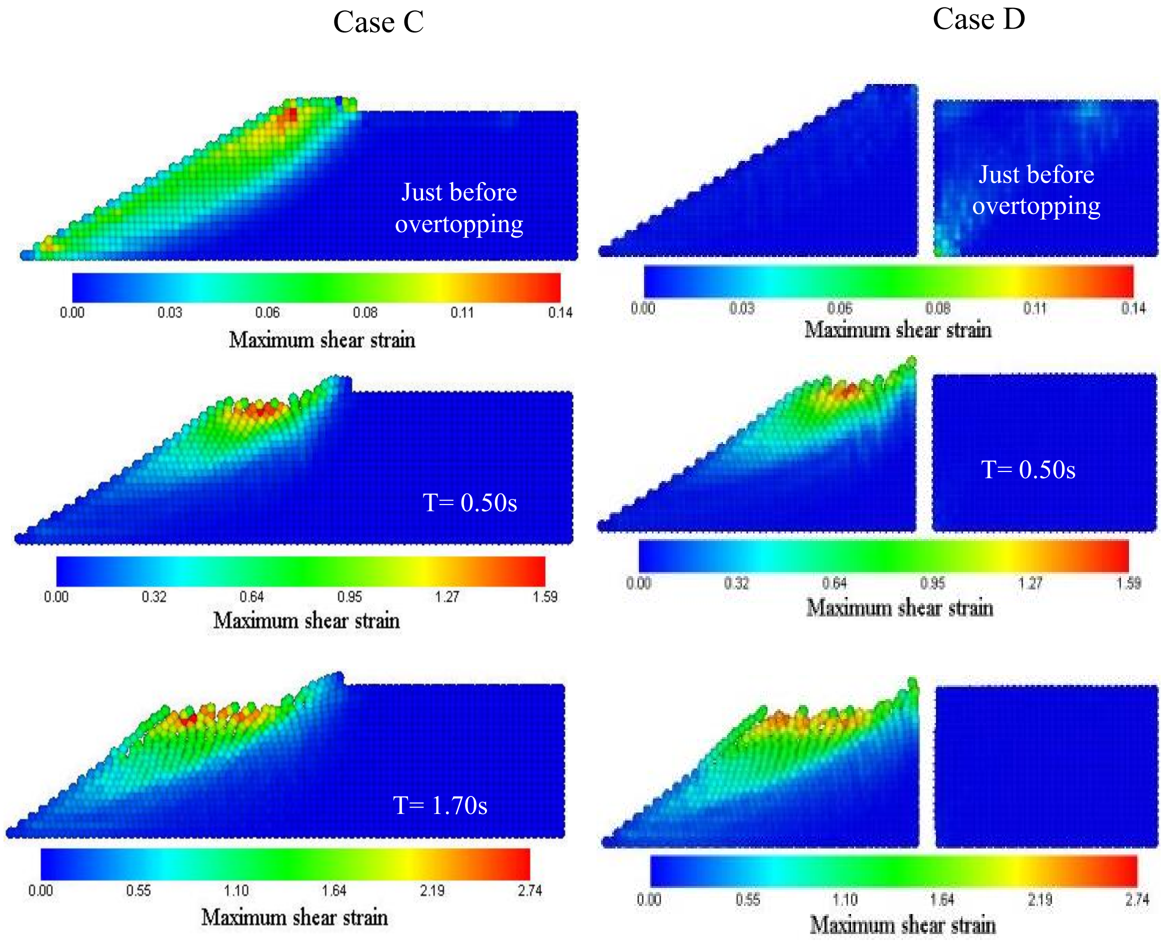

Figure 6.14 Comparison of maximum shear strain distribution for case C and case D.

6.6 Comparison of scour with experiment

In the experiment, water head in the seaside was gradually raised to make the head difference. Steady state seepage flow was ensured before the tsunami overtopping. Duration of the experiment time was approximately 100 seconds. However, in the simulations water head in the seaside was not raised gradually rather it was raised at once. Duration of the simulation was 3.7 seconds. Figure 6.15 shows scour data for experiment and simulation. It was found that the trends of scour curves in simulations for all the cases are qualitatively same with that in experiment. It was found that maximum scour depth for case B_1 is higher than that of case A by 0.50 cm in experiment and 0.28 cm in simulation. That means when seepage forces are combined with tsunami overtopping scour depth increases. It was also found that with the effect of the countermeasure scour depths were reduced both in experiment and simulation.

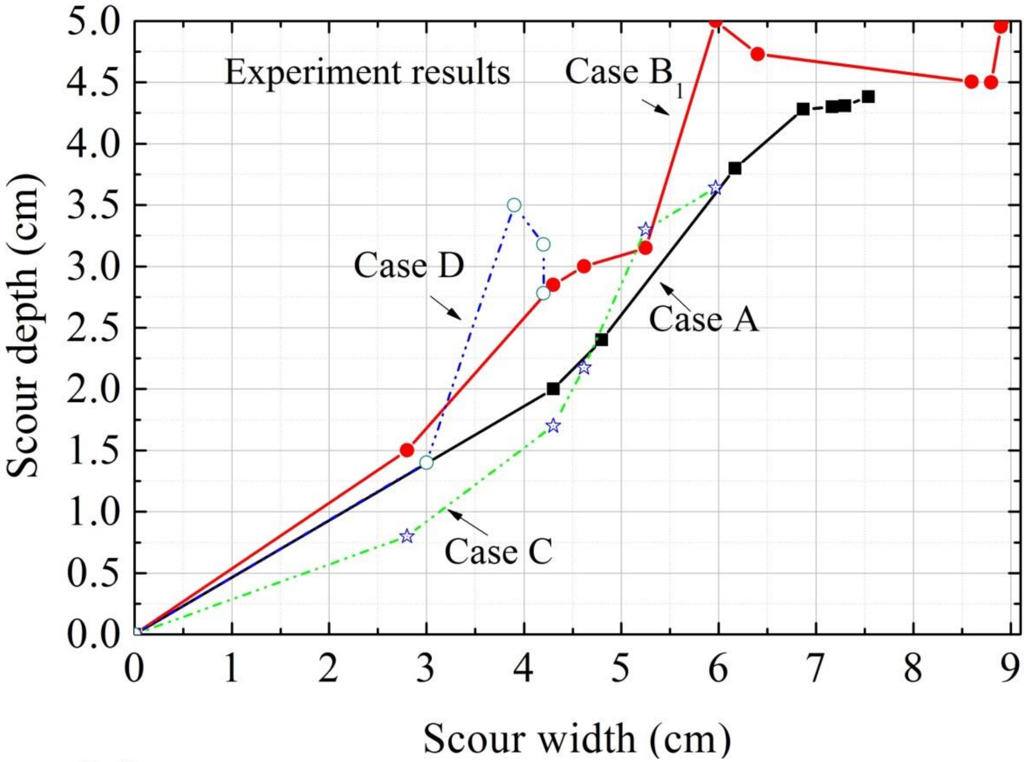

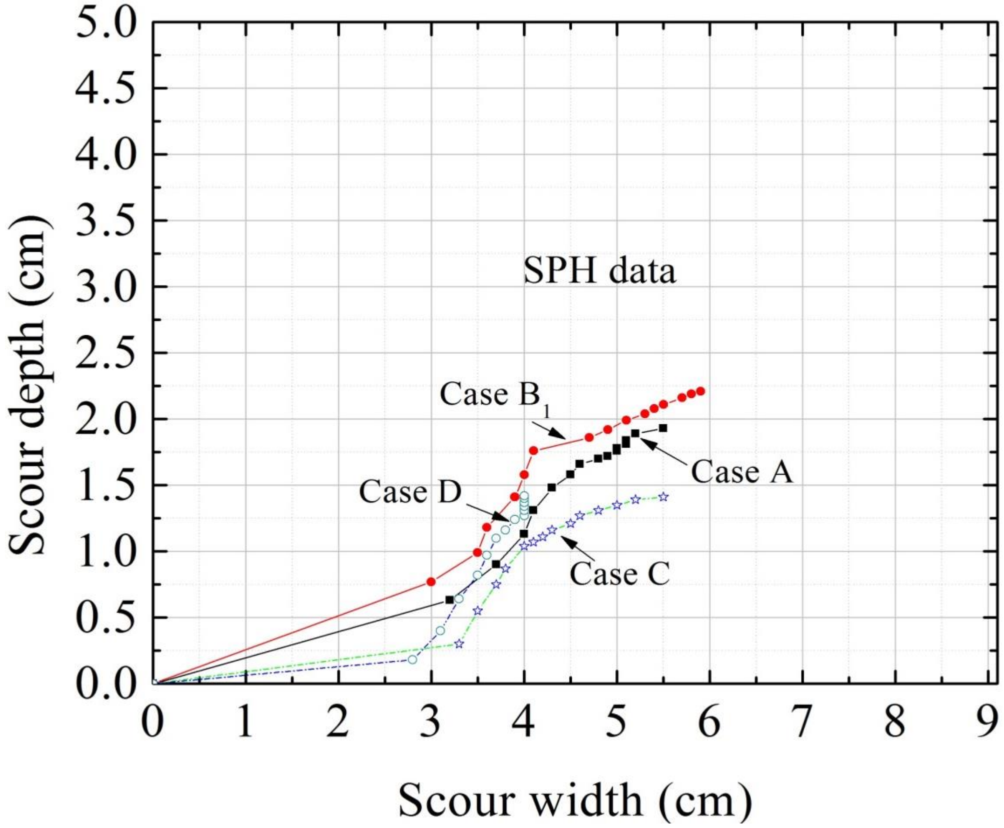

Figure 6.15 Comparison of scour between simulation and experiment data.

6.7 Simulation of scour: Case B_2

Table 6.5 summarizes the parameters for simulation of scour for case B_2. Figure 6.16 shows simulation condition and active seepage force just before the tsunami overtopping. Figure 6.17 shows progress of scour, velocity and seepage force vectors. Figure 6.18 shows the deviation of the scoured profile from the initial surface for case B_2 as observed in the simulation. Figure 6.19 shows comparison of maximum shear strain for case C and case D. Just before the tsunami overtopping case C with h=5 cm shows higher value of maximum shear strain than that of case D for the influence of seepage flow. However, case D having a sheet pile, does not have any seepage flow for head difference. After the start of tsunami overtopping, no definite trend was found in maximum shear strain between the case C and case D. It appeared that influence of tsunami overtopping was strong enough to ignore the influence of head difference.

Table 6.5 Parameters for simulation of scour case B_2.

Number of soil particles	1300
Initial number of water particles	1987
Initial particle spacing (m), Δd	0.005
Smoothing length (m), h	0.006
Duration of a time step (s), Δt	10^{-5}
Density for soils (kg/m^3)	2008
Density for water (kg/m^3)	1000
Theoretical coefficient of permeability (cm/s), k	0.10
Porosity, n	0.50
Frictional angle of soil (degree) , ϕ (c=0)	38
Artificial viscosity parameters α, β for soil	0.1, 0.1
Artificial viscosity parameters α, β for water	0.1, 0
XSPH co-efficient ε for water	0.01
Boundary type at rigid base	Non-slip
Boundary type at vertical wall	symmetric

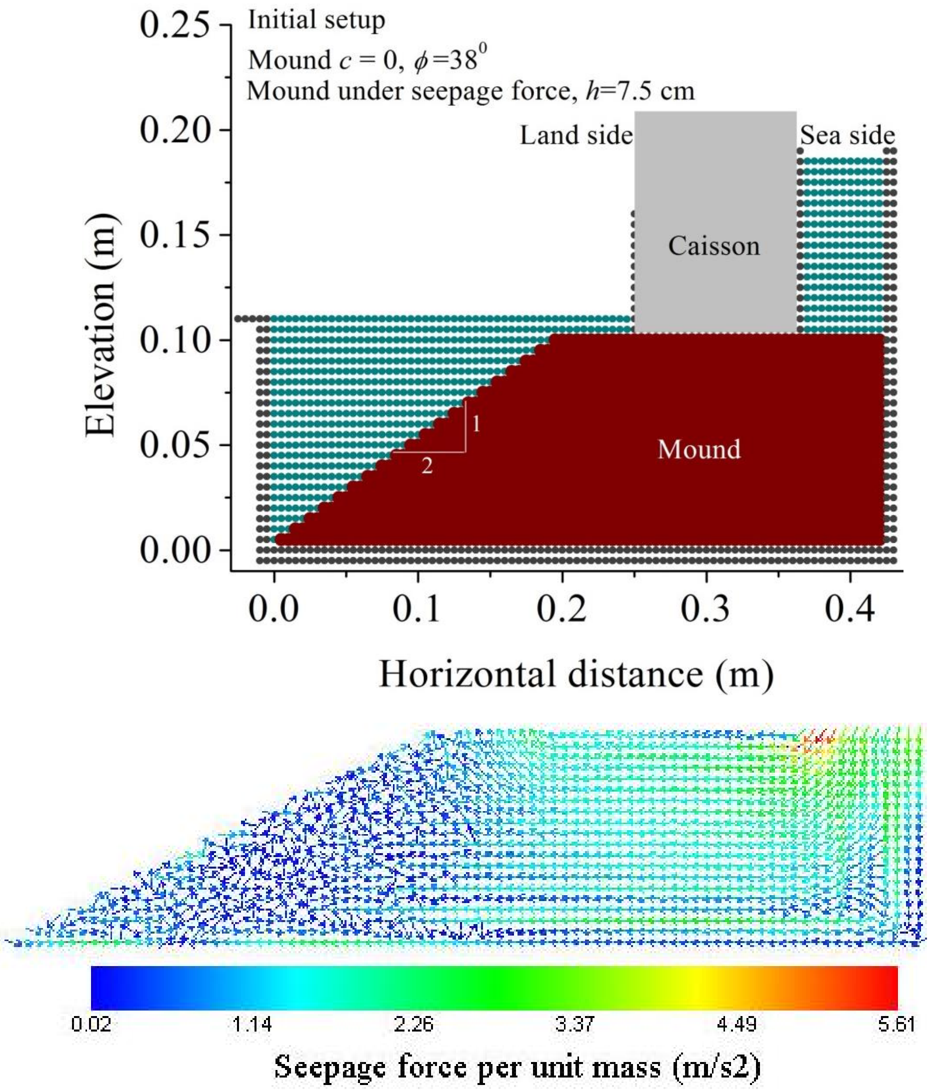

Figure 6.16 Initial setup and seepage condition just before tsunami overtopping for case B_2.

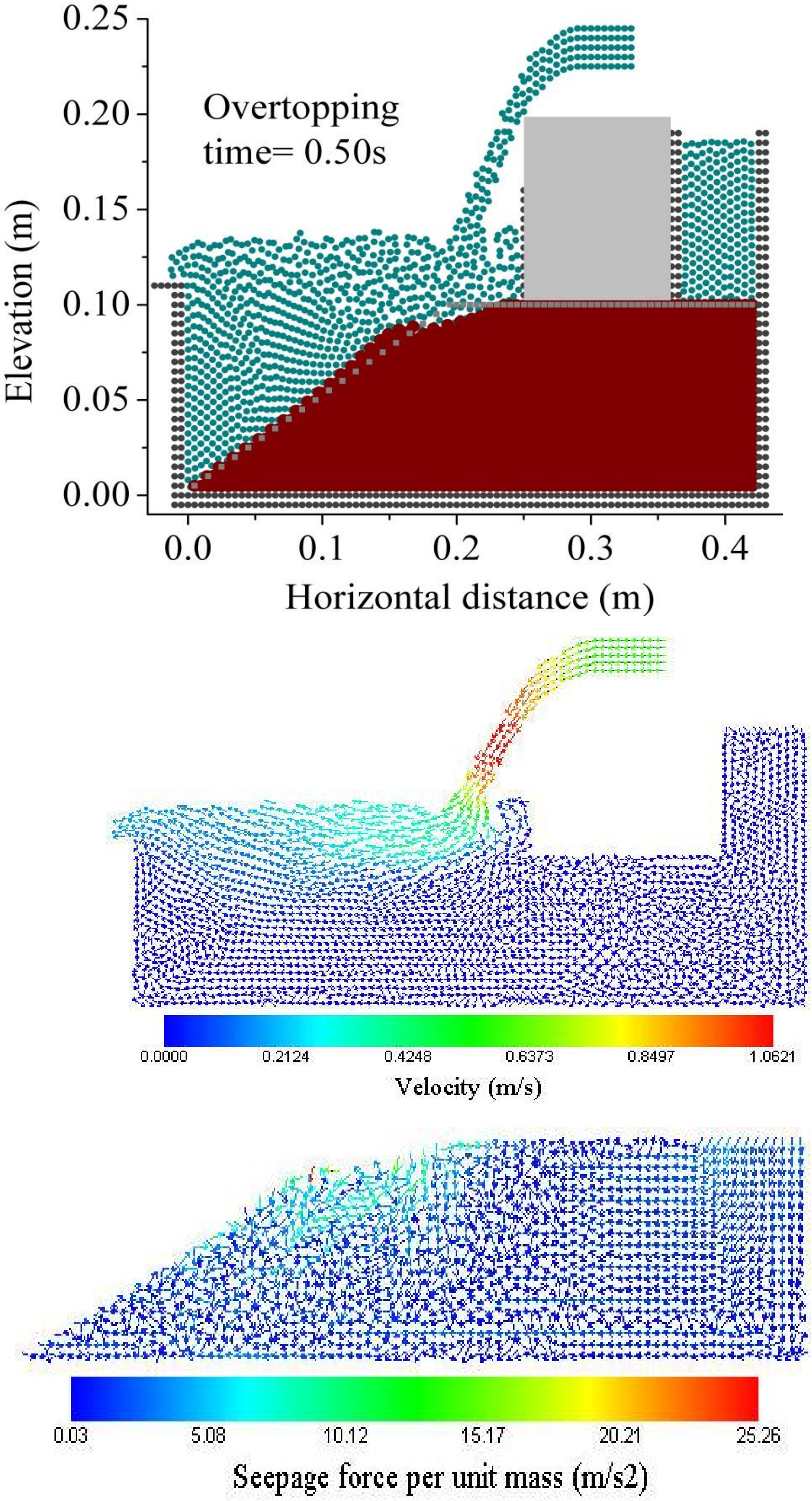

Figure 6.17 Scoured profile, velocity distribution at overtopping time of 0.50second for case B_2.

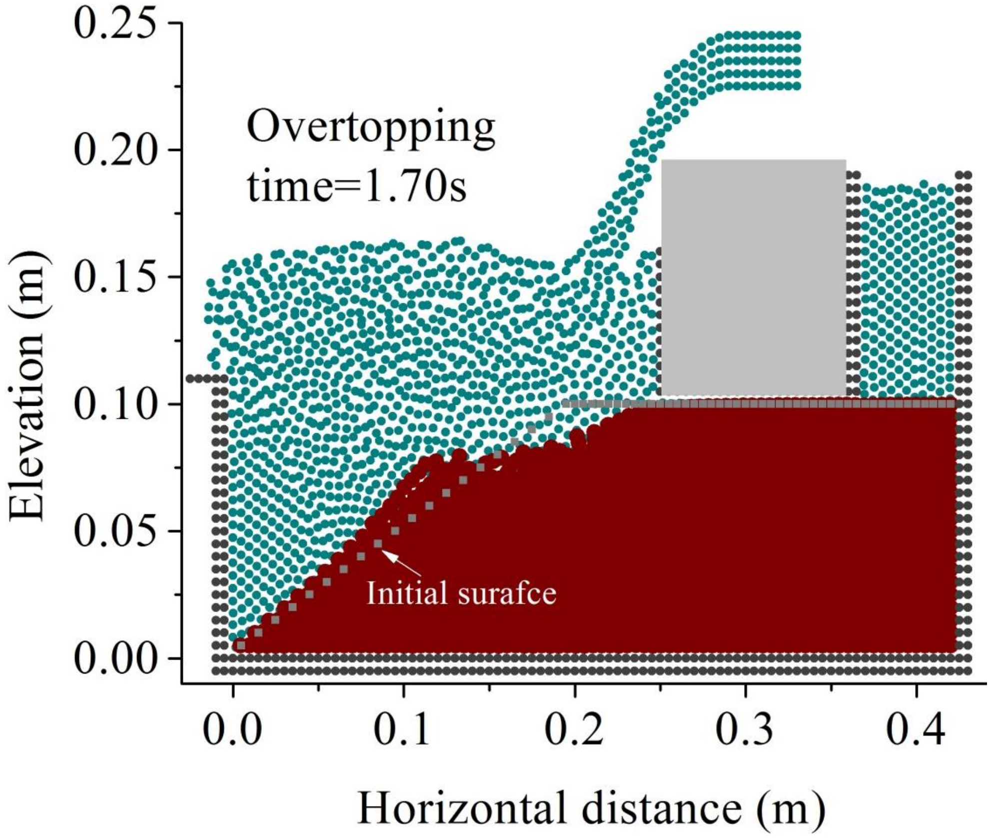

Figure 6.18 Scoured profile at overtopping time of 1.70 seconds for case B_2.

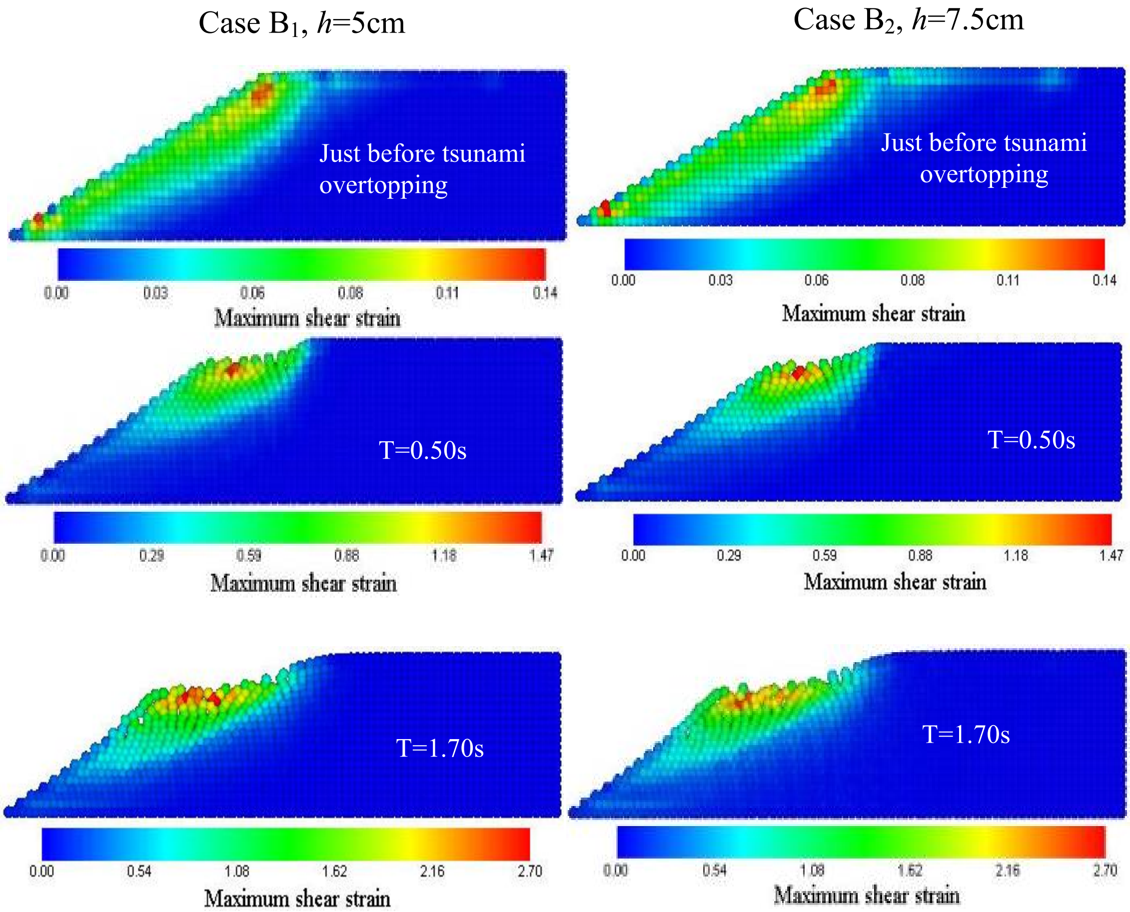

Figure 6.19 Comparison of maximum shear strain distribution for case B_1 and case B_2.

6.8 Comparison of scour for various head difference

Figure 6.20 shows comparison of scour depths for various head difference. It was found that when head difference was increased from 0 cm to 5 cm scour depth was found to be increased by 0.28 cm. Moreover, when head difference was increased from 5 cm to 7.50 cm , scour depth was increased by 0.03 cm. Figure 6.21 shows comparison of scour widths for various head difference. It was found that when head difference was increased from 0 cm to 5 cm scour width was found to be increased by 0.40 cm. Moreover, when head difference was increased from 5 cm to 7.50 cm, scour width was increased by 1.20 cm.

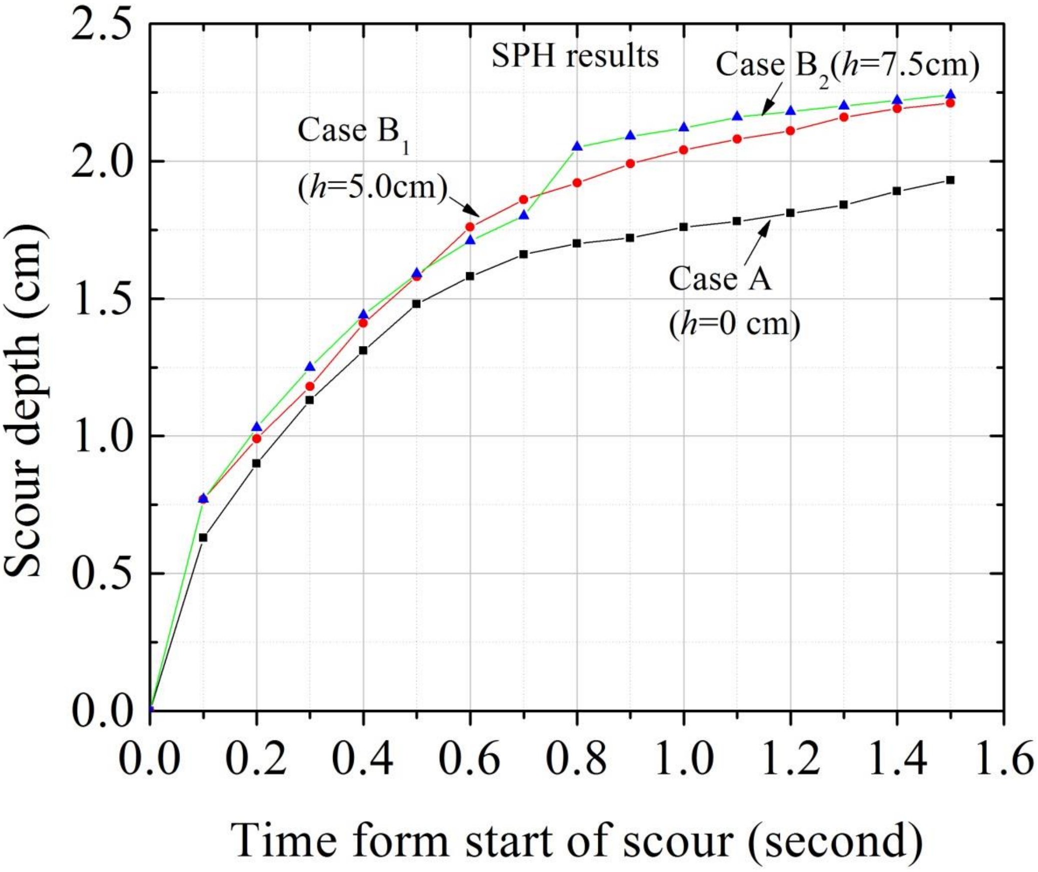

Figure 6.20 Scour depths for various head difference.

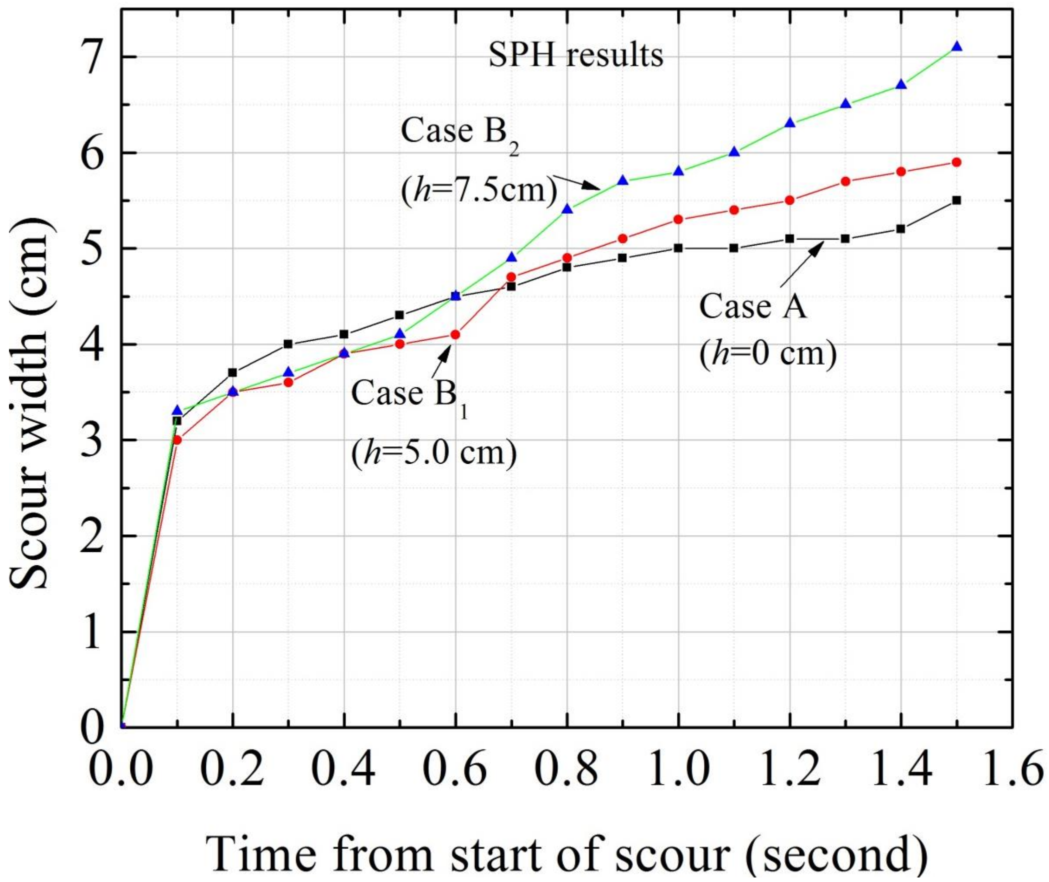

Figure 6.21 Scour widths for various head difference.

6.9 Summary

From the SPH simulation it was found that scour depth increased when tsunami overflow was combined with seepage flow. Moreover, two countermeasures were found to reduce the scour depth. So, it can be said that SPH results are qualitatively same as the experiments. Moreover, scour with head difference "*h*" of 0 cm, 5 cm, and 7.5 cm between seaside and landside were simulated. It is found that both scour depths and widths has increased with the increase of "*h*" as shown in figure.

CHAPTER 7

CONCLUSIONS AND RECOMMENDATIONS

7.1 Conclusions

The objective of the study was to investigate the deformation behavior of a breakwater mound during scour. To achieve the objective it was necessary to conduct both experiment and numerical simulation. SPH was used as the numerical tool. It was necessary to develop the SPH code with ability to simulate water flow, deformation behavior of the geo-material and water-soil coupling behavior. It was also important to check the accuracy of the SPH code prior to attempting the final objective.

In chapter 2, validity of the SPH code for water was performed by simulating couette flow, shear cavity, dam break flow. Simulation results were compared with corresponding analytical/ experimental results. SPH results were found to match both qualitatively and quantitatively with the corresponding analytical/ experimental results.

In chapter 3, SPH code for elastic perfectly plastic soil model with Drucker-Prager failure criteria has been validated by performing simulations for simple shear test, granular flow test, bearing capacity test. Simulation results were compared with the corresponding analytical/ experimental results. SPH simulations results were found to match both qualitatively and quantitatively with corresponding analytical/ experimental results

In chapter 4, SPH simulations on permeability and boiling were performed by water-soil coupling model. Simulation results of permeability test were found to match with the analytical solution both qualitatively and quantitatively. So, SPH is capable of simulating flow of water through porous soil. Boiling in experimental conditions was simulated with SPH. It was found that generation of heave was observed in the simulation with head difference of 3.85cm higher than that of the experimental conditions. However, sudden and complete wash out after the heave generation was not observed in the simulation.

In chapter 5, from experiment results, it was found that scour depth and width increased when seepage flow was combined with the tsunami flow. It was found that two countermeasures could reduce the scour depth and width. Reduction in scour depth was not only for physical reinforcement effect. It was also for the change of hydraulic gradient and transportation characteristics of scoured soil in the mound.

In chapter 6, simulations of scour with validated SPH code were performed. From the simulations it was found that scour depth and width increased when tsunami overflow was combined with seepage flow. Moreover, two countermeasures were found to reduce the scour depth and width. It was found that scour results for all cases followed the same trend as found in the experiment. Moreover, scour with head difference "*h*" of 0 cm, 5 cm, and 7.5 cm between seaside and landside were simulated. It is found that both scour depths and widths have increased with the increase of "*h*".

It was found from both experiment and numerical simulations that deformation behavior due to scour during tsunami overtopping were influenced by the head difference between seaside and landside of the breakwater.

7.2 Recommendations for future work

- ➢ The SPH simulation was performed in two dimensional conditions. It is important to simulate in three dimensional conditions to produce realistic results. However, without accelerating the computational speed three dimensional analyses will be meaningless. To increase computational speeds it necessary to adopt parallel computation technique.

- The simulation was done under experimental conditions. However, it is important to simulate actual conditions.

- In this study, simulation of scour was performed without considering transportation and resettling of the scoured materials. It is necessary to consider them while simulating scour.

- In this study elastic perfectly plastic soil model was considered. However, sometimes it is very difficult to achieve realistic soil behavior by elastic perfectly plastic model. So, more realistic soil model should be implemented for achieving better results.

- Deformation behaviour of dry soil was found perfect in simulation. However, deformation behavior of saturated soil specially boiling response was slow in water-soil coupling model. In the water-soil coupling model, water flow was found to be accurate. So, it is important to improve the deformation behavior of saturated soil.

REFERENCES

Arikawa T., Sato M., Shimosako K., Hasegawa I., Yeom Gyeong-Seon and Tomita T (2012). " Failure mechanism of Kamaishi breakwater due to the great east Japan earthquake tsunami", available: http://journals.tdl.org/icce/index.php/icce/article/viewFile/6845/pdf.

Bui, H. H., Fukagawa, R., Sako, K. and Ohno, S. (2008a). "Lagrangian meshfree particles method (SPH) for large deformation and failure flows of geomaterial using elastic - plastic soil constitutive model", International Journal for Numerical and Analytical Methods in Geomechanics, Vol.32, pp.1537-1570.

Bui, H. H., Fukagawa, R., Sako, K. and Wells J.C. (2008b). "SPH-based numerical simulations for large deformation of geomaterial considering soil-structure interaction", Proceedings of the 12th International Conference of International Association for Computer Methods and Advances in Geomechanics (IACMAG)1-6 October, 2008 , Goa, India, pp. 570-578.

Bui Ha H., K. Sako and R. Fukagawa (2007). "Numerical simulation of soil-water interaction using smoothed particle hydrodynamics (SPH) method", Journal of terramechanics 44 (2007) pp.339-346.

Bui, H. H., Fukagawa, R., Sako, K. and Wells J.C. (2011a). "Slope stability analysis and discontinuous slope failure simulation by elasto-plastic smoothed hydrodynamics (SPH)", Geotechnique 61, No.7, pp. 565-574.

Bui Ha H., Nguen C.T., K. Sako and R. Fukagawa (2011b). "A SPH model for seepage flow through deformable porous media", 6th international SPHERIC workshop, Hamburg, Germany, June 08-10, 2011.

Bui Ha H. and Fukagawa Ryoichi (2013). "An improved SPH method for saturated soils and its application to investigate the mechanisms of embankment failure: Case of hydrostatic pore-water pressure", International Journal for numerical and analytical methods in geomechanics, 2013; 37:pp. 31‐50.

Carla Antoci, Mario Gallati, Stefano Sibilla (2007). "Numerical simulation of fluid‐structure interaction by SPH", Computers and Structures 85 (2007) pp. 879‐890.

Chen J. K., Beraun J. E and Carney T.C (1999). "A corrective smoothed particle method for boundary value problems in heat conduction", Computer methods in applied mechanics and engineering, 46: 231-252.

Chen Wei and Qiu Tong (2011). "Numerical Simulations of Granular Materials using Smoothed Particle Hydrodynamics Method", Advances in Unsaturated Soil, Geo-Hazard, and Geo-Environmental Engineering: pp. 157-164, Geotechnical Special Publication No. 217, ASCE.

Das R., Cleary P.W. (2007). " Modelling Stress Wave Propagation and Triaxial Compression Test using Smoothed Particle Hydrodynamics", Proceedings of the 5th Australasian Congress on Applied Mechanics, ACAM 2007 10-12 December 2007, Brisbane, Australia.

Das R., Cleary P.W. (2006). “Uniaxial compression test and stress wave propagation modelling using SPH”, Proceedings of the 5th International Conference on CFD in the Process Industries CSIRO, Melbourne, Australia, 13-15 December 2006, pp.1-7.

Dong Simeng, Zen Kouki, Kasama Kiyonobu, Wang Bo, Takesue Akihiro (2012). “Theoretical and Experimental Study on Tsunami Induced Instability of Caisson Type Composite Breakwater”, memoirs of the Faculty of Engineering, Kyushu University, Vol.72, No.2 June, 2012.

G.R. Liu and M.B. Liu (2003). “Smoothed Particle Hydrodynamics; a meshfree particle method”, book, World Scientific Publishing Co. Pte. Ltd. (2003)

Grey JP, Monaghan JJ, Swift RP (2001). “SPH elastic dynamics”, computer method in applied mechanics and engineering, 190, pp. 6641-6662.

Hiraoka N., Oya A. , Bui Ha H., Rajeev P. and Fukagawa R. (2013). “Seismic slope failure modelling using the mesh-free SPH method”, Int. J. of GEOMATE, Sept., 2013, Vol. 5, No. 1 (Sl. No. 9), pp. 660-665 Geotec., Const. Mat. & Env., ISSN:2186-2982(P), 2186-2990(O), Japan.

Imase T., Maeda K., Miyake M., Sawada Y., Sumida H. and Tsurugasaki K. (2012) “Destabilization of a caisson-type breakwater by scouring and seepage failure of the seabed due to a tsunami”, Proceedings of ICSE6, Paris, August 27-31, 2012, pp.807-814.

Jaan Hui Pu , Songdong Shao (2012). “Smoothed Particle Hydrodynamics Simulation of Wave Overtopping Characteristics for Different Coastal Structures”, the Scientific World Journal volume 2012, article ID 163613, 10 pages doi:10.1100/2012/163613.

Joseph P. Morris, Patrick J. Fox, and Yi Zhu (1997). “Modeling Low Reynolds Number Incompressible Flows Using SPH”, JOURNAL OF COMPUTATIONAL PHYSICS 136, pp.214–226 (1997), article no. CP975776

Kazama Motoki, Noda Toshihiro (2012). “Damage statistics (Summary of the 2011 off the Paific Coast of Tohoku Earthquake damage)”. Soils and Foundations 2012; 52 (5): pp. 780-792.

LEMIALE Vincent, Mead Stuart and CLEARY Paul (2012). “Numerical Modelling of landslide events using a combination of continuum and discrete methods”, Proceedings of the 9th International Conference on CFD in the Minerals and Process Industries CSIRO, Melbourne, Australia 10-12 December, 2012, pp.1-6.

Lucy L.B. (1977). “Numerical approach to testing the fission hypothesis”, Astronomical Journal, 82: pp. 1013-1024.

Maeda Kenichi, Hirotaka Sakai and Mamoru Sakai (2004). “Development of seepage failure analysis method of ground with smoothed particle hydrodynamics”, JSCE vol.7, 2004, pp.775-786.

Martin J. C. and Moyce W. J. (1952). “An experimental study of the collapse of liquid columns on a rigid horizontal plane”, Phil. Trans. R. Soc. Lond., A 244, 312–324.

Monaghan J.J. and Lattanzio J.C. (1985). “ A refined particle method for astrophysical problems, Astronomy and Astrophysiscs, 149: 135-143.

Monaghan J.J. (1989). “On the problem of penetration in particle methods”, Journal of computational physics, 82: 1-15.

Monaghan J.J. (1994). “Simulating free surface flows with SPH”, Computational Physics, Vol.110, (1994), pp 399-406.

Monaghan J.J. (2000). “SPH without a tensile instability”, Journal of computational physics, 159, pp. 290-311.

Morris Joseph P., Fox Patrick J., and Zhu Yi (1997). “Modeling Low Reynolds Number Incompressible Flows Using SPH”, Journal of Computational Physics, 136: 214–226 .

Naili Mounir, Matsushima Takashi, Yamada Yasuo (2005). “A 2D Smoothed Hydrodynamics method for liquefaction induced lateral spreading analysis”, JSCE Journal of Applied Mechanics, Vol.8.

Nguyen C.T., Bui Ha H., and Fukagawa R. (2013). “Two-dimensional numerical modelling of modular-block soil retaining walls collapse using mesh free method”, Int. J. of GEOMATE, Sept., 2013, Vol. 5, No. 1 (Sl. No. 9), pp. 647-652 Geotec., Const. Mat. & Env., ISSN:2186-2982(P), 2186-2990(O), Japan.

Nonoyama Hideto (2011). “NUMERICAL APPLICATION OF SPH METHOD FOR DEFORMATION, FAILURE AND FLOW PROBLEMS OF GEOMATERIALS”, doctoral dissertation, Gifu University, Japan.

Nonoyama H., Yashima A., Moriguchi S. (2013). “Future evolution of slope stability analysis created by SPH method”, Proceedings of the 18th International Conference on Soil Mechanics and Geotechnical Engineering, Paris 2013, pp.2229-2232.

Randles P.W and Libersky L.D. (1996). “ Smoothed particle hydrodynamics some recent improvements and applications”, Computer methods in applied mechanics and engineering, 138: 375-408.

Songdong Shao , Changming Ji , David I. Graham , Dominic E. Reeve, Philip W. James, Andrew J. Chadwick (2006). “Simulation of wave overtopping by an incompressible SPH model”, Coastal Engineering 53 (2006), pp.723–735.

Swegle JW, Hicks DL, Attaway SW (1995). “Smoothed particle hydrodynamics stability analysis”, Journal of computational physics, 1995, 116(1), pp. 123-134.

Sakai H., Maeda K (2006). “Seepage failure of granular ground occurring for soil-water-gas interaction”. Geomechanics and Geotechnics of particulate media- Hyodo, Murata & Nakata (eds) , Taylor & Francis Group, London, ISBN 0-415-41097-5 , pp. 273-279.

Sakai H., Maeda K (2009). “Seepage Failure and Erosion Mechanism of Granular Material With Evolution of Air Bubbles Using SPH”. Proceedings of the 6 International Conference on Micromechanics of Granular Media edited by M. Nakagawa and S. Luding

American Institute of Physics 978-0-7354-0682-7, pp. 1001-1004.

Takahashi Sheigo, Arikawa Taro and Tomita Takahasi et al (2011). “Urgent survey for 2011 great east Japan earthquake and tsunami disaster in ports and coasts part I (tsunami)”, Technical note of PARI, no.1231, April 28, 2011.

Takahashi Hidenori, Sassa Shinji, Morikawa Yoshiyuki, Takano Daiki (2013). “Stability of breakwater foundation under seepage flow caused by tsunami”, report of Port and Airport Research Institute (PARI), Japan, vol. 52, No. 2, June 2013.

Takbiri Zeinab, Rasekh Amin and Afshar Mohammad Hadi (2010). “Analysis of Seepage through Dam Foundation using Smoothed Particle Hydrodynamics (SPH) Meshless Method”. World Environmental and Water Resources Congress 2010 Challenges of Change, 2010 ASCE, pp.1604-1612

WANG Jian, WU Hao, GU ChongShi and HUA Hui (2013).” Simulating frictional contact in smoothed particle hydrodynamics”, Science China Tech Sciences, 2013, 56: 1779-1789, doi:10.1007/s11431-013-5262-x

Yaidel Reyes Lopez, Dirk Roose and Carlos Recarey Morfa (2012). “Dynamic refinement for SPH simulations of post-failure flow of non-cohesive soil”, 7th international SPHERIC workshop Prato, Italy, May 29-31, 2012.